UNIVERSITY OF HONG KONG

DOCTORAL THESIS

Understanding Extreme Accretion and Outflows Around Black Holes through Radiative Transfer Studies

Author:
Lars Lund THOMSEN

Supervisor:
Prof. Jane Lixin DAI
Co-Supervisor:
Prof. Stephen NG

A thesis submitted in fulfillment of the requirements for the degree of Doctor of Philosophy

in the

Department of Physics
Faculty of Science

January 20, 2024

Abstract of thesis entitled

Understanding Extreme Accretion and Outflows Around Black Holes through Radiative Transfer Studies

Submitted by

Lars Lund THOMSEN

for the degree of Doctor of Philosophy

at The University of Hong Kong

in January, 2024

This dissertation investigates the observational characteristics of super-Eddington accretion and outflow through advanced radiative transfer simulations.

In the first part of the dissertation, I developed and utilised a general relativistic ray-tracing package to examine the X-ray reverberation signatures from super-Eddington accretion flows. My study reveals that the spectral and temporal signatures of Fe lines generated by super-Eddington flows have distinct morphologies compared to those produced by thin accretion disks: the line energy is more blueshifted, the line profiles are more symmetric, and the time lag of the line is much shorter. I apply my calculations to successfully model the Fe line observed from the jetted tidal disruption event Swift J1644+57, and I give direct quantitative evidence that a super-Eddington disk has likely formed in this event.

In the second part of the dissertation, I employ a state-of-the-art Monte Carlo Radiative Transfer code, Sedona, to calculate the continuum emission produced from simulated super-Eddington accretion flows, focusing on their relevance to tidal disruption events. I find that the spectral energy distribution depends not only on the inclination of the observer with respect to the disk but also on the accretion rate. Therefore, my results can be used to explain the diversity and evolution of TDEs, in which the accretion rate is expected to change rapidly over a timescale of years. In particular, I apply this model to explain tidal disruption events that start as optically bright but evolve to be X-ray bright later, such as ASASSN 15-oi.

This dissertation emphasises the importance of using radiative transfer calculations to study and understand super-Eddington accretion and outflow around black holes. The findings provide valuable insights into the physical processes involved in these events and contribute to developing more accurate models for future observations.

Abstract is 309 words

Declaration

I, Lars Lund THOMSEN, declare that this thesis titled, "Understanding Extreme Accretion and Outflows Around Black Holes through Radiative Transfer Studies", which is submitted in fulfillment of the requirements for the Degree of Doctor of Philosophy, represents my own work except where due acknowledgement have been made. I further declared that it has not been previously included in a thesis, dissertation, or report submitted to this University or to any other institution for a degree, diploma or other qualifications.

Signed: 

Date: January 20, 2024

Acknowledgements

I would like to express my heartfelt appreciation to my wife, Yvonne Chan, for her loving support and encouragement throughout my PhD journey. Her love, understanding, and patience have been instrumental in helping me overcome the challenges I faced along the way. I would also like to thank my parents for their constant support and belief in me and the academic path I wanted to pursue.

I am deeply grateful to my supervisor, Jane Lixin Dai, for her invaluable advice, mentorship, and expertise. Her support, constructive feedback, and insightful suggestions have been instrumental in shaping the outcome of this dissertation. In addition, I would like to thank her for enabling me to pursue exciting projects. Her support and encouragement have given me the confidence to pursue research questions that I found engaging and meaningful.

I am also grateful to the Hong Kong PhD Fellowship Scheme for supporting my doctoral studies financially. This prestigious fellowship has enabled me to focus on my research and pursue my academic interests without financial burden.

In addition, I would like to acknowledge the contributions of my collaborators, whose input and expertise have been priceless in shaping this research project. Lastly, I would like to thank all the individuals who have contributed to this work in one way or another. Your support, encouragement, and feedback have been invaluable in helping me accomplish this important milestone in my academic journey.

Lars Lund THOMSEN
University of Hong Kong
January 20, 2024

List of Publications

JOURNALS:

[1] **Thomsen L. L.**, Lixin Dai J., Ramirez-Ruiz E., Kara E., Reynolds C., "X-Ray Fluorescence from Super-Eddington Accreting Black Holes," *Astrophysical Journal Letter*, ApJL, 884, L21. doi:10.3847/2041-8213/ab4518, October 2019.

[2] **Thomsen L. L.**, Dai L., Kara E., Reynolds C. "Relativistic X-Ray Reverberation from Super-Eddington Accretion Flow ," *Astrophysical Journal*, 925, 151. doi:10.3847/1538-4357/ac3df3, February 2022.

[3] **Thomsen L. L.**, Kwan T. M., Dai L., Wu S. C., Roth N., Ramirez-Ruiz E., "Dynamical Unification of Tidal Disruption Events ," *Astrophysical Journal Letter*, 937, L28. doi:10.3847/2041-8213/ac911f, October 2022.

[4] Leloudas G., Bulla M., Cikota A., Dai L., **Thomsen L. L.**, Maund J. R., Charalampopoulos P., et al., "An asymmetric electron-scattering photosphere around optical tidal disruption events," *Nature Astronomy*, 6, 1193. doi:10.1038/s41550-022-01767-z, September 2022

DATASETS:

[1] Data set for Thomsen et al. (2019) can be downloaded here:
`https://github.com/gfh112/Xray-Flourescense`

[2] Data set for Thomsen et al. (2022a) can be downloaded here:
`https://github.com/gfh112/Xray_Reverberation`

[3] Data set for Thomsen et al. (2022b) can be downloaded here:
`https://github.com/gfh112/TDE_SED`

Contents

List of Figures

List of Tables

List of Abbreviations

ADAF	**A**dvection **D**ominated **A**ccretion **F**low
AGN	**A**ctive **G**alactive **N**ucleus
ASASSN	**A**ll **S**ky **A**utomated **S**urvey for **S**uper**N**ovae
BAL	**B**road **A**bsorption **L**ine
BEL	**B**road **E**mission **L**ine
BH	**B**lack **H**ole
BL	**B**oyer **L**indquist
BP	**B**landford- **P**ayne
BZ	**B**landford- **Z**najek
GR	**G**eneral **R**elativity (Relativitic)
GRRMHD	**G**eneral **R**elativistic **R**adiation **M**magneto**H**ydrodynamic
IMBH	**I**ntermediate **M**ass **B**lack **H**ole
ISCO	**I**nnermost **S**table **C**ircular **O**rbit
LTE	**L**ocal **T**hermal **E**quilibrium
MAD	**M**agnetically **A**rrested **D**isk
MBH	**M**assive **B**lack **H**ole
MCMC	**M**arkov **C**hain **M**onte **C**arlo
MCRT	**M**onte **C**arlo **R**adiative **T**ransfer
MESA	**M**odules for **E**xperiments in **S**tellar **A**strophysics
MRI	**M**agneto**R**otational **I**nstability
PLT	**P**alomar **T**ransient **F**actory
RIAF	**R**adiative **I**inefficient **A**ccretion **F**low
ROSAT	**R**ö**S**ntgen**SA**tellit
RT	**R**adiative **T**ransfer
SED	**S**pectrak **E**nergy **D**istribution
SMBH	**S**uper**M**assive **B**lack **H**ole
SE	**S**uper-**E**ddington
TDE	**T**idal **D**isruption **E**vent
UFO	**U**ltra-**F**ast **O**utflow
ULX	**U**ltra-**L**uminous **X**-ray binaries
UV	**U**ltra **V**iolet
XRB	**X** - **Ray** **B**inary
ZAMO	**Z**ero-**A**ngular **M**omentum-**O**bserver
ZTF	**Z**wicky - **T**ransient **F**acility

Chapter 1

Introduction

Black holes are astronomical objects that have fascinated both the public and scientists for decades. These objects can be formed when stellar cores collapse under their own gravity, creating an immensely dense region in space where the gravitational pull is so strong that nothing, not even light, can escape. According to the no-hair theorem, black holes are described solely based on their total mass and angular momentum (spin), meaning that the composition and distribution of matter within the black hole are unnecessary for its characterisation (Misner et al., 1973). Surprisingly, this makes black holes relatively simple mathematical entities despite their enigmatic reputation.

Direct electromagnetic observations of black holes are impossible as they do not emit detectable light. However, their influence on surrounding environments can be observed through the accretion process. As material falls toward a black hole, it heats up and generates intense radiation, which telescopes can detect. Accretion is crucial because the only other way to detect black holes indirectly is through their gravitational effects on gas and stars, which is only possible for nearby objects. The accretion process efficiently converts the mass-energy of infalling gas into radiation energy. By examining the radiation properties, astronomers can deduce the mass and spin of black holes. It has been discovered that supermassive black holes (SMBHs) exist at the centres of most galaxies, with masses typically exceeding 1 million solar masses. Despite their relatively small sizes, SMBHs can easily outshine the billions of stars that make up their host galaxies if they are accreting gas rapidly. These SMBHs are referred to as Active Galactic Nuclei (AGNs).

The mass of the SMBH is related to the velocity dispersion of the bulge stars ($M_{\mathrm{BH}} - \sigma_{\mathrm{Bulge}}$) (Magorrian et al., 1998), suggesting that SMBHs can significantly impact the growth and evolution of their host galaxies. However, the gravitational sphere of influence of a SMBH is typically a few orders of magnitude smaller than the size of the bulge of its host galaxy, so astronomers think it is likely due to a phenomenon called AGN feedback. AGN feedback is believed to be powered by the radiation and outflows produced during the accretion process. These radiation and outflows interact with and deposit energy into the star-forming gas in the host galaxy, thereby regulating the growth and evolution of the galaxy by suppressing star formation (Silk & Rees, 1998).

In general, the faster a black hole accretes gas, the more luminous it becomes. However, there is a theoretical upper limit on the luminosity produced from accretion, known as the Eddington limit. In some astrophysical systems, black holes have very high gas-feeding rates, and super-Eddington accretion occurs, which exceeds the Eddington limit. Recent disk simulations have demonstrated that such high accretion rates can produce a lot of radiation and, more importantly, strong outflows. For instance, some supermassive black holes are believed to have experienced super-Eddington accretion phases to account for the observed large masses at high redshift (Bañados et al., 2018). The rationale for the early super-Eddington phase is that if the SMBHs in the centre of galaxies have grown from smaller black hole mass seeds of $M < 10^4 M_\odot$, they could not have acquired enough mass through merging and Eddington limited accretion to explain the observations. The super-Eddington accretion phase deposits enormous amounts of energy through radiation and winds to the galactic gas (Kobayashi et al., 2018). Therefore, studying and understanding the early super-Eddington accretion phase and its outflows are crucial to understanding the mass evolution of SMBHs.

The recent surge in detecting tidal disruption events (TDEs) has paved the way for studying super-Eddington accretion in the local universe. These violent events occur when a star passes close to a quiescent SMBH and is torn apart by the tidal force into streams of stellar debris. Moreover, the peak fallback rate of the stellar debris is super-Eddington for $M_{\rm BH} < 10^7 M_\odot$, followed by a characteristic $t^{-5/3}$ decline pattern (Rees, 1988; Phinney, 1989). The devouring of the stellar debris occurs over months to years, enabling us to directly observe the formation and evolution of a super-Eddington accretion flow within a human lifespan. TDEs present an excellent opportunity to test the recent theoretical advances in super-Eddington accretion theory. Accurate modelling of these events can reveal information about the properties of the SMBH and the disrupted star as well as the physical environment around the SMBH. Therefore, TDEs are particularly useful for probing the mass population of quiescent black holes, which are otherwise difficult to study, except for very nearby SMBHs, through their gravitational effect on the dynamics. This highlights the importance of understanding and accurately modelling TDEs and, consequently, super-Eddington accretion flows.

This dissertation aims to model the observational signatures of super-Eddington accretion flows using radiative transfer studies. By comparing these modelling predictions to the observational properties of super-Eddington sources, such as TDEs, we can gain new insights into the geometry, energy, and physical processes happening in super-Eddington accretion. Moreover, the findings of this dissertation can contribute to our understanding of the growth and evolution of black holes and galaxies in the early phase of the universe.

1.1 Accretion Physics

Accretion onto black holes is a highly efficient process for extracting the mass-energy of matter. As matter falls onto a central object, its gravitational potential energy is released through radiation, heat, and kinetic energy. Therefore, accretion plays a crucial role in the formation and evolution of many astrophysical systems, including some of the most luminous objects in the universe, such as X-ray binaries (XRBs), AGNs, and TDEs, as well as the growth of massive black holes and galaxies. As a result, understanding the detailed mechanics of the accretion process is of utmost importance for advancing our understanding of the universe and its most energetic phenomena.

1.1.1 Accretion Process

The energy released from the accretion of matter of mass m from infinity to a central object of mass M and radius R_{obj} can be estimated using an order of magnitude calculation:

$$\Delta E_{\text{accretion}} = \Delta E_{\text{grav}} = \frac{GMm}{R_{\text{obj}}}, \tag{1.1}$$

where G is the gravitational constant. When assuming a steady inflow of mass ($\dot{m} = dm/dt$), the maximum gravitational energy that can be radiated away through the accretion process is represented by the luminosity:

$$L_{\text{acc}} = \Delta \dot{E}_{\text{accretion}} = \frac{GM\dot{m}}{R_{\text{obj}}}. \tag{1.2}$$

The efficiency of a system in radiating away gravitational energy is determined by the radiative efficiency η, which is defined as the ratio of radiation energy produced during accretion to the maximum possible energy available, represented by $\Delta \dot{E}_{\text{max}} = \dot{m}c^2$, where c is the speed of light. The maximum radiative efficiency available for accretion is:

$$\eta = \Delta \dot{E}_{\text{accretion}} / (\dot{m}c^2) = \frac{GM}{c^2 R_{\text{obj}}} \tag{1.3}$$

Therefore, black holes have some of the highest efficiencies as they are the most compact objects.

In general, the luminosity is expressed as:

$$L_{\text{acc}} = \eta \dot{m} c^2. \tag{1.4}$$

Accretion onto black holes typically results in a radiative efficiency of approximately $\eta = 0.1$, which means that around 10% of the mass-energy of the accreting gas is converted into radiation (Shakura & Sunyaev, 1973). This efficiency is significantly higher than the nuclear efficiency of fusion in the sun around $\eta_{\text{nuclear}} = 0.0007$. Therefore, black holes can radiate enormous amounts of energy with only a small amount of accreting material.

1.1.2 The Eddington Limit

The radiation released from accretion exerts pressure on the gas elements, which can slow down the gravitational infall of gas. The Eddington limit is derived from the hydrostatic equilibrium when the inward gravitational force counterbalances the outward radiation pressure force. To estimate this limit, I assume a steady, spherical accretion flow of ionised hydrogen. Thomson scattering on free electrons with a cross-section of σ_T dominates the outward radiation pressure, as the cross-section of protons is smaller by a factor of $(m_e/m_p)^2 \approx 5 \cdot 10^{-4}$ (see Chapter 1 in Frank et al., 2002). At the Eddington limit ($L_{\rm Edd}$), the proton-electron pair experiences equal inward gravitational force and outward radiation force. This can be written as:

$$F_{\rm rad} = \frac{L_{\rm Edd}\sigma_T}{4\pi c r^2} = F_{\rm gravity} = \frac{GM(m_p + m_e)}{r^2} \approx \frac{GMm_p}{r^2}. \tag{1.5}$$

Solving for $L_{\rm Edd}$ and normalising the result with a 10^6 solar mass black hole gives the following expression:

$$L_{\rm Edd} = 4\pi GMm_p c/\sigma_T \approx 1.3 \times 10^{44} \Big(\frac{M_{\rm BH}}{10^6 M_\odot}\Big) {\rm erg\ s^{-1}}. \tag{1.6}$$

The Eddington luminosity limit can also be expressed in terms of the Eddington accretion rate $\dot{M}_{\rm Edd}$, using the expression $L_{\rm Edd} = \eta \dot{M}_{\rm Edd} c^2$:

$$\dot{M}_{\rm Edd} = \frac{L_{\rm Edd}}{\eta c^2} = \frac{4\pi GMm_p c}{\sigma_T \eta c^2} = 0.023 M_\odot\ {\rm yr^{-1}} \Big(\frac{M_{\rm BH}}{10^6 M_\odot}\Big) \Big(\frac{\eta}{0.1}\Big)^{-1}. \tag{1.7}$$

The Eddington limit sets a critical upper limit on the amount of matter that can be accreted onto a black hole before the radiation pressure becomes too strong. This limit applies to a steady-state inflow of gas. However, recent studies have shown that this theoretical Eddington limit can be exceeded for several reasons. For instance, most systems do not accrete matter spherically. Instead, they form an accretion disk or torus structure due to the initial angular momentum of gas (Shakura & Sunyaev, 1973). In this configuration, radiation can freely escape in the low-density polar region, and the Eddington luminosity can be exceeded. Understanding the behaviour of matter in extreme environments, such as accretion onto black holes, is crucial to advancing our knowledge of the universe, so I present the accretion disk structures for both sub- and super-Eddington accretion in the following subsections.

1.1.3 Accretion Disks

When gas falls towards the central object with some amount of angular momentum, it cannot be accreted in a spherical structure (Bondi, 1952). Instead, it settles into a disk or torus structure due to the conservation of angular momentum. Then further angular momentum transport happens, and the gas accretes onto the central object through hydromagnetic processes in the disk (Shakura & Sunyaev, 1973; Balbus & Hawley, 1991).

The structure of an accretion disk depends on the accretion rate in relation to the Eddington limit. It can be broadly classified into three regimes: (I) the thin accretion disk, (II) the hot accretion flow, which describes radiatively inefficient accretion flow (RIAF) such as the advection-dominated accretion flow (ADAF), and (III) the super-Eddington accretion flow. I present a cartoon of the three disk structures in Fig. 1.1 and describe each of these disk geometries in more detail in the following subsections.

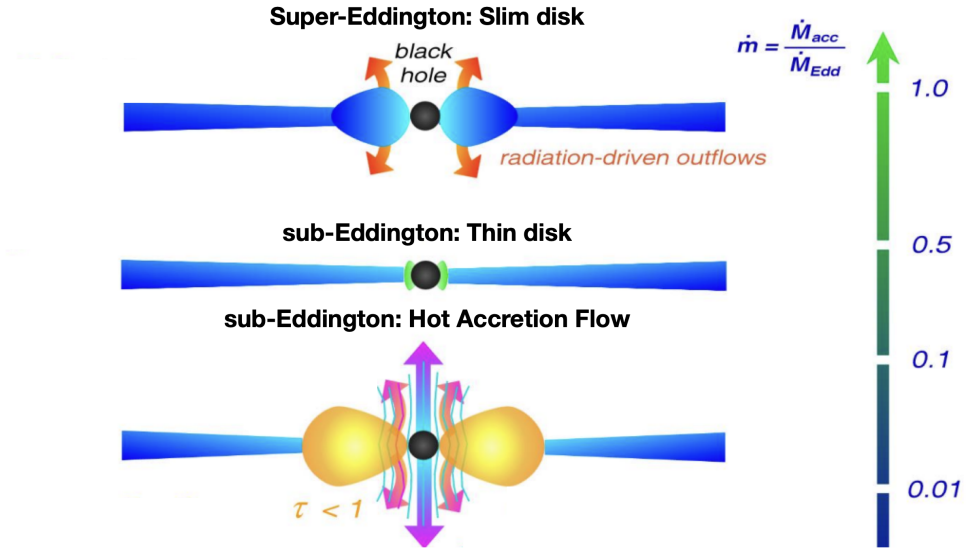

Figure 1.1: This figure illustrates three different disk structures based on the accretion rate. **The bottom panel** displays the hot accretion flow where the inner disk is hot, geometrically thick, and optically thin. This disk is radiatively inefficient, and the hot gas is advected before it can radiate away its energy. **The middle panel** shows the standard geometrically thin, optically thick disk, which is radiatively efficient. **The top panel** depicts super-Eddington accretion, where the inner disk is optically and geometrically thick. The disk is also radiative inefficient in the classical slim disk description. The figure is adapted from Müller (2004) with minor modifications.

Thin Disk Geometry

The thin disk is the most extensively studied disk structure, which was first proposed as an analytical model by Shakura & Sunyaev (1973); Novikov & Thorne (1973). This disk structure emerges when the accretion rate ($\dot{m}$) is slightly below the Eddington limit ($\dot{m} < \dot{M}_{\rm Edd}$) but not too low ($\dot{m} > 0.1 - 1\%\dot{M}_{\rm Edd}$). In this accretion regime, the disk is optically thick and radiatively efficient, allowing it to cool through blackbody radiation and remain geometrically thin with a small vertical extent, as illustrated in Fig. 1.1. Consequently, it can be treated as a one-dimensional structure, and many parameters are expressed as vertically integrated quantities, such as the surface density $\Sigma = \int_{-z}^{z} \rho dz$. The thin disk model has been successfully applied to explain various astrophysical systems, including young stellar objects, XRBs, AGNs. For a more comprehensive understanding of a thin disk's structure and derivation, please refer to Appendix A.1. Below, I highlight some of the key features of the thin disk.

The gas in the thin disk orbits the black hole at nearly perfect Keplerian velocity with a small radial inflow velocity. The innermost part of the disk, where the Keplerian velocity is the highest, has the highest temperature of the disk. The temperature profile of the disk is given by

$$T_s^4(r) = 3\frac{GM\dot{M}}{8\pi\sigma r^3}\left[1 - \left(\frac{R_{\rm ISCO}}{r}\right)^{1/2}\right], \tag{1.8}$$

where $R_{\rm ISCO}$ denotes the radius of the innermost stable circular orbit (ISCO), which depends on the black hole's dimensionless spin parameter and indicates the innermost extent of the accretion disk. Its values range from 1 to 9 gravitational radii ($R_g = GM/c^2$). Notably, the maximum temperature of the disk is found at $r = 1.36R_{\rm ISCO}$. By expressing the accretion rate in terms of Eddington luminosity and the radius in terms of gravitational radii, the maximum temperature of the disk is:

$$T_{\rm max} = 0.6 \times 10^6 K \left(\frac{\eta}{0.1}\right)^{-1/4} \left(\frac{M_{\rm BH}}{10^6 M_\odot}\right)^{-1/4} \left(\frac{L}{L_{\rm Edd}}\right)^{1/4} \left(\frac{R_{\rm isco}}{r_g}\right)^{-3/4}. \tag{1.9}$$

This equation reveals that, assuming the same Eddington luminosity, stellar-mass black holes have higher maximum temperatures than SMBHs. Since a thin disk is optically thick (Shakura & Sunyaev, 1973), the radiation it dissipates can be described as blackbody radiation. The total luminosity (L) emitted by the disk can be calculated by summing over the blackbody spectrum at each annulus, as shown in the following equation:

$$L = \int_{R_{\rm ISCO}}^{\infty} 2\pi r (2\sigma T(r)^4) dr = \frac{GM\dot{M}}{2R_{\rm ISCO}} = \frac{1}{2}E_{\rm pot}. \tag{1.10}$$

Here, σ is the Stefan-Boltzmann constant and the factor of 2 accounts for emission from both the top and bottom part of the disk. The thin disk can radiate up to half its potential energy away while the other half is lost in kinetic energy (the viral theorem). The spectrum of the accretion disk, obtained by integrating the blackbody radiation emitted by all annuli together, is typically the strongest in the X-ray band, with temperatures of the inner disk around $10^5 - 10^7$K.

It is important to note that the equations presented in this section were derived in the context of purely Newtonian gravity. However, Novikov & Thorne (1973) demonstrated that the results could be generalised to a general relativistic (GR) frame. Furthermore, all previous results are obtained by assuming the gas is in a steady state. In such a state, parameters like temperature are independent of the specific value of viscosity, which is good since this parameter is highly uncertain. While it is known that gas friction alone cannot account for it, turbulence and magnetorotational instability (MRI) have been suggested as possible sources of viscosity (Balbus & Hawley, 1991). The MRI arises due to the differential rotation of the disk, which leads to a shearing motion that can amplify the magnetic field and drive strong turbulence. As a result, the viscosity used in the thin disk model is often parameterised and takes on the form:

(Shakura & Sunyaev, 1973; Balbus & Hawley, 1991):

$$\nu = \alpha c_s H, \tag{1.11}$$

where c_s is the sound speed, H is the vertical extent of the disk and α is a unitless parameter describing how effectively angular momentum can be dissipated. It is generally believed that $\alpha \leq 1$ (Shakura & Sunyaev, 1973).

Despite its simplicity, the thin accretion disk model has proven to be a powerful tool for understanding the behaviour of accretion disks in various astrophysical contexts. As such, the thin accretion disk model is an essential theoretical framework for understanding the physics of accretion in the universe.

Hot Accretion Flow

When the accretion rate drops significantly below the Eddington limit ($\dot{m} < 0.1 - 1\% \dot{M_{\rm Edd}}$), the hot accretion flow structure is formed. In this regime, the standard thin disk prescription fails. The disk is unable to balance the viscous heating with cooling through radiation due to its lower density. As a result, nearly all of the viscously dissipated orbital energy is advected into the black hole before it can be radiated away (Abramowicz & Fragile, 2013). This causes the disk to become very hot and geometrically thick and to deviate from Keplerian orbits (Narayan & Yi, 1994, 1995; Yuan & Narayan, 2014). Due to their low radiative efficiency, ADAFs are much less luminous than the Shakura–Sunyaev thin disks and their spectra are non-thermal (Narayan et al., 1996; Yuan & Narayan, 2014). Their non-thermal spectra, which appear as a power law, make ADAFs a suitable candidate to explain X-ray binaries in the low, hard state. The Event Horizon Telescope observed two famous black holes, M87 and Sgr A*, in this accretion regime (Event Horizon Telescope Collaboration et al., 2019, 2022).

Super-Eddington Accretion

When the accretion rate exceeds the Eddington limit ($\dot{m} > \dot{M}_{\rm Edd}$), a super-Eddington accretion disk is formed. At such high accretion rates, radiation pressure significantly alters the disk structure, making it geometrically thick while remaining optically thick. These disks are considered radiatively inefficient due to the optically thick gas trapping photons, making it more likely for them to be advected into the black hole than diffusing out (Begelman, 1978).

To understand why the thin disk model fails at super-Eddington accretion rates, one can consider that the gravitational force must be greater than the radiative force at the thin disk surface ($z = H$) for gas to accrete. This requirement leads to the following

inequality:

$$F_{\rm grav}|_{z=H} = \frac{GM}{r^2+z^2}\cos\theta = \frac{GMz}{r^3(1-z^2/r^2)^{3/2}} \approx \frac{GM}{r^2}\frac{z}{r} >$$
$$F_{\rm rad} = \frac{\sigma_T}{c} f_{\rm rad} = \frac{\sigma_T}{c}\sigma_{\rm B} T^4_{\rm surface} = \frac{3GM\dot{M}\sigma_T}{8\pi r^3 c}\left(1-\left(\frac{R_{\rm ISCO}}{r}\right)^{1/2}\right)$$
$$= \frac{\dot{M}}{\dot{M}_{\rm Edd}}\frac{3m_p(GM)^2}{2\eta r^3 c^2}\left(1-\left(\frac{R_{\rm ISCO}}{r}\right)^{1/2}\right). \quad (1.12)$$

The surface temperature $T_{\rm surface}$ is taken from Eq. 1.8. This inequality shows that the scale height is proportional to the accretion rate, resulting in the following equation:

$$\frac{H}{r} > \frac{\dot{M}}{\dot{M}_{\rm Edd}}\frac{3GM}{2\eta r c^2}\left(1-\left(\frac{R_{\rm ISCO}}{r}\right)^{1/2}\right) = \frac{\dot{M}}{\dot{M}_{\rm Edd}}\frac{3}{2\eta}\frac{R_g}{r}\left(1-\left(\frac{R_g}{r}\right)^{1/2}\right), \quad (1.13)$$

where the inner radius of the accretion disk is set to the gravitational radii, $R_{\rm ISCO} = R_g = GM/c^2$. This function has a maximum value at:

$$\frac{H}{r}|_{\rm max} > \frac{\dot{M}}{\dot{M}_{\rm Edd}}\frac{3}{2\eta}\frac{4}{27} = 2.2\frac{\dot{M}}{\dot{M}_{\rm Edd}} \quad \text{for} \quad \eta = 0.1. \quad (1.14)$$

As a result, the disk becomes geometrically thick ($\frac{H}{r} > 1$) at super-Eddington accretion rates, contradicting the assumption of $H/r << 1$ used to derive the thin disk structure.

One of the early theories of super-Eddington accretion was explored by Abramowicz et al. (1988), who derived a semi-analytical disk model called the slim disk. This model has since been refined by other researchers, such as Beloborodov (1998); Sądowski (2009); Abramowicz & Fragile (2013). At lower accretion rates, the slim disk model simplifies to the thin disk, but it allows the gas to extend within the ISCO, making it more general and realistic. However, at high accretion rates, the rotational velocity deviates significantly from the Keplerian speed, and the radial inflow velocity becomes significant compared to the rotational velocity, causing the inner region to thicken. Consequently, advection turns on, leading to decreased radiative efficiency. This occurs because hot gas can be advected to the black hole before it can cool through radiation, while the thin disk assumes all the viscous heat can be efficiently radiated away. Thus, at high Eddington accretion rates, the luminosity only slightly exceeds the Eddington limit in this slim disk model.

The slim disk solution remains self-similar for disk thickness up to $H/r \leq 1$ in the inner regions, corresponding to moderately super-Eddington accretion rates ($\dot{m} <$ few $\times \dot{M}_{\rm Edd}$). However, these semi-analytical models do not account for the production of large-scale winds or super-Eddington luminosities, which have been observed in a few super-Eddington systems (Pinto et al., 2016; Kara et al., 2016b, 2018; Alexander et al., 2017). Recent numerical studies have more accurately revealed the physics of super-Eddington flows, which I describe in more detail in Chapter 1.1.5.

1.1.4 Outflows

Outflows are a commonly observed feature in accretion systems, ranging from super-Eddington sources, such as ultra-luminous X-ray binaries (ULXs) (e.g., Pinto et al., 2016; Kosec et al., 2018) and TDEs (e.g., Alexander et al., 2016; Kara et al., 2018; Hung et al., 2021) to sub-Eddington sources such as AGNs (Weymann et al., 1981, 1991; Knigge et al., 2008), and even in hot accretion flows such as Sgr A* and M87 (Yuan & Narayan, 2014; Bu et al., 2016). These outflows can carry a significant amount of mass and energy, and they are believed to play a crucial role in regulating the accretion process and shaping the surrounding environment (Yuan et al., 2015; Yang et al., 2022).

To produce an outflow, the gas must have a velocity greater than the gravitational escape velocity or a driving mechanism that prevents it from falling back onto the black hole once launched. However, determining what constitutes a genuine wind rather than a turbulent outflow in accretion flow simulations is numerically challenging and requires detailed calculations, as demonstrated by Yuan et al. (2015). Additionally, the literature has no clear distinction between winds and jets. Hereafter, we define jets as highly collimated and relativistic outflows launched close to the black hole, while winds are less collimated and have slower outflow velocities.

In this overview, I discuss the three main mechanisms that can drive an outflow in an accretion disk: I) thermal, II) magnetic, and III) radiative.

Thermally Launched Outflows

Thermally launched outflows occur when the gas temperature in the accretion disk is so high that the thermal velocity ($v_T = \sqrt{\frac{kT}{m}}$) becomes comparable to the escape velocity ($v_{es} = \sqrt{\frac{2GM}{r}}$), which requires temperatures above $T > 10^7 K$ for the inner disk region. This temperature far exceeds the thin disk predictions in Eq. 1.8. However, Begelman et al. (1983) have argued that X-rays from the inner disk may be able to heat the gas through Compton heating, leading to the required temperatures for thermally launched winds in the outer region of the accretion disks. This is also called a Compton or corona wind. XRBs have been suggested as a potential source for launching this type of wind due to Compton heating (Done et al., 2018), but this mechanism is unlikely to be responsible for AGN or TDE winds.

Magnetically Launched Outflows

Magnetic fields are a crucial component of accretion disks, playing a significant role in launching winds, jets and driving accretion. The magnetic fields in accretion disks can either be generated by the gas dynamo action (as described in the review by Brandenburg & Subramanian, 2005) or carried to the vicinity of the black hole by the accreting gas.

Magnetic fields can drive winds through the magneto-centrifugal mechanism, also called the Blandford-Payne (BP) mechanism (Blandford & Payne, 1982), which involves

the interaction between magnetic fields in the disk and ionised gas. The ionised gas is coupled to the magnetic fields, which are twisted due to the disk's differential rotation. This coupling causes the gas to follow the magnetic lines, resulting in a torque that can launch the gas as a wind. As the gas moves further from the accretion disk, the magnetic field lines weaken, allowing the gas to disperse to larger solid angles.

A process similar to the BP mechanism but happening under more extreme conditions is the Blandford-Znajek (BZ) process, which was first explained by Blandford & Znajek (1977). As the magnetic field lines enter the ergosphere of the black hole, the frame-dragging effect twists the magnetic field lines, forming helical structures. A Poynting flux is then produced and confined by the magnetic field lines. This process can allow the extraction of the rotational energy of a black hole, which leads to the creation of powerful, relativistic jets. The BZ process is currently considered the most promising explanation for the launch of high-energy and relativistic jets. The power of these jets is directly proportional to the square of the black hole's spin and magnetic field strength and can be expressed as $P \propto a^2 B^2$.

Radiatively Launched Outflows

Radiation-driven winds, powered by electron scattering, are expected to occur naturally in systems where the accretion rate is close to or above the Eddington limit, as shown in Kobayashi et al. (2018). This makes it an obvious mechanism for driving winds in super-Eddington disks, such as TDEs (Miller et al., 2015). This effect arises because, at super-Eddington luminosities, the radiation pressure generated by the accretion process becomes so strong that it dominates over gravity, making it impossible for a spherical accretion process to be sustained, as derived in Section 1.1.2. As a result, the intense radiation pressure can drive gas outward and give rise to strong winds.

Resonant line scattering can further increase the radiation pressure by causing photons of a specific wavelength to be absorbed and re-emitted through bound-bound transitions, resulting in a net transfer of momentum and energy from the radiation field to the gas. This can create a force multiplier that magnifies radiation pressure by up to 2000 times in O stars, enabling stars to generate strong winds (Castor et al., 1975). Radiation plus line-driven winds may also be important for launching winds in sub-Eddington accretion sources, such as AGNs (Murray et al., 1995; Proga et al., 2000). In these systems, the radiation pressure alone may not be sufficient to drive a wind through electron scattering alone. However, when resonance line scattering is considered, the total radiation pressure may be strong enough to accelerate the gas and launch a wind.

In conclusion, accretion disks, such as those formed in XRBs, AGNs, and TDEs, can give rise to outflows driven by various mechanisms, including thermal pressure, radiation pressure, and magnetic fields. However, a combination of all these mechanisms can operate simultaneously in each system. These winds can significantly impact

the surrounding environment of the black holes, shaping the growth and evolution of galaxies and other structures in the universe.

1.1.5 Numerical Simulation of Super-Eddington Accretion

Recent advances in numerical studies of super-Eddington accretion disks have revealed that the Eddington luminosity limit can indeed be surpassed due to the advection of photons by magnetic bubbles (buoyancy) or the launching of large-scale optically-thick winds or relativistic jets (Ohsuga et al., 2009; Jiang et al., 2014; McKinney et al., 2015; Dai et al., 2018). The optically thick outflows typically reach ultra-fast speeds of $v \geq 0.1c$, enabling them to carry a significant amount of energy. These energy transport mechanisms allow super-Eddington accretion systems to boost the radiative efficiency much larger than the slim disk model predicts while keeping super-Eddington accretion rates, despite emitting energy well above the Eddington limit.

Simulations of super-Eddington accretion flow reveal structures that agree with observations, such as fast wind structures. Fig. 1.2 illustrates the accretion flow geometry of two different simulations and (GR) radiation magnetohydrodynamic codes; these structures typically include a thick disk from which large-scale, optically thick winds are launched. A relativistic jet can also be launched via the BZ process if the black hole is spinning. Moving from the disk to the pole, the density generally decreases while the velocity increases, creating an optically thin funnel in the polar region through which X-rays can escape. However, the precise geometry of the wind and funnel can vary depending on the initial conditions of the simulation, such as the accretion rate (Jiang et al., 2019), magnetic field strength and topology (Sądowski & Narayan, 2016), and black hole spin (Sądowski et al., 2014).

Although the study of super-Eddington accretion disks is still in its early stages, these simulations highlight the need for additional numerical simulations to fully understand these systems' complexities. Since these simulations are computationally expensive, it is crucial to assess whether the predicted structures can explain some of the more detailed observational features and to determine if more advanced (and computationally expensive) models are necessary to explain any discrepancies.

1.2 X-Ray Reverberation

X-ray reverberation is a technique that has revolutionised our understanding of accretion disks around black holes and other compact objects. It was first proposed by Fabian et al. (1989) as a way to study geometry and physical properties of the inner regions of these disks, which is difficult or impossible to measure directly through other means. In X-ray reverberation, the X-ray emission from the corona illuminates the surrounding material, causing it to emit characteristic reflection features, such as the Fe Kα line. By characterising the line profile and measuring the time delay between the

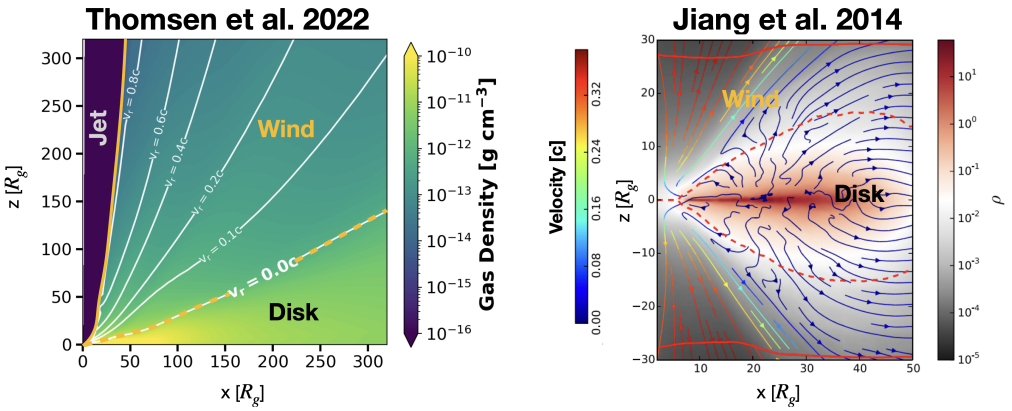

Figure 1.2: The two figures depict the geometry of two super-Eddington simulations obtained with different codes and initial conditions. Both figures display the two primary regions that are commonly observed in simulations of super-Eddington accretion flows: the disk and high-velocity winds. The background colour corresponds to the density of each region, and the white lines represent contours of constant radial velocity or streamlines for the figures on the left and right, respectively. In this context, the disk refers to the radial inflow region, while the wind represents the radial outflow of gas. The jet, highlighted in dark blue in the left panel, is where the magnetic pressure exceeds the gas pressure, and it is launched in these simulations due to the BZ process, which requires a rotating black hole. No jet is launched in the rightmost panel due to a non-spinning black hole. The velocity increases from the disk to the polar region while the density decreases. The figure on the left is adapted from Thomsen et al. (2022b), while the figure on the right is adapted from Jiang et al. (2014).

direct X-ray emission and the reflected emission, it is possible to infer the distance between the X-ray source and the surrounding material, as well as the viewing angle, the mass and the spin of the black hole. Therefore, X-ray reverberation has proved to be a powerful technique for studying the behaviour of accretion disks in a wide range of astrophysical contexts, from AGNs (Fabian et al., 1989; Tanaka et al., 1995; Zoghbi et al., 2012) to X-ray binaries (Mushotzky et al., 1978; Miyamoto et al., 1988) and TDEs (Kara et al., 2016b) since it provides a direct measurement of the inner disk geometry.

1.2.1 Canonical Thin Disk Geometry

X-ray spectra in AGNs and XRBs typically consist of three distinct components. The first component is a thermal disk spectrum, originating from the thin accretion disk surrounding the black hole or neutron star. The second component is a non-thermal hard spectrum, which arises from high-energy electrons in the corona close to the disk. These electrons can cause the thermal photons from the disk to Compton up-scatter, resulting in the hard power law spectrum. The third component is a reflection spectrum, which arises from the interaction of the hard X-ray emission with the disk. This interaction produces a reflected spectrum that contains various features, such as emission lines and a broad hump-like feature known as the Compton hump. The corresponding geometry behind these three components and their relative strength in an AGN is

depicted in Fig. 1.3. Accurately determining the relative contributions of these three components is crucial for interpreting X-ray spectra and extracting valuable information regarding the astrophysical processes occurring in these systems.

Thin Disk Component

The thermal photon energy distribution emitted by the disk is determined by the disk's temperature and geometry, as discussed in Section 1.1.3. For thin accretion disks around SMBHs, the temperatures generally peak in the extreme ultraviolet (EUV) range. Consequently, X-ray emissions stem from the Wien tail of the disk's hottest region. In contrast, X-ray binaries with stellar-mass black holes exhibit peak temperatures in the X-ray range (see Eq. 1.8). Overall, the temperature and associated X-ray flux increase towards smaller radii. However, the thin accretion disk cannot extend to the event horizon. This limitation arises because, within the ISCO, gas falls to the event horizon within a free fall time (Reynolds et al., 1999). The canonical view assumes that gas densities within this radius are negligible, but recent studies have begun to challenge this assumption (Wilkins et al., 2020). Despite advances in black hole accretion modelling, the standard models utilised in the X-spec package, such as `REFLOINX` (Ross & Fabian, 2005) and `RELXILL` (Dauser et al., 2013; García et al., 2013, 2014), assume that the accretion disk terminates at ISCO. This assumption is significant because the ISCO's location varies depending on the black hole's spin, with the ISCO being closer to the black hole for higher spins, ranging from $1.235R_g$ for a maximally spinning black hole ($a = 0.998$) (Novikov & Thorne, 1973; Thorne, 1974) to $6R_g$ for a non-spinning black hole ($a = 0$). As a result, this technique can be used to constrain the black hole spin in AGNs and XRBs in the thin disk regime.

Corona Component

The X-ray spectra of several accreting black hole systems, such as AGNs, are dominated by a continuous emission, taking the form of a power law that extends up to energies of 100 keV (Reynolds, 2014). It is widely believed that these hard X-rays are produced through inverse Comptonisation between disk thermal photons and a very hot "corona" consisting of energetic electrons ($kT \approx 100$ keV) (Pozdnyakov et al., 1977). Despite various theoretical efforts, the production mechanism of the hot corona is still unknown. Some possible candidate models include reconnection of magnetic field lines and particle acceleration in the base of the jet (Galeev et al., 1979; Blandford et al., 2017; Yuan et al., 2019).

Because the corona production mechanism is still unclear, various models have been proposed for the corona's geometry. The simplest and most extensively studied model is the "lamppost" model (George & Fabian, 1991), where the corona is assumed to be an isotropically radiating point source located a few R_g above the black hole (Matt et al., 1991; Reynolds & Begelman, 1997) (see Fig. 1.3). Other corona geometries that have been investigated include an off-axis compact corona or extended corona sources

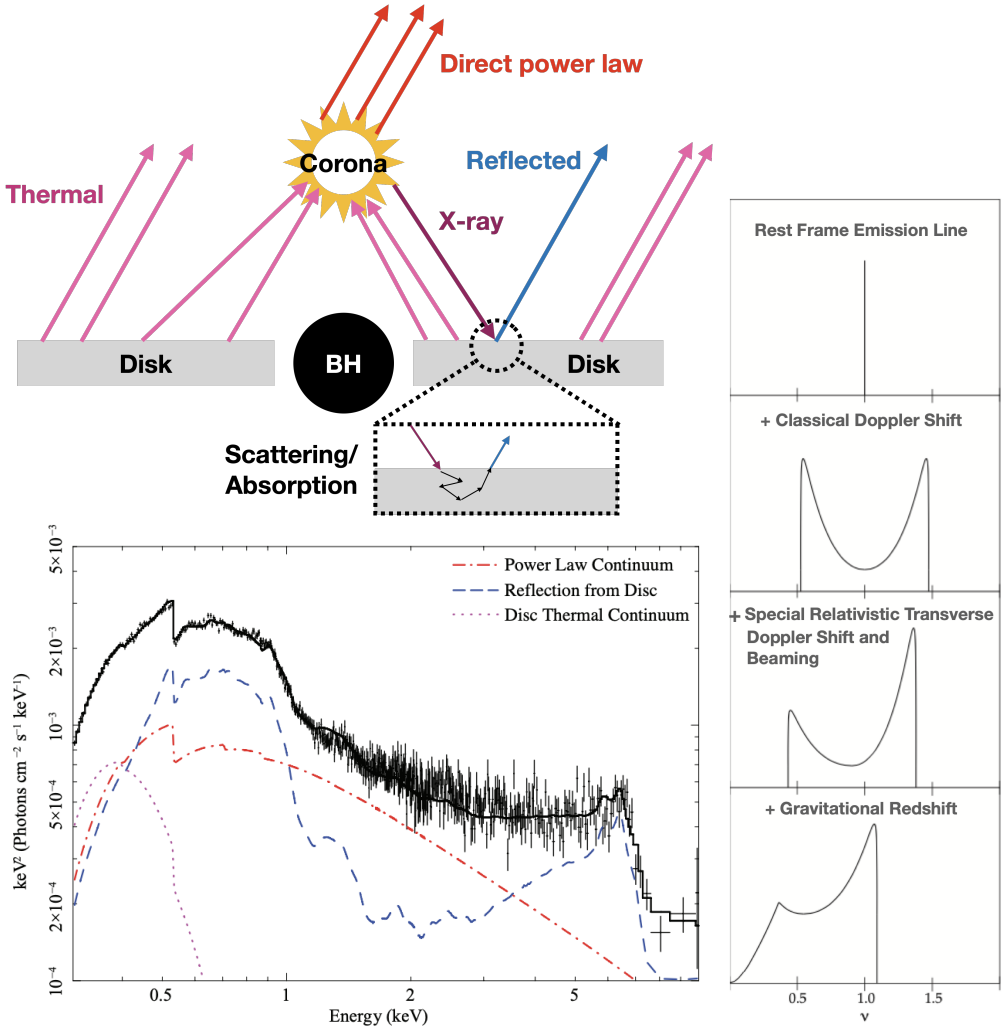

Figure 1.3: The figure on the top left illustrates the "lamppost model" geometry and the origin of the three X-ray spectral components: thermal disk, corona, and reflection. The disk emits thermal photons, which can be Compton up-scattered by the corona to form a non-thermal hard power law. This non-thermal emission irradiates the disk, producing reflection spectra via scattering and absorption. **The figure on the bottom left** shows the contribution of each component in fitting the Seyfert 1 galaxy, 1H 0707-495. Notably, the Fe Kα line, soft excess, and Compton hump all originate from the reflection spectrum. Figure from Wilkins (2013). **The right-hand side of the figure** depicts how relativistic effects distort emission lines produced at a particular radius. In the rest frame, these lines would be observed as delta functions. However, as the gas orbits around the black hole, the lines acquire a Doppler shift, causing the profile to broaden. Furthermore, the gas orbits at relativistic speeds, which results in the beaming effect of the blue light that moves towards the observer, leading to a skewed appearance. Furthermore, due to the strong gravitational field in the vicinity of the black hole, photons lose energy while moving away from it, which causes an overall redshift of the line. Figure slightly modified from Wilkins (2013)

(see Wilkins & Fabian, 2012). However, current observational evidence, such as short X-ray reverberation time delays and gravitational micro-lensing, supports a relatively

compact corona structure located near the black hole (Reis & Miller, 2013; Kara et al., 2016a).

Reflection Component

A reflection spectrum is produced via scattering and absorption processes as the disk reflects the corona's hard X-ray photons. The reflection spectrum features several components, including the Fe Kα line typically at around 6.4 keV, a soft excess below 1 keV, and a Compton hump around 30 keV (Matt et al., 1991; Ross & Fabian, 2005; García et al., 2014). While the work in this dissertation focuses mainly on the Fe Kα line, which is discussed in the next section, the other two components are briefly discussed below.

When X-ray photons interact with the accretion disk's material, they undergo various processes, including Compton scattering by electrons in the disk. The energy exchange during this process depends on the photon's energy relative to the disk's Compton temperature. Generally, if the photon's energy is higher than the Compton temperature, it loses energy, while if its energy is lower, it gains energy on average. The Compton scattering process produces a distinctive "Compton hump" in the reflection spectrum, which is an excess of photons typically observed around 20-30 keV.

The soft excess observed at energies below 1 keV cannot be accounted for by the standard accretion disks around SMBHs (Shakura & Sunyaev, 1973). One proposed explanation for the soft excess is a warm corona with a temperature of $kT = 1$ keV. However, this model cannot explain why the soft excess is independent of the black hole's mass (Gierliński & Done, 2004). To address this issue, some researchers have suggested that the absorption and re-emission of X-ray photons, along with relativistic blurring of different lines in the X-ray spectrum, such as OVII, OVIII, and Fe lines, can produce the soft excess (Ross & Fabian, 2005). This hypothesis has been modelled using `REFLIONX` and shown in Fig. 1.3. Therefore, the soft excess has also been attributed to the reflection spectrum.

1.2.2 Fe K Line

The Fe Kα fluorescence line is the most prominent feature in the reflected spectrum, and it is generated when X-ray photons with energies above the ionisation threshold, which is 7.1 keV for neutral Fe, interact with an Fe atom. This interaction causes an electron to be ejected from the inner K-shell (with principal quantum number n = 1) through photoionisation, creating a vacancy in the K-shell. The vacancy is then filled by an electron from a higher energy level, such as the L-shell (n = 2), releasing energy in the form of a characteristic X-ray photon with an energy between 6.4-6.97 keV, corresponding to the Fe Kα fluorescence line.

Production of Fe K Line

The energy of the Fe Kα line emitted depends on the ionisation state of the Fe atom. For low-ionisation states, the rest-frame energy is 6.4 keV, while for high-ionisation states primarily composed of FeXXV and FeXXVI, the rest-frame energies are 6.7 keV and 6.97 keV, respectively (Reynolds & Begelman, 1997; Ballantyne & Ramirez-Ruiz, 2001).

However, for elements other than Fe, the K-shell absorption and subsequent emission process have a low probability due to their low radiative yield, which goes approximately as the quartic of the atomic number for neutral atoms Z^4 (Bambynek et al., 1972; Krause, 1979). Consequently, these lighter atoms are more likely to de-excite through the Auger process, which involves electron emission without the Kα lines. As Fe is the most abundant heavy element, there is no overlap with other lines, and the line is predominantly isolated since other abundant atoms, such as oxygen, do not possess such high ionisation potentials.

In the next section, I present how the Fe Kα line is broadened and how we can extract information about the black hole's inclination and spin from the line profile.

Line Broadening

Fe Kα lines are generated in the vicinity of black holes and appear broadened and skewed when observed due to the combined effects of general relativistic redshift and Doppler shifts, as seen in Fig. 1.3. The primary influence of general relativity is the shift of the line profile towards the red end of the spectrum caused by gravitational redshift (Shapiro, 1964). Additionally, the Doppler effect arises from the disk's Keplerian rotation, resulting in blueshifted lines when gas moves towards the observer and redshifted lines when gas moves away from the observer.

For instance, a system with a large prograde spin and viewed nearly face-on yields a highly redshifted Fe line profile due to gravitational redshift in the innermost regions and minimal Doppler shifts. In contrast, a black hole with minimal or retrograde spin has an inner radius further away, leading to smaller overall redshifts. Astronomers use this method to determine a black hole's spin. When observed nearly edge-on, the lines are subject to both gravitational redshift and Doppler shifts. The relativistic speeds in the innermost region result in the relativistic Doppler effect, where the blueshifted component is enhanced, as illustrated in Fig. 1.3.

In summary, the Fe K α line profile is independent of the black hole mass (Fabian et al., 1989) and is primarily shaped by the viewing angle and spin. However, as briefly discussed in the following sections, it also depends on the corona geometry, which can best be constrained by analysing temporal and spectral data together.

1.2.3 X-Ray Echoes

The corona exhibits considerable variability in its emission (Ponti et al., 2012), causing the reflection spectrum to exhibit similar variability but with a slight delay due to the

light travel time between the corona and the accretion disk. Consequently, variations in reflection-dominated parts of the spectrum, such as the soft excess (0.1-1 keV) band and the Fe K (4-7 keV) band, are anticipated to lag behind those of the continuum-dominated part of the spectrum. Astronomers can then map out the inner disk geometry by examining these light echoes as a function of energy under a general relativistic treatment.

Fe K-lags in AGNs were first detected by Zoghbi et al. (2012), and since then, over 20 AGNs with Fe K-lags have been observed, exhibiting lags of a few hundred to a few thousand seconds behind the continuum (see Kara et al., 2016a, and references therein). This lag timescale corresponds to the travel time of photons reflected from the inner disk within a few gravitational radii ($t = \text{few} \times R_g/c = \text{few} \times 49(M_{\rm BH}/10^7 M_\odot)$ seconds). Therefore, the observed time delay, which is primarily caused by the light travelling time, can be employed to estimate the physical distance to the corona. However, a degeneracy exists between the height of the corona in gravitational units and the mass of the black hole, as black holes exhibit scale invariance when neglecting cooling/heating terms (Cackett et al., 2014; Uttley et al., 2014).

1.2.4 X-Ray Reverberation from Super-Eddington Accretion Flows

Prior to this work, there had been limited exploration of how the reflection scenario differs from sub-Eddington (thin disk regime) sources to super-Eddington sources, which likely results from the absence of X-ray reverberation observation signatures from super-Eddington accretion flows. Such a signature was initially reported by Kara et al. (2016b) in the case of the jetted TDE Swift J164449.3+573451 (Swift J1644 hereafter), where a highly blueshifted line around 7.5-8.5 keV was observed, suggesting reflection by fast outflows. Further details on this event can be found in Section 1.3.2, and general information on TDEs is presented in Section 1.3. Recently, a few more detections of X-ray reverberation in likely super-Eddington sources have been detected, such as the sudden appearance evolution and disappearance of the broad line region of AGN 1ES 1927+654 (Masterson et al., 2022) making it Changing Look AGNs, and the narrow-line Seyfert 1 galaxy 1H 0323+342 (Mundo et al., 2020).

Actually, the canonical razor-thin disk model is even non-physical in the thin disk regime, as radiation pressure inherently generates a non-zero vertical disk height (Shakura & Sunyaev, 1973). The effect of non-zero disk thickness has been explored by Taylor & Reynolds (2018a,b). One should expect the reverberation geometry in super-Eddington flows to be even more drastically different from the canonical picture. As I later show in Chapters 3 and 4, the coronal emission is reflected or reprocessed by the optically thick winds rather than the surface of an exposed disk in the super-Eddington case. Furthermore, the Doppler shift of the Fe Kα line mainly originates from the motion of the optically thick winds instead of the equatorial Keplerian motion of the thin disk flow. Such discoveries allow us to use the X-ray reverberation features to probe the winds produced from super-Eddington accretion flows.

1.3 Tidal Disruption Events

A tidal disruption event (TDE) occurs when a star comes too close to a SMBH, causing the tidal force of the SMBH to overpower the star's self-gravity. This results in the star being stretched as it approaches the SMBH and ultimately fully disrupted into stellar debris near its pericentre. Roughly half of the debris is gravitationally bound to the SMBH and can eventually accrete onto the SMBH, while the other half is ejected at high velocities and never returns. Such an event generates a bright flare that can last months to years, emitting radiation often across the electromagnetic spectrum, from X-rays to radio waves (Rees, 1988; Phinney, 1989). However, TDEs are rare events, happening only once every 10,000 to 100,000 years per galaxy (Magorrian & Tremaine, 1999; Wang & Merritt, 2004; Stone & Metzger, 2016).

Due to their rare and short-lived nature, TDEs are ideal targets for all-sky transient surveys, most of which are currently conducted using optical telescopes, such as the All Sky Automated Survey for SuperNovae (ASASSN), the Palomar Transient Factory (PTF) / Zwicky Transient Facility (ZTF) (Holoien et al., 2014; Hung et al., 2017; van Velzen et al., 2021; Hammerstein et al., 2023). These surveys have different sensitivities and capabilities, which make them complementary in the search for TDEs across the electromagnetic spectrum. Also, X-ray telescopes such as ROSAT and the Swift Gamma-Ray Burst Explorer have detected several TDEs which are strong in X-rays and gamma-rays (e.g. Bade et al., 1996; Komossa & Bade, 1999; Bloom et al., 2011).

One especially intriguing aspect of TDEs is that they make otherwise quiescent SMBHs detectable, allowing researchers to study the properties and demographics of these massive objects (Rees, 1988). Additionally, TDEs can help detect intermediate-mass black holes (IMBHs) that may reside in dwarf galaxies and stellar clusters. Furthermore, TDEs can provide insight into the population and dynamics of stars in the innermost regions of galaxies. Finally, TDEs are a promising avenue for studying the physics of accretion disks and jets around black holes.

In this section, I present some of the basic theories and observational facts of TDEs. Then, I describe how the modelling of TDEs has evolved over the past decade. It is worth mentioning that even the most sophisticated models developed so far require complex calculations conducted on supercomputers. However, as I show, more detailed modelling is still needed to comprehend all the physical processes happening in TDEs.

1.3.1 The Canonical Models of TDE

TDEs were first theoretically proposed as a way to validate the existence of black holes by Hills (1975); Frank & Rees (1976); Rees (1988) before their first detection by Bade et al. (1996) and Komossa & Bade (1999). The canonical understanding of TDEs is still based on the analytical description of the disruption and emission process presented

in Rees (1988) and Phinney (1989). Here, I present this description as the "first-order" picture of the TDE phenomenon.

The Tidal Radius

A TDE occurs when other stars in the bulge of the galaxy scatter a star within the "tidal radius" of a SMBH. This tidal radius (R_T) is the distance at which the gravitational force of the black hole becomes dominant and overwhelms the self-gravity of the star. By utilising the definition of the tidal radius and performing a Taylor expansion with respect to the small parameter R_*/R_T, we can equate the gravitational force at the surface of the star to the tidal forces from the black hole to obtain the tidal radius as shown below:

$$F_{\text{self}} = GM_*/R_*^2 = F_{\text{tidal}} = \frac{GM_H}{R_T^2} - \frac{GM_H}{R_T^2(1+R_*/R_T)^2} \approx \frac{GM_H}{R_T^2} - \frac{GM_H}{R_T^2}(1-2R_*/R_T)$$
$$R_T = \left(2\frac{M_H}{M_*}\right)^{1/3} R_* \approx \left(\frac{M_H}{M_*}\right)^{1/3} R_*. \tag{1.15}$$

Here, the variables R_*, M_*, and M_H represent the radius of the star, the mass of the star, and the mass of the black hole, respectively. The expression of the tidal radius implies that a maximum black hole mass exists for a given combination of stellar mass and radius that can cause a star to be disrupted outside the event horizon of the black hole. Otherwise, a black hole with an even higher mass could only disrupt the star within its event horizon, which renders the event invisible. Scaling with a one-solar-mass star, this maximum black hole mass threshold is:

$$M_{\text{BH}} = 1.1 \times 10^8 M_\odot \left(\frac{m_*}{M_\odot}\right)^{-0.5} \left(\frac{R_*}{R_\odot}\right)^{3/2}. \tag{1.16}$$

Therefore, TDEs can probe SMBHs with masses lower than those explored through AGN studies, which are usually above $10^7 M_\odot$ based on reverberation or the $M-\sigma$ relation (Magorrian et al., 1998; Vestergaard & Peterson, 2006; McConnell et al., 2011). This distinction emphasises the unique nature of TDEs and their potential for studying SMBHs at the lower end of the mass spectrum.

The Disruption Process

To analytically describe the disruption process, Rees (1988) considered a simple scenario where a star remains gravitationally bound until it reaches the tidal radius, within which the stellar gas instantly becomes unbound. As a result, the binding energy of the disrupted star is conserved until it reaches the tidal radius. The star's centre is expected to be on an initially parabolic orbit with zero orbital energy. At the tidal radius, the potential energy gradient between the star's centre and its radius is redistributed into orbital energy, resulting in a spread in energy given by:

$$-\Delta\epsilon_{\text{orbit}} = \Delta\epsilon_{\text{potential}} = \frac{GM_{\text{BH}}}{R_T} - \frac{GM_{\text{BH}}}{R_T(1+R_*/R_T)} \approx \frac{GM_{\text{BH}}R_*}{R_T^2}. \tag{1.17}$$

However, a more general calculation of the disruption process involves considering the pericentre distance of the star's initial parabolic orbit, which might differ from the tidal radius. This is quantified by the impact parameter $\beta = R_T/R_P$, where R_T is the tidal radius, and R_P is the pericentre distance of the original stellar orbit. Full disruption events are usually assumed to occur when $\beta > 1$, while partial disruption events where the stellar core survives occur when $\beta < 1$. Actually, the precise value of β required for full disruption depends on the internal structure of the star. Recent research conducted by Guillochon & Ramirez-Ruiz (2013) and Law-Smith et al. (2020) has revealed that stars typically require $\beta > 0.9 - 2.0$ for full disruption, taking into account differences in internal structure and the deformation and compression of stars before reaching the tidal radius. For the purposes of this dissertation, only full disruptions are considered, with $\beta = 1$ assumed to be the critical value.

After disruption, around half of the stellar gas (debris) has a positive binding energy of $\Delta\epsilon_{\rm potential}$ and becomes unbound, while the other half carries negative binding energy and remains bound (Rees, 1988). This is illustrated in Fig. 1.4, and it remains true for different β parameters since the mass-energy spread ($dM/d\epsilon$) is approximately symmetric around the specific binding energy, as long as it is a complete disruption. The bound debris then orbits around the SMBH on highly elliptical orbits. The most bound debris (i.e., the one with the smallest eccentric orbit and shortest orbital period) has a semi-major axis given by $a_{\rm MB} = -GM_H/(2\Delta\epsilon_{\rm orbit}) = R_T^2/(2R_*)$, where ϵ is the specific orbital energy, which for the most bound orbit is $\epsilon_{\rm potential}$ as in Eq. 1.17. The other debris has larger semi-major axes and longer orbital periods.

The Fallback Rate

Once the SMBH has fully disrupted a star, the bound debris returns to the disruption site on a timescale known as the fallback time. This timescale is characterised by the Keplerian orbital timescale of the most bound orbit:

$$t_{\rm FB} = 2\pi\sqrt{a^3/(GM_H)} \approx 41 \text{ days} \left(\frac{M_H}{10^6 M_\odot}\right)^{1/2} \left(\frac{M_*}{M_\odot}\right)^{-1} \left(\frac{R_*}{R_\odot}\right)^{3/2}. \tag{1.18}$$

Using the relationship between the semi-major axis and the fallback time, the specific orbital energy can be related to a characteristic time scale, t, by $\Delta\epsilon_{\rm orbit} = -GM/(2a) = -GM/\left(2(t_{\rm FB}^2 GM)^{1/3}\right) \propto -t^{-2/3}$. This lead to a mass fallback rate proportional to the following:

$$\dot{M}_{\rm FB} = \frac{dM}{d\epsilon_{\rm orbit}} \frac{d\epsilon_{\rm orbit}}{dt} \propto \frac{dM}{d\epsilon} t^{-5/3}. \tag{1.19}$$

This equation gives the classical "minus five-thirds power law" ($t^{-5/3}$) decline pattern commonly associated with TDEs. This power law decay has become a distinctive feature of TDEs. It is still used today as direct observational evidence to differentiate them from other transient phenomena, such as supernovae or gamma-ray bursts.

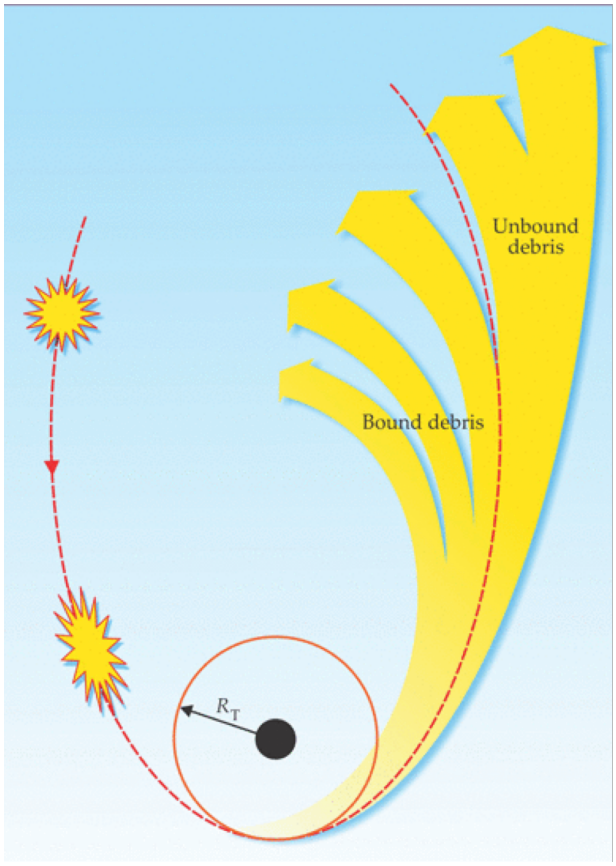

Figure 1.4: The figure depicts the aftermath of the star disruption event. As shown, roughly half of the star's gas gains orbital momentum and becomes unbound, while the other half loses orbital momentum and becomes bound in a highly elliptical orbit. The figure is adapted from Rees (1988).

To derive an analytical estimate for the mass fallback rate, it is commonly assumed that the mass distribution of the disrupted star is flat, such that the mass M_* is distributed in an energy range of $|2\Delta\epsilon_{\rm orbit}|$ (Evans & Kochanek, 1989), resulting in $dM \approx |M_*/(2\Delta\epsilon_{\rm orbit}|)d\epsilon$.

To better understand the physical magnitude of the mass fallback rate, it can be expressed in terms of the typical parameters of TDEs at the characteristic time $t_{\rm FB}$ (Phinney, 1989; Evans & Kochanek, 1989):

$$\dot{M}_{\rm FB} = \frac{1}{3}\frac{M_*}{t_{\rm FB}}\frac{d\epsilon_{\rm orbit}}{dt} = 3.3 M_\odot {\rm yr}^{-1}\left(\frac{M_H}{10^6 M_\odot}\right)^{-1/2}\left(\frac{R_*}{R_\odot}\right)^{-3/2}\left(\frac{M_*}{M_\odot}\right)^2 \times \left(\frac{t}{t_{\rm FB}}\right)^{-5/3} = \dot{M}_p \times \left(\frac{t}{t_{\rm FB}}\right)^{-5/3}. \tag{1.20}$$

Here $\dot{M}_p$ is the peak mass fallback rate, which occurs at $t \approx t_{\rm FB}$.

If the debris can quickly assemble into an accretion disk, the accretion rate will also roughly follow the mass-fallback rate. By relating the analytical fallback accretion

rate in Eq. 1.20 to the Eddington accretion rate from Eq. 1.4, it is found that the fallback rate is super-Eddington for most stellar parameters when the black hole mass is smaller than a few $\times 10^7 M_\odot$ (Rees, 1988; Evans & Kochanek, 1989; Guillochon & Ramirez-Ruiz, 2013). Specifically, the ratio of the fallback accretion rate to the Eddington rate is given by:

$$\frac{\dot{M}_{\rm FB}}{\dot{M}_{\rm Edd}} = \frac{3.3 M_\odot {\rm yr}^{-1}}{3\times 10^{-2} M_\odot {\rm yr}^{-1}} \Big(\frac{\eta}{0.1}\Big)\Big(\frac{M_*}{M_\odot}\Big)^2 \Big(\frac{M_H}{10^6 M_\odot}\Big)^{-3/2} \Big(\frac{t}{t_{\rm FB}}\Big)^{-5/3} = 140 \Big(\frac{\eta}{0.1}\Big)\Big(\frac{M_*}{M_\odot}\Big)^2 \Big(\frac{M_H}{10^6 M_\odot}\Big)^{-3/2} \Big(\frac{t}{t_{\rm FB}}\Big)^{-5/3}. \tag{1.21}$$

The system eventually transitions to sub-Eddington accretion rates at $t > t_{\rm Edd}$ with the classical "minus five-thirds power law" ($t^{-5/3}$) decay from the peak. The time at which this transition occurs is when $\dot{M}_{\rm FB}(t_{\rm Edd})/\dot{M}_{\rm Edd} \approx 1$:

$$\frac{t_{\rm Edd}}{t_{\rm FB}} \approx 19.4 \Big(\frac{\eta}{0.1}\Big)^{3/5} \Big(\frac{M_H}{10^6 M_\odot}\Big)^{-9/10} \Big(\frac{M_*}{M_\odot}\Big)^{6/5}. \tag{1.22}$$

The Accretion and Emission Processes

Early TDE studies often assume that the debris rapidly forms an accretion disk and accretes on timescales shorter than the fallback time. If this were true, the accretion rate would follow the fallback rate, indicating that the accretion process is super-Eddington. This would suggest that a super-Eddington accretion disk forms and evolves into a sub-Eddington flow typically within months to years, underscoring the significance of TDEs as a platform to test accretion physics, particularly in relation to super-Eddington accretion. Nonetheless, the rapid formation of a disk is still an active research topic and is further discussed in Section 1.3.3.

Rees (1988) and Phinney (1989) proposed that TDEs are powered by emission from a super-Eddington accretion disk. They adopted the thin disk model and predicted that TDEs are expected to be X-ray bright with temperatures ranging from 10^5 to 10^6 K, so they are best observed using X-ray telescopes in space. Assuming a constant radiative efficiency throughout the evolution of a TDE, the luminosity produced in the accretion disk can be described by the equation:

$$L_{\rm FB} = \eta \dot{M}_{\rm FB} c^2 \tag{1.23}$$

Therefore, the light curve of a TDE is expected to follow the evolution of the debris mass fallback rate. By fitting the observed luminosity as a function of time, it is then possible to estimate the black hole mass and the parameters of the disrupted star as they set the fallback rate. Examples of TDE light curves are shown in the lower right panel of Fig. 1.6. It is important to note that pre-peak and near-peak observations of TDEs play a significant role in unravelling some of the inherent model degeneracies when estimating the masses of the black hole and the disrupted star. Many current

fitting models assume that the light curves strictly follow the fallback rate at early times, which is not always the case (Mockler et al., 2019a).

1.3.2 Observational Features of TDEs

In this section, I introduce some of the most important observational features of TDE and what can be learned from them.

X-Ray and Gamma-Ray Detected TDEs

Inspired by the theoretical work pioneered by Rees (1988), observers examined archived data from the ROSAT all-sky X-ray survey and identified four galaxies that were initially X-ray dim but suddenly became X-ray bright for a short period (Bade et al., 1996; Komossa & Bade, 1999; Greiner et al., 2000). These events decayed back to non-detection over a few years. The observed luminosity (counts/s) also appears to follow the characteristic $t^{-5/3}$ behaviour, as seen in Fig. 1.5 (left panel). Furthermore, the right panel shows that the spectra can be well described by a blackbody spectrum of $T \sim 10^5$K, which would be expected if it is emitted by the innermost region of an accretion disk around a SMBH. All the observed features are consistent with the prediction for TDEs by Rees (1988).

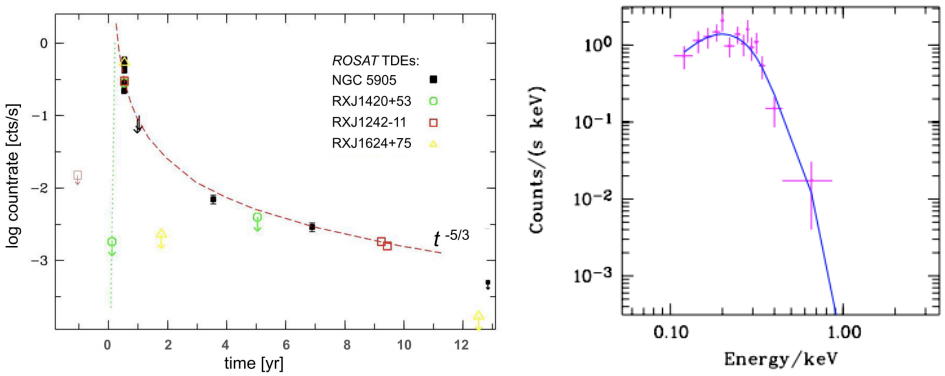

Figure 1.5: The left figure shows the light curve of four TDEs that were originally discovered using the X-ray all-sky survey ROSAT. It is evident that the count rates of each TDE approximately follow the predicted $t^{-5/3}$ decay. More surprisingly, different TDEs seem to follow it as well, which is a pure coincidence due to the detection limit. This figure is from Komossa (2015). **The figure on the right** displays the spectral energy distribution of RX J1420.4+5334. It can be seen that a blackbody source with temperatures in the range of $(3-5)\times 10^5$ K, including galactic absorption, can fit the spectra. This figure is from Greiner et al. (2000).

Later, the Swift telescope detected three TDEs (Bloom et al., 2011; Cenko et al., 2012; Brown et al., 2015) producing very large non-thermal X-ray fluxes, which are believed to originate from viewing the source along the relativistic jets produced from the transient disks. The existence of the jet and relativistic beaming effects are based on the extreme luminosity inferred by assuming isotropic X-ray emission, as well as

the accompanying synchrotron emission detected in radio bands. These events represent a distinct subgroup of X-ray TDEs, often referred to as relativistic or jetted TDEs. The study of their jet properties and evolution provides critical insights into particle acceleration and jet launching mechanisms.

Optically Detected TDEs

Thanks to the advent of optical all-sky surveys, the number of optical TDEs has recently become dominant, surpassing the number detected through other bands, as shown in the upper left panel of Fig. 1.6. However, the optical detection of TDEs poses a few challenges to the classical TDE theory.

One discrepancy between observation and theory is the temporal evolution of the emission. For many optical TDEs, the observed light curve in a given optical/UV band follows the classical $t^{-5/3}$ pattern, as shown in the upper right panel of Fig. 1.6. The monochromatic optical/UV fluxes should not follow this trend, at least not initially when the temperature of the outer disk peaks at higher energies than the UV/optical regime (Lodato & Rossi, 2011). The emission in a monochromatic optical/UV band should decay following $t^{-5/12}$ as predicted by Lodato & Rossi (2011); Lodato et al. (2015). This is because the optical/UV emission from the disk should arise from the Rayleigh–Jeans part of the accretion disk spectrum, where the luminosity is proportional to the temperature, which is proportional to $(\dot{M})^{1/4}$ (Eq. 1.8), so $L_\nu \propto B_\nu(T) \propto T_{\rm disk} \propto (\dot{M}_{\rm Edd})^{1/4} \propto (t^{-5/3})^{1/4} = t^{-5/12}$ (Lodato & Rossi, 2011). Therefore, only the inferred optical blackbody luminosity (see the Sec. 1.3.2 for definition and the bottom right panel of Fig. 1.6 for illustration) or the X-ray luminosity should follow the $t^{-5/3}$ when modelling the emission using a classical thin accretion disk.

In summary, the behaviour of the observed optical light at early times cannot be fully explained by standard thin disk models. However, as the accretion rate declines and the TDE enters the sub-Eddington regime, Mummery & Balbus (2020) showed that the late-time optical/UV and X-ray light curves could be explained by a geometrically thin disk with declining accretion rates. This suggests the presence of a different emission structure in the optical at early times, which is further discussed in Section 1.3.3 (and investigated in Chapter 5 and particularly Fig. 5.4).

Inferred Blackbody Parameters

These optical all-sky surveys take large field images in different band filters every few hours to days (Graham et al., 2019). Therefore, when a TDE is detected by its transient nature, astronomers often only possess the band filter observations. The primary modelling, which can be done with this, is to fit blackbody spectra to the SED consisting of the band filters observed from a similar period in time. An example of this procedure is shown in the bottom left panel of Fig. 1.6.

Once a blackbody fit has been obtained, the temperature, radius, and luminosity of a TDE can be inferred. The high cadence of all-sky surveys allows for the evolution

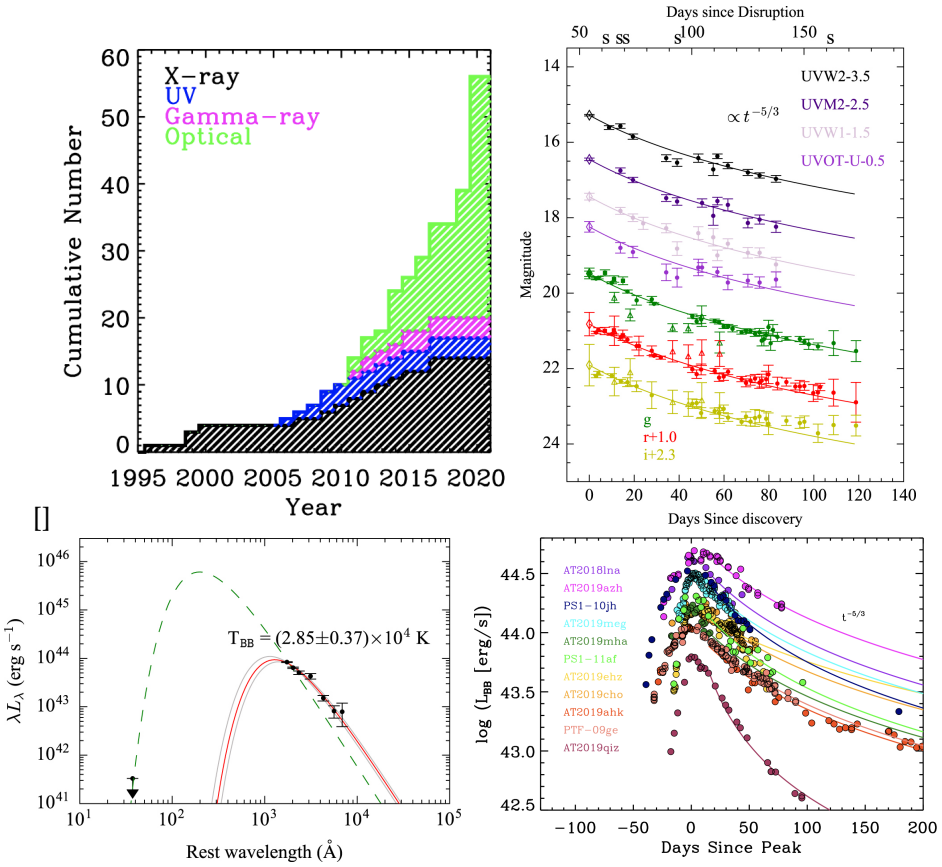

Figure 1.6: The top left figure illustrates the cumulative detection of TDEs as a function of years, with the colour denoting the first detection in X-ray (grey), UV (blue), gamma-ray (magenta), and optical (green). This figure is from Gezari (2021). **The figure on the top right** shows the monochromatic light curves for the TDE iPFT16axa observed at a specific filter. Noticeably, the band filter also exhibits a $t^{-5/3}$ decay, which is unexpected for early times in a thin disk model. The figure is Hung et al. (2017). **The bottom left figure** depicts the spectral energy distribution (SED) of iPFT16axa in different UV/optical bandpasses at a given time. The SED is fitted with a blackbody function, from which a temperature is obtained. For optical observations, this temperature is typically a few 10^4 K. The figure is from Hung et al. (2017). **The figure on the bottom right** displays the inferred blackbody luminosity light curves of TDEs that were detected before reaching their peak. It can be seen that an excellent fit to the $t^{-5/3}$ decay is observed. This figure is from Gezari (2021).

of these parameters to be probed, as illustrated in Fig. 1.7. An important feature to note in TDEs is that, after the peak, the temperature remains roughly constant even as the luminosity falls by an order of magnitude. For typical accretion processes, this implies a lack of cooling mechanisms as the accretion rate drops. Therefore, the photosphere radius must correspondingly decrease to account for the decreasing luminosity.

In addition, the fitted photosphere radii of TDEs are typically more extensive than what would be expected for a compact accretion disk structure with a size corresponding to the circularisation radius $R_c \approx 2R_T$ (Rees, 1988), which corresponds to a circular

orbit with the same specific angular momentum as the stellar orbit. However, the inferred photosphere radii are orders of magnitude larger (Gezari, 2021). This mismatch poses another challenge for early TDE theory.

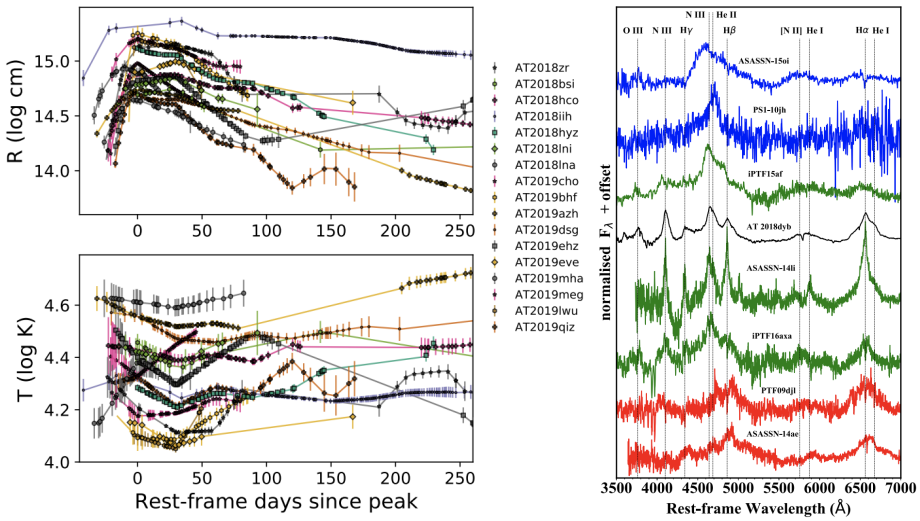

Figure 1.7: The left-hand side panel shows the evolution of the inferred blackbody parameters (radius, R, and temperature, T) for the 17 TDEs monitored with ZTF. The figure is from van Velzen et al. (2020). **The right-hand side figure** shows example spectra of TDEs. Blue is TDE He, green is TDE Bowen, and red is TDE H. The last class, TDE featureless, is not shown as it is easy to visualise. The figure is from (Leloudas et al., 2019)

Spectral Classification

After detecting a TDE candidate, researchers conduct more detailed follow-up observations to obtain high-resolution spectra. It is found that optical TDEs often produce broad emission lines with widths of $\sim 10^4$ km/s. Four different classes have been observed based on the spectroscopic features (Leloudas et al., 2019; van Velzen et al., 2020; Hammerstein et al., 2023) and are illustrated in the right panel of Fig. 1.7, they are:

- TDE H: Characterised by strong and broad hydrogen emission lines
- TDE He: Characterised by strong and broad helium emission lines
- TDE Bowen (also known as TDE H+He): Characterised by broad NIII and/or OIII line structures, which are usually also accompanied by strong and broad hydrogen and helium emission lines
- TDE featureless: Characterised by no broad line detection.

These spectra, specifically the line shape and strengths, provide valuable information about the physical parameters of the gas in which the lines are emitted, as different lines are present depending on the ionisation state. Two of the more surprising lines in TDEs are the Bowen OIII and NIII lines, which occur through the Bowen mechanism. The

Bowen mechanism requires resonant absorption and a lot of UV and HeII ionisation (Bowen, 1934; Leloudas et al., 2019).

Outflows in TDEs

Blueshifted broad absorption lines have recently been found in the UV spectra of TDEs (Cenko et al., 2016; Hung et al., 2021), and P-Cygni line profiles have been observed in X-rays (Kara et al., 2018). The absorption is typically rather broad and significantly blueshifted, with both velocity and broadening ranging from 10^3 to 10^4 km/s. This blueshift is typically larger than that inferred from optical emission lines (Hung et al., 2021), providing strong evidence for the presence of fast, powerful outflows in TDEs. Understanding the wind structure in TDEs is essential for fully characterising these events.

Case Studies

This section focuses on two specific TDEs that were observed with high-cadence, multi-band observations. These events will be further discussed later in this dissertation when comparing my models to the observed data.

Case Study I Swift J1644

Swift J1644 is a jetted TDE that exhibits X-ray reverberation signatures indicative of a super-Eddington accretion flow (Kara et al., 2016b). The upper left panel of Fig. 1.8 shows a highly blueshifted line around 7.5-8.5 keV, while further X-ray reverberation studies revealed a relativistic broadened Fe Kα line shown in the upper right panel of Fig. 1.8. Both observations suggest high-velocity gas with a velocity greater than 0.1c. In the standard thin disk picture, the Doppler blueshift is thought to arise from the rotational disk, implying a high inclination angle (edge-on) to explain the blueshift. However, the detection of beamed X-ray emission from the jet toward our line-of-sight suggests a low (face-on) inclination angle (Bloom et al., 2011; Burrows et al., 2011), as the jet is usually believed to be perpendicular to the disk. This makes the classical picture of Fe K lines reflected from a thin disk incompatible with the viewing angle constraints given by the jet. However, as TDEs can produce super-Eddington accretion, strong winds are expected to be present. Thus, if the Fe Kα line is due to the reflection of fast-moving winds, the viewing angle discrepancy can be overcome, which was first proposed by Kara et al. (2016b). I conducted more theoretical modelling related to this aspect, which is presented in Chapters 3 and 4.

Case Study II ASASSN-15oi

ASASSN-15oi is a notable TDE with peculiar features. It was first detected as an optical TDE, and at early times the UV and optical emissions follow the canonical $t^{-5/3}$ power law decay behaviour associated with TDEs (Holoien et al., 2016a). It also exhibited weak, nearly constant X-ray emissions during the first 100 days. However, follow-up observations by Gezari et al. (2017) revealed an intriguing trend in the X-ray flux

of ASASSN-15oi. As shown in the lower left panel of Fig. 1.8, the X-ray emission increased at late times and reached a peak roughly 400 days after the optical peak. Similar X-ray brightening has been observed in a few other initially optically strong TDEs (Gezari et al., 2017; Kajava et al., 2020; Liu et al., 2022). Additionally, the inferred optical blackbody luminosity over the X-ray luminosity between $0.2 - 10$ keV, shown in the lower right panel of Fig. 1.8, decreased steadily until 300 days, at which point the optical and X-ray luminosities became similar. Different theoretical models have been proposed to explain this peculiar behaviour, including the one I propose in Chapter 5.

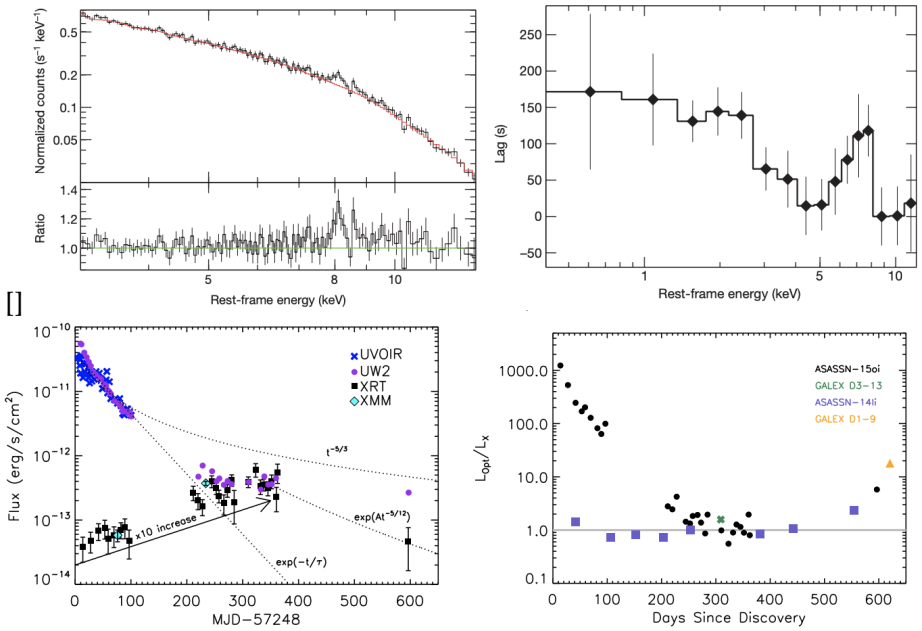

Figure 1.8: The upper left figure displays a weak and narrow Fe Kα line detected in the X-ray reflection of the TDE Swift J1644. The Fe line profile is highly blueshifted, with peak energy around 8keV, indicating relativistic blueshift/outflow. This figure is from Kara et al. (2016b). **The figure on the upper right** shows a broad Fe Kα line profile in the energy-lag spectra due to X-ray reverberation in the TDE Swift J1644. The Fe line in the energy-lag is much broader than the spectral line, indicating relativistic broadening. This figure is also from Kara et al. (2016b). **The lower left figure** depicts the UV and X-ray flux of the TDE ASASSN-15oi. The UV flux decays steadily, while the X-ray flux increases in strength to roughly 400 days before it decays. This figure is from Gezari et al. (2017). **The figure on the lower right** shows the X-ray brightening of ASASSN-15oi by visualising the ratio of the inferred optical luminosity to the X-ray luminosity. The optical luminosity is calculated based on the optical blackbody fit, and the X-ray luminosity is the flux in the $0.2 - 10$ keV band. After roughly 100 days, the optical and X-ray have equal strength. This figure is also from Gezari et al. (2017).

1.3.3 Recent Theoretical Development

Many new models and numerical simulations have been carried out in the past two decades to account for the mismatch between the observed features of TDEs and the canonical models mentioned in the previous section. In particular, it is important to

note that up to now, self-consistent simulations of TDEs have yet to be conducted due to the complexity of the problem and the huge computation cost needed. Instead, researchers have conducted studies focusing on different phases of the event, which require different physics to be resolved. This highlights the uncertainty in our understanding of TDEs and the need for more sophisticated modelling using next-generation codes.

Below I briefly mention the recent models and simulations in the following topics:

- Disruption
- Circularisation /disk formation
- Accretion
- Emission

Disruption

In recent years, sophisticated hydrodynamical simulations can allow TDE modellers to better resolve the deformation that a star undergoes on the way to the black hole and the compression and shocks during disruption (e.g. Lodato et al., 2009; Guillochon & Ramirez-Ruiz, 2013). They found that the overall accretion rate is slightly lower than the analytical estimate, yet still being super-Eddington for typical parameters. Close to the peak, the fallback rate sensitively depends on the parameters such as the stellar structure and pericenter distance and can deviate slightly from the canonical $t^{-5/3}$. Most recently, Law-Smith et al. (2019); Golightly et al. (2019); Law-Smith et al. (2020) adopted more realistic stellar profiles obtained from MESA (Paxton et al., 2011) instead of using the standard polytropic stellar structure. This approach incorporates different evolutionary stages of stars, predicting the abundance of metals falling back over time (Law-Smith et al., 2019). While most of these parameter studies use Newtonian calculations, general relativistic corrections are only necessary if the encounter is highly relativistic with $R_p < 10R_g$ (Tejeda et al., 2017; Stone et al., 2019).

Circularisation/Disk Formation

Post disruption, the bound debris is highly elliptically, and they are conventionally assumed to go through the "circularisation process" to form a disk (see a review by Bonnerot & Stone, 2021). This means excess orbital energy of the stellar debris must be removed before settling into a circular disk. Furthermore, for the accretion rate to closely follow the fallback rate in TDEs, the circularisation timescale and the viscous/accretion timescale are assumed to be smaller than the fallback timescale (Rees, 1988). However, the circularisation timescale and efficiency are still actively debated.

Shocks are the primary mechanism by which the gas can dissipate some of the excess energy. There are two major shock sites. First, the nozzle shock occurs as debris goes through the pericentre for the second time, where they are vertically compressed

(Guillochon et al., 2014). Second, after passing through the pericentre an experiencing the nozzle shock, the out-going debris stream can cross the in-going stream due to GR apsidal precession (Shiokawa et al., 2015; Dai et al., 2015; Guillochon & Ramirez-Ruiz, 2015; Bonnerot et al., 2016). For TDEs around SMBHs, the self-crossing shock is typically the stronger driver for circularisation (Guillochon et al., 2014; Bonnerot et al., 2021).

The simulations of the disruption and circularisation processes are challenging since physics happens on vastly different scales and needs to be resolved simultaneously. To lower the computational cost, one approach is to use a smaller mass ratio of the black hole and star (e.g. Ramirez-Ruiz & Rosswog, 2009; Shiokawa et al., 2015) or an initial bound elliptical stellar orbits (e.g. Sądowski et al., 2016; Hayasaki et al., 2016; Bonnerot et al., 2016). However, it is unclear how to use these results to interpret normal TDEs with initial parabolic orbits and realistic mass ratios. Another approach adopted by Lu & Bonnerot (2020) and Bonnerot et al. (2021) is to split the process into two simulations, one global simulation and one local with high resolution, to focus on the stream-stream collision itself. They found that circularisation can be somewhat efficient, and depending on the disruption parameters, around 2% to 33% of the initially bound material can become unbound due to the shocks happening after the stream-stream collision. Very recently, Steinberg & Stone (2022) attempted to simulate the entire TDE process using an adaptive moving mesh code. They also found that circularisation can be efficient, and about 15% of the bound debris becomes unbound. However, more research is needed on this topic since none of the simulations mentioned above includes magnetic fields, which are crucial for resolving the accretion process and likely to impact the circularisation efficiency. Nonetheless, these results show that, at least in some TDE parameter space, circularisation is likely to happen rapidly and efficiently. The efficiency of the circularisation process is also related to the emission mechanisms available, as I will discuss later.

Accretion

The debris will eventually form an accretion disk. If the circularisation process is moderately efficient, it preserves some signatures from the fallback rate, such as the accretion rate being super-Eddington and somewhat following the fallback rate.

There exist a few semi-analytical models for describing TDE disks. For example, since the debris carries low angular momentum, quasi-spherical models such as the ZEBRA model were proposed (Loeb & Ulmer, 1997; Coughlin & Begelman, 2014). Another approach is to consider an ad hoc slim/thin disk + outflow model (Strubbe & Quataert, 2009; Lodato & Rossi, 2011; Metzger & Stone, 2016) or assume a spherical wind profile envelope (Roth et al., 2016).

With advances in numerical codes related to super-Eddington accretion, as discussed in Section 1.1.3, Dai et al. (2018) conducted a simulation using `HARMRAD` (McKinney et al., 2014) of a super-Eddington accretion flow with parameters similar to those

expected in TDEs. Other groups also simulated super-Eddington TDE disk structures with different parameters, such as Curd & Narayan (2019). These simulations all show that strong and dense winds are expected to launch from such disks.

On the other hand, if the debris takes a long time to circularise, an elliptical accretion disk might form (Svirski et al., 2017). Such disks have been used to explain some of the TDE observational signatures. Yet, the geometry and physics of elliptical accretion disks still need to be better understood, as such disks have yet to be resolved in simulations.

Emission

While the X-ray emissions from TDEs should originate from the accretion disks and jets, the optical emission origin is still under debate. Two main groups of models explain the optical emission: reprocessing and shocks.

For the first model, the reprocessing materials could be the winds produced in the super-Eddington accretion or disk formation process. The X-ray emission originating from the inner disk must pass through the wind before being observed, and absorption and scattering in the wind shift photon energies to lower levels. This mechanism explains why some TDEs are observed in the optical range (dense winds) while others are detected in X-rays (dilute winds). Models incorporating this description include those presented in Loeb & Ulmer (1997), Strubbe & Quataert (2009), Lodato & Rossi (2011), Metzger & Stone (2016), Roth et al. (2016), Dai et al. (2018), and Curd & Narayan (2019).

In particular, this thesis heavily relies on the model presented in (Dai et al., 2018). The authors used the Monte Carlo Radiative Transfer Code Sedona Kasen et al. (2006) to calculate synthetic spectra produced from the super-Eddington disk-wind configuration after a TDE. The authors found that the SED of the escaped emission is a function of the viewing angle. Specifically, the wind is dilute at low inclinations (face-on), and X-rays are primarily observed. At higher inclinations, however, the X-rays are reprocessed into optical radiation. At intermediate viewing angles, both X-ray and optical radiation are observed. The authors propose a TDE unification model in which the observation of distinct classes of TDEs is a viewing angle effect, similar to the AGN unification model. This model suggests that the observed X-ray to the optical event in TDEs may be a complex interplay of viewing angle and reprocessing mechanisms and that understanding this interplay is necessary for a complete understanding of these phenomena. A schematic illustration of the viewing angle dependence is shown in Fig. 1.9. The authors presented three reprocessing mechanisms to explain the observed X-ray to the optical event: atomic reprocessing, adiabatic expansion, and Comptonisation (for more details see Appendix C.2).

The other model mainly applies to the case of inefficient circularisation, when standard circular accretion disks cannot be produced. This was first proposed by Piran et al. (2015) that the shocks produced during streams crossing themselves might be powerful enough to explain the luminosities and temperatures of at least a subset of optical

TDEs. However, sophisticated modelling is lacking for this model, so it is unclear if the emission follows the $t^{-5/3}$ power law as observed or if the observed TDE SED and emission lines can be reproduced in this model. Furthermore, the delayed accretion rates and efficiency lack detailed modelling, although this has been used to explain X-ray brightening events such as ASASSN-15oi.

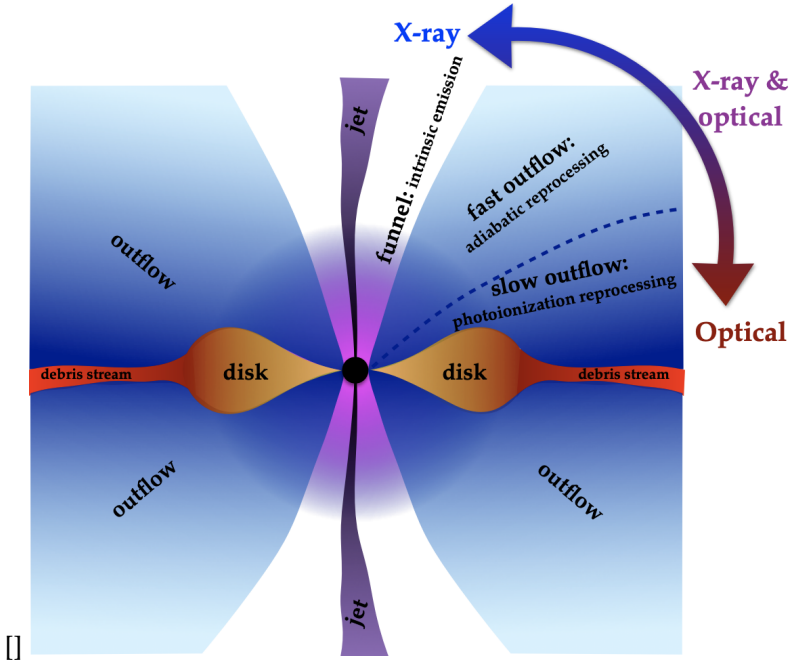

[]

Figure 1.9: The figure depicts the disk-wind geometry of a super-Eddington accretion source, specifically a TDE, and illustrates how observed emission is dependent on the viewing angle, as proposed in the TDE unification model. The basic geometry consists of a thick disk with slower, denser disk winds near the equatorial plane and faster winds towards lower inclinations. X-ray TDEs are expected to be observed through an optically thin funnel near the pole, where the emitted X-rays do not undergo significant reprocessing. However, if the observer views the TDE edge-on through the disk or slow winds, all X-ray photons are reprocessed, resulting in EUV/optical emission. At intermediate inclination angles, X-rays and optical emission can be observed simultaneously from a TDE. The figure is from Dai et al. (2018).

1.4 Outline

In the previous sections of Chapter 1, I first delved into the complexities of accretion physics. I introduced the X-ray reverberation technique, which offers a unique approach to constraining the inner accretion flow geometry. I also introduced the theory and observations of TDEs, which are ideal targets for testing extreme accretion and outflow physics.

In Chapter 2, I present methods for calculating emission signatures from an accretion flow. Specifically, I introduce the GR ray-tracing code, which I use to compute the X-ray reverberation signals from super-Eddington structures. Additionally, I briefly

discuss solving the radiative transfer equation using a Monte Carlo method, which I employ to calculate the SED and line emission of super-Eddington disk structures for comparison to TDE observations.

In Chapter 3, I present my work on how the Fe Kα line in a super-Eddington setting is reflected. I demonstrate that the Fe Kα line profiles produced in a super-Eddington setting are morphologically distinct from those produced in thin disks, particularly in parameters such as the blueshift and symmetry of the line profile.

In Chapter 4, I examine the X-ray reverberation temporal signatures produced from super-Eddington geometry and find that the Fe lines respond much faster to variations in the driving flux for super-Eddington disks than for thin disks. I identify other parameters differentiating the two geometries, such as the energy-lag spectra between two narrow frequency ranges. Furthermore, I provide the first quantitative evidence that a self-consistent super-Eddington model can better explain the detection of Swift J1644 than a thin disk model.

In Chapter 5, I use super-Eddington accretion disks with different accretion rates to examine the dynamical evolution of TDEs. I apply post-processing onto simulated disk structures using the advanced radiative transfer code Sedona. The results allow me to explain the diversity and evolution of TDE emissions. I also show that our model can explain the range of inferred TDE blackbody parameters as observed. Furthermore, I explain why some optical TDEs brighten in X-rays at late times based on reprocessing model.

Chapter 2

Methods: Radiative Transfer

The information we can extract from observations of astrophysical systems relies heavily on our understanding of electromagnetic radiation. To interpret these observations, we must model the production and transport of radiation. Therefore, radiative transfer is a fundamental process in astrophysics that describes how electromagnetic radiation propagates through and interacts with matter. In this section, I introduce the radiative transfer methods that I use in the later chapters to calculate various observational features from extreme black hole accreting systems. Specifically, I focus on calculating the general relativistic (GR) broadening and time delay of Fe lines in Section 2.1, and the spectral energy distribution (SED) of a given disk/wind structure in Section 2.2. These calculations enable me to test theoretical models against observations and provide insights into the physical processes that govern the behaviour of astrophysical systems.

2.1 Modelling the Fe K Line

Part of Section 2.1.2 builds upon the Appendix published by Thomsen et al. (2022a), which is presented in Chapter 4.

The Fe Kα line is a prominent spectral feature observed in the X-ray spectra of many astrophysical sources, such as Active Galactic Nuclei (AGNs) and X-ray Binaries (XRBs). This line is produced due to high-energy coronal photons photoionising Fe K-shell electrons from the accretion disk. This creates a vacancy in the K-shell, which is then filled by an L-shell electron and emission of the Fe Kα photon. However, since Fe lines are generated in the strong gravitational field near the black hole, GR effects must be considered to accurately describe their shape and strength.

Modelling the Fe line is a complex task involving describing the initial line strength (emissivity), its broadening due to different physical processes, and the transportation of rays between the source and an observer in a GR environment. This section explores GR ray-tracing techniques for modelling the Fe Kα line by considering the effects of strong gravity, such as light bending, Doppler and gravitational redshifts, and Shapiro time delays.

2.1.1 Strength of the Fe Lines

The process of producing Fe lines is well understood, but determining the location and strength of the lines through detailed radiative transfer modelling is challenging. Early studies only considered the Fe line production without accounting for the other parts of the spectrum (e.g. Fabian et al., 1989; Matt et al., 1991; Reynolds & Begelman, 1997), but more recent research has taken the entire X-ray continuum into account (Ross & Fabian, 2005; García et al., 2014). To do this, the authors first calculate the emission lines from infinite slabs in the Newtonian regime (García et al., 2013) and then apply GR ray-tracing codes to describe how the individual lines are blurred, such as in work by Dauser et al. (2013).

When considering only the Fe line, the detailed state of the gas is not required, and the initial strength of the emission line is usually assumed to be proportional to the incoming irradiation flux of the corona onto the accretion disk. This assumption is based on the intuition that the rate of Fe K-lines should be directly related to the photoionisation process, which is given by the irradiating flux, F_x. Therefore, the emissivity profile of the Fe Kα line is assumed to be: $\epsilon \propto F_x$.

Emissivity Profile

In Newtonian geometry, the emissivity profile can be analytically calculated assuming the lamppost geometry shown in Figure 1.3, with the corona located at a height h_{LP} above the black hole. The resulting emissivity profile is described by the expression:

$$\epsilon_{\mathrm{Newton}} = \frac{L_x \cos(\psi)}{4\pi d^2} \propto \frac{\cos(\psi)}{r^2 + h_{\mathrm{LP}}^2} = \frac{h_{\mathrm{LP}}}{(r^2 + h_{\mathrm{LP}}^2)^{3/2}}, \tag{2.1}$$

where L_x is the X-ray luminosity that can ionise the Fe K-shell electrons, d is the distance from the corona to a specific radius of the disk r, and $\cos(\psi)$ is the angle between the path of the coronal photons and the normal to the disk surface. The last part of the equation is obtained using thin disk geometry, for which the emissivity decreases as r^{-3} at large distances from the corona ($r \gg h_{\mathrm{LP}}$). It is intuitive that more Fe lines should be produced in the inner disk than those further out due to the more extensive irradiation of the inner disk. This approach to line strength is adopted in Thomsen et al. (2019) and is presented in Chapter 3.

However, in a GR setting, the irradiation profile is more complex and requires full GR ray-tracing simulations to account for the light-bending effect and other GR effects. A rigorous GR emissivity profile is given by (Wilkins & Fabian, 2012):

$$\epsilon_{GR} = \frac{g^2 N(r, dr)}{\gamma A(r, dr)}. \tag{2.2}$$

Here, r is the distance from the black hole to the disk, and $N(r, dr)$ is the number of photons hitting an annulus of the disk at r with thickness dr and corresponding proper area $A(r, dr)$. The Lorentz factor γ accounts for the disk's motion with respect to the

stationary observer. The energy shift g of photons from the corona to the disk is given by:

$$g = \frac{E_{\rm obs}}{E_{\rm emit}} = \frac{\left(p_\mu u^\mu\right)_{\rm obs}}{\left(p_\nu u^\nu\right)_{\rm emit}}, \tag{2.3}$$

where $E_{\rm obs}$ is the photon energy observed by the disk elements, and $E_{\rm emit}$ is the energy of the photon emitted from the corona. The four-momentum and velocity of the gas are denoted by p^μ and u^μ, respectively. A GR ray-tracing simulation is required to account for the light-bending effects in N and calculate the change in energy, g. This rigorous GR calculation of the emissivity is used in Thomsen et al. (2022a) to calculate the Fe line profile in thin and super-Eddington disk settings, as presented in Chapter 4.

2.1.2 General Relativistic Ray-Tracing

The gravity of a black hole is so strong that it warps the space-time nearby, causing a space-time curvature that affects the path of light passing near it to no longer follow straight lines. This means that accurate descriptions of the propagation of light near a black hole require a sophisticated tool such as a GR ray-tracing code.

Code Equations

To calculate the photon trajectory from the corona to the emitting gas and from a far-away stationary observer to the emitting gas, I employ a GR ray-tracing code based on Dai (2012) and use equations from Fuerst & Wu (2004). It utilises the Boyer-Lindquist coordinate, which describes the space-time around a rotating (Kerr) black hole with the line element, ds^2, as:

$$ds^2 = -\left(1-\frac{2r}{\Sigma}\right)dt^2 - \frac{4ar\sin^2\theta}{\Sigma}\,dt\,d\phi + \frac{\Sigma}{\Delta}\,dr^2 + \Sigma\,d\theta^2 + \left(r^2+a^2+\frac{2a^2r\sin^2\theta}{\Sigma}\right)\sin^2\theta\,d\phi^2, \tag{2.4}$$

where (t, r, θ, ϕ) is the BL spherical coordinates, a is the dimensionless spin parameter and $\Delta = r^2 - 2\,r + a^2$ and $\Sigma = r^2 + a^2\cos^2\theta$. Here the geometric unit ($G = M = c = 1$) is used.

In this code, the geodesic of particles is calculated by evolving the six variables $t, r, \theta, \phi, p_r, p_\theta$ using the equations given below:

$$\begin{aligned}
&p_t = -E \quad \dot{t} = E + \frac{2r(r^2+a^2)E - 2aL}{\Sigma\Delta} \\
&p_r = \frac{\Sigma}{\Delta}\dot{r} \quad \dot{p}_r = \frac{(r-1)\left((r^2+a^2)H - \kappa\right) + rH\Delta + 2r(r^2+a^2)E^2 - 2aEL}{\Sigma\Delta} - \frac{2p_r^2(r-1)}{\Sigma} \\
&p_\theta = \Sigma\dot{\theta} \quad \dot{p}_\theta = \frac{\sin\theta\cos\theta}{\Sigma}\left(\frac{L^2}{\sin^4\theta} - a^2(E^2+H)\right) \\
&p_\phi = L \quad \dot{\phi} = \frac{2arE + (\Sigma - 2r)L/\sin^2\theta}{\Sigma\Delta}
\end{aligned} \tag{2.5}$$

Here, p_t and p_ϕ are constants of motion representing the conservation of energy, E, and angular momentum around the spin axis, L. Additionally, H is a constant twice the Hamiltonian, 0 for photons and -1 for massive test particles. The last constant is $\kappa = Q + L^2 + a^2(E^2 + H)$, where Q is Carter's constant given by $Q = p_\theta^2 - a^2 E\cos^2\theta + L^2\cot^2\theta$. These six variables are evolved with a standard 5th-order Runge-Kutta integrator.

The GR ray-tracing code automatically accounts for the important line-broadening effects, such as Doppler shifts and gravitational reddening, as well as gravitational time delays (Shapiro time delays) through the photon's 4-momentum vector. These effects arise from the strong gravitational fields near a black hole and can significantly alter the observed properties of light emitted from a source near a black hole. For example, gravitational redshift causes the wavelength of light to stretch as it travels away from a strong gravitational field, resulting in a shift towards longer wavelengths (redshift). This effect is illustrated on the right-hand side of Fig. 1.3. In the following section, I outline how to utilise this code to perform ray-tracing calculations.

Tracing Photons Travelling from the Corona to the Disk

In order to obtain the emissivity profile in Eq. 2.2, I use the conventional lamppost model, which assumes that the corona is a point source that radiates isotropically in its local frame. Note that this does not mean that the corona emits isotropically in a faraway observer's (BL coordinate) frame. Therefore, to describe the coronal emission, I need to express the local isotropic emission in the coordinate frame of the ray-tracing code.

Isotropic radiation by a point source in the Minkowski space-time (denoted with hat) can be achieved by emitting photons in equally spaced solid angles of $d\hat{\Omega}$:

$$d\hat{\Omega} = \sin(\alpha) d\alpha d\beta = -d(\cos(\alpha)) d\beta, \tag{2.6}$$

where α is the declination angle from the polar axis and β is the azimuthal angle. Therefore, radiating isotropically in Minkowski space can be approximated by sampling random values of $\cos(\alpha) \in [-1, 1]$ and $\beta \in [-\pi, \pi]$. Suppose a photon with energy E_0 is emitted with angles α and β. In that case, its energy-momentum 4-vector is found by the standard spherical projection of the solid angles to the Minkowski coordinate tetrad $(\hat{t}, \hat{x}, \hat{y}, \hat{z})$ to be:

$$\hat{p} = \dot{x} = \left(p^{\hat{t}}, p^{\hat{x}}, p^{\hat{y}}, p^{\hat{z}}\right) = E_0\Big(1, \sin(\alpha)\sin(\beta), \sin(\alpha)\cos(\beta), \cos(\alpha)\Big), \tag{2.7}$$

where I have used $p^\mu = \frac{dx^\mu}{d\lambda} = \dot{x^\mu}$ for massless particles.

According to GR, one can shift the reference frame to the local reference frame (e.g. the corona), so the metric reduces to that of Minkowski space:

$$\eta_{\hat{\alpha}\hat{\beta}} = e^\mu_{\hat{\alpha}} e^\nu_{\hat{\beta}} g_{\mu\nu} = \mathrm{diag}(-1, 1, 1, 1). \tag{2.8}$$

The transformation matrix is sometimes referred to as the 'vierbein (four legs) matrix' since it consists of four vectors ($e^{\mu}_{\hat{\alpha}}$), which make up the (4×4) transformation matrix. Each of the four legs is normalised and orthogonal to the others. The transformation matrix for arbitrary coronal point sources orbiting with the four-velocity is $\vec{u} = u^t(1, 0, 0, \Omega)$ around a Kerr black hole is derived in Appendix B.1.1. The momentum transformation between the local reference frame of a rotating observer and the coordinate frame is given by:

$$p^{\mu} = \frac{dx^{\mu}}{d\lambda} = \dot{x^{\mu}} = e^{\mu}_{\hat{\mu}} \hat{p^{\mu}}, \tag{2.9}$$

where $\hat{p^{\mu}}$ is the four-momentum expressed in the local tetrad basis, and p^{μ} is the transformed four-momentum expressed in the global coordinate frame.

From Eq. 2.9, the initial conditions of isotropic emission from a stationary coronal source in the code coordinates become:

$$\begin{aligned}
\dot{t}_{\text{STATIONARY}} &= p^t = e^t_{\hat{t}} p^{\hat{t}} + e^t_{\hat{x}} p^{\hat{x}} = \frac{-E_0}{\sqrt{-g_{tt}}} + \frac{E_0 \sin(\alpha)\cos(\beta)}{\sqrt{g_{\phi\phi}\left(\frac{g_{tt}}{g_{t\phi}}\right)^2 - g_{tt}}} \\
\dot{r}_{\text{STATIONARY}} &= p^r = e^r_{\hat{z}} p^{\hat{z}} = E_0 \cos(\alpha)\sqrt{\frac{\Delta}{\Sigma}} \\
\dot{\theta}_{\text{STATIONARY}} &= p^{\theta} = e^{\theta}_{\hat{y}} p^{\hat{y}} = \frac{E_0 \sin(\alpha)\sin(\beta)}{\sqrt{\Sigma}} \\
\dot{\phi}_{\text{STATIONARY}} &= p^{\phi} = e^{\phi}_{\hat{x}} p^{\hat{x}} = \frac{-E_0 \sin(\alpha)\cos(\beta)}{\sqrt{g_{\phi\phi} - \frac{(g_{t\phi})^2}{g_{tt}}}}.
\end{aligned} \tag{2.10}$$

From these equations, one can obtain the three constants of motion (E, L, Q), which can be used to evolve the 6 equations of motion to simulate isotropic emission from the corona. A ray-tracing simulation illustrating how local isotropic radiation looks in GR is presented in Fig. 2.1. Here, light-bending effects towards the black hole are clearly seen as the photons no longer travel in a straight line due to the curvature of spacetime. After such a simulation, the emissivity profile (Eq. 2.2) is calculated by considering the radial number distribution of photons hitting an annulus $N(r, dr)$ and the energy shift, g, which is obtained as a dot product of photon energy-momentum vector from the ray-tracing code and the 4-velocity of the disk/corona.

Tracing photons travelling from disk to observer

Forward ray-tracing, starting from the accretion disk, requires tracing all the photons at each disk position that can hit our telescope. However, this process is time-consuming as most photons travel in other directions. To address this, one can use the backward ray-tracing method, in which an image plane can be placed at the same inclination to the accretion disk as the telescope and located far enough away such that photons passing through it travel in straight lines. By setting the image plane at a distance of $r = 10^3 - 10^4 R_g$ away from the source, only photons hitting the image plane perpendicular

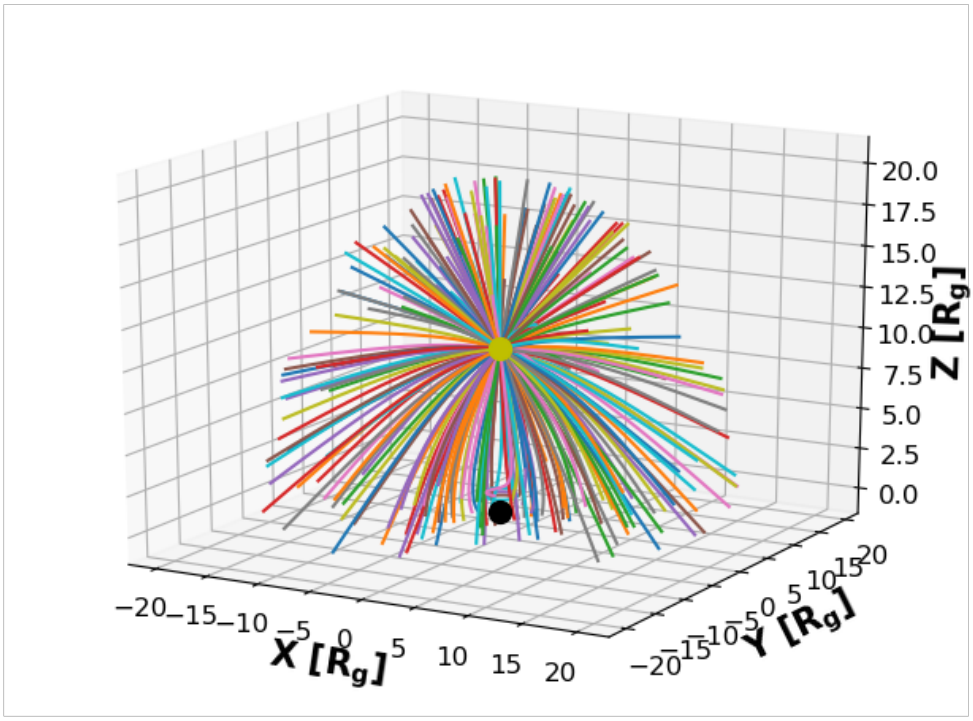

Figure 2.1: This figure shows the trajectory of photons from a stationary lamppost corona source located at $z = 10\ R_g$ as calculated by our GR ray-tracing code. 250 isotropically emitted photons from the corona have been traced around a maximally spinning black hole with $a = 0.998$. The corona and the black hole are represented by the large yellow and black circles, respectively. The GR effect of light bending is observed through the curved photon trajectories towards the black hole. Furthermore, close to the black hole, the frame-dragging effects of the maximally spinning Kerr black hole can be seen, which produce the characteristic twisted path.

can reach the telescope. Therefore, only these photons need to be initialised from the image plane.

Backward ray-tracing allows us to correlate each pixel on the image plane with a location in the accretion flow. Combining this with the local velocity of the disk, the energy shift can be determined, and the emitted intensity of the Fe line can be calculated from the emissivity profile at that radius. Louisville's Theorem can be applied to convert the emitted line strength into the observed one. This theorem states that I_ν/ν^3 remains constant along the ray, enabling the relationship between the emitted and observed intensities (Cunningham, 1975):

$$I_{\nu,\mathrm{obs}} = g^3 I_{\nu,\mathrm{emit}} \quad \text{and}$$
$$I_{\mathrm{obs}} = \int I_{\nu,\mathrm{obs}} d\nu_{\mathrm{obs}} = \int I_{\nu,\mathrm{emit}} g^3 d(g\nu_{\mathrm{emit}}) \propto g^4 I_{\mathrm{emit}} \propto g^4 \epsilon, \tag{2.11}$$

Here, I_{emit} and I_{obs} represent the emitted and observed intensities, respectively, and ϵ is the emissivity profile, which was discussed and calculated in Section 2.1.1. The

observed Fe line strength and shape can be simulated by combining the emissivity simulation with the backward ray-tracing simulation from the observer to the disk.

2.2 Monte Carlo Radiative Transfer Studies

Radiation processes are complex and computationally demanding due to their high dimensionality. The radiation field generally depends on three spatial dimensions and three momentum directions (frequency and two angles), resulting in a six-dimensional time-dependent solution that requires computational techniques to solve (Roth & Kasen, 2015), not to mention the case when polarisation also needs to be studied. To reduce dimensionality and complexity, various numerical methods have been employed, such as neglecting angular dependencies (e.g. M1 closure, Pomraning, 1969), frequency (e.g. grey opacity Eddington, 1926), temporal dependence (steady-state), or assuming spatial symmetry (e.g. spherical). Monte Carlo Radiative Transfer (MCRT) methods are among the most versatile approaches, as they enable the treatment of the problem in its full dimensionality and are well-suited for parallelization on computing clusters. The code I use for the second part of my dissertation (Chapter 5) is a MCRT code called Sedona (Kasen et al., 2006).

In the following sections, I present the radiative transfer equation, which dictates how radiation is transported, and then the Monte Carlo approach to solving it.

2.2.1 The Radiative Transfer Equation

The radiative transfer equation describes the propagation of radiation through a medium. The specific intensity, I_ν, is a fundamental parameter characterising radiation; it is defined as the amount of energy passing through a unit area per unit of time and solid angle and at a specific frequency ν. Mathematically, this can be expressed as:

$$dE = I_\nu \cos\theta \, dA \, dt \, d\nu \, d\Omega,$$

where dE is the energy passing through an infinitesimal area dA in time dt at frequency ν and solid angle $d\Omega$, and θ is the angle between the normal to the surface and the direction of the radiation. The radiative transfer equation in flat space-time is given by:

$$\frac{dI_\nu}{ds} = j_\nu - \alpha_\nu I_\nu$$

where dI_ν/ds is the rate of change of specific intensity with distance s.

The first term, j_ν, represents the amount of radiation added to the light beam as it travels through the medium due to various emission processes. The emission coefficient, j_ν, describes the efficiency of the medium in emitting radiation at a given frequency and direction. It depends on properties such as temperature, density, and composition of the medium. Key processes contributing to j_ν include bound-bound,

free-bound, free-free processes, and scattering into the line of sight. If we only have emission, the intensity of a beam increases by the integration of j_ν along the line of sight: $I_\nu(s) = I_\nu(s_0) + \int_{s_0}^{s} j_\nu(s')ds'$.

The second term, $-\alpha_\nu I_\nu$, describes how radiation is removed from the light beam due to the absorption coefficient α_ν. The absorption coefficient includes contributions from bound-bound, bound-free, and free-free processes, as well as scattering out of the line of sight. The absorption coefficient is proportional to the radiation intensity, meaning it removes a portion of the radiation as it passes through the medium. If we only have absorption, the intensity of a beam decreases exponentially by the integration of α_ν along the line of sight: $I_\nu(s) = I_\nu(s_0)e^{\int_{s_0}^{s} -\alpha_\nu(s')ds'}$.

In general, the radiative transfer equation can only be solved numerically and under certain constraints, usually under the assumption of a plane-parallel atmosphere or spherical symmetry to reduce the computational power needed (Rybicki & Lightman, 1979).

Opacity, Optical Depth and Random Walk

The absorption coefficient can be expressed as $\alpha_\nu = \kappa_\nu \rho$, where κ_ν is the opacity of a medium, a measure of its ability to absorb radiation per unit density. The opacity considers the state of the gas or material to determine the absorption rate as the radiation passes through. Comparing opacities instead of absorption coefficients is useful when comparing regions with different densities, as it quantifies the efficiency of a material to absorb radiation per unit mass.

The optical depth, $\tau_\nu(s)$, is another important parameter, defined as the integral of the absorption coefficient α_ν with respect to distance s along the path of radiation:

$$\tau_\nu(s) = \int_{s_0}^{s} \alpha_\nu ds = \int_{s_0}^{s} \kappa_\nu \rho ds'.$$

The solution to the radiative transfer equation for pure absorption then becomes $I_\nu(\tau_\nu) = I_\nu(0)e^{-\tau_\nu(s)}$. The probability for photons to travel at least one optical depth through an absorbing medium is $e^{-\tau_\nu}$, so the optical depth is directly related to the probability of being absorbed. The mean optical depth a photon can travel before absorption is exactly one optical depth, $< \tau_\nu >= \int_0^\infty \tau_\nu e^{-\tau_\nu} d\tau_\nu = 1$, which can be inverted to a mean-free path that the photon can travel before being absorbed or scattered, $l_\nu = 1/\alpha_\nu$.

The radiative transfer equation can be written and solved more easily using the definition of optical depth as

$$\frac{dI_\nu}{d\tau_\nu} = S_\nu - I_\nu,$$

where $S_\nu = j_\nu/\alpha_\nu$. The formal solution to this equation is $I_\nu(\tau_\nu) = S_\nu + e^{-\tau_\nu}(I_\nu(0) - S_\nu)$. In optically thin media, where $\tau_\nu << 1$, a photon is not likely to interact with the medium, and the solution becomes $I_\nu(\tau_\nu) = I_\nu(0)$. In optically thick regions, where $\tau_\nu >> 1$, photons undergo many absorptions and scatterings before leaving

the medium, following random walks as they interact with the medium. To leave the boundary in an optically thick medium with τ_0, a photon needs to scatter or be absorbed $N = \tau_0^2$ times. This causes the radiation to exhibit diffusion-like behaviour, where the specific intensity becomes isotropic and approaches a constant value, which for LTE is the Planck function B_ν, i.e., $I_\nu = S_\nu = B_\nu$.

2.2.2 Monte Carlo Method in Solving the Radiative Transfer Equation

The Monte Carlo method simulates random interactions between photon packages and matter as the former propagates through a medium. This approach retains the complete angular dependence of the radiation field and naturally models complex physical interactions by directly sampling the appropriate probability distributions. In MCRT, photon packages are often treated as indivisible energy packages, ensuring energy conservation before and after an interaction (Lucy, 2002; Kasen et al., 2006). This treatment prevents the exponential growth of photons when treating bound-bound fluorescence, which would have otherwise made the simulations computationally impossible.

Photon interactions in MCRT are determined by a series of random numbers generated at each step, which dictate the directions and distances that photons travel, and the type of interactions they undergo with the matter. The likelihood of interaction is described by a probability distribution based on the medium's physical properties, such as density, ionisation and excitation state, composition, and temperature. The Monte Carlo method calculates the probabilities of all the possible interactions based on the energy flow and uses random numbers to determine the specific transition.

Photon Propagation

As previously discussed, optical depth is directly related to the probability of absorption and scattering through $p(\tau_\nu) \propto e^{-\tau_\nu}$. Therefore, optical depth is an important parameter in modelling radiative processes. To mimic the average travel distance/optical depth before an interaction occurs, a random benchmark optical depth $\tau_0 = -\ln(1-\zeta)$ is generated, where ζ is a random number between $[0,1]$ (Noebauer & Sim, 2019). An interaction occurs during the move ds if $\tau_\nu = \int \kappa_\nu \rho ds > \tau_0$; otherwise, a new τ_0 is generated and the photon packet is propagated ds until an interaction occurs or the package has left the computational domain. Some MCRT codes propagate the photon a distance l' based on τ_0, such that $\tau_0 = \int_0^{l'} \kappa_\nu ds = \tau_\nu$, and move the photon packet to the point where the interaction occurs.

The type of interaction is determined according to the weights of the opacity, e.g., scattering occurs if $\kappa_s/\kappa_t < \zeta_1$, where κ_s is the scattering opacity, κ_t is the total opacity, and ζ_1 is a new random number between $[0,1]$. MCRT codes determine the total frequency-dependent opacity similarly to classical methods by adding individual opacity sources. After an event, the photon packet is given a new random direction and frequency depending on the type of interaction. Typically, codes adopt isotropic

scattering/emission in the rest frame, so the two angles, α and β, are randomly drawn as $\cos(\alpha) \in [0, 1]$ and $\beta \in [-1, 1] \times \pi$.

Detailed radiative transfer physics can be modelled intuitively by simulating photons through this random approach, with scattering and full dimensionality more easily implemented compared to numerical solutions of the radiative transfer equation (Noebauer & Sim, 2019).

Sedona

In Chapter 5, the MCRT code Sedona is used to calculate the emergent spectra from super-Eddington accretion geometry. Sedona is a MCRT transport code that has been applied to various astrophysical phenomena such as supernovae (Kasen et al., 2006), kilonovae (Kasen et al., 2015), and TDEs (Roth et al., 2016; Dai et al., 2018). It solves the frequency-dependent, time-dependent radiation transport in most geometries.

In this code, gas is assumed to be in either local thermodynamic equilibrium (LTE) or non-LTE for calculating the atomic ionisation and excitation state. The gas temperature structure is updated based on the radiative heating and cooling rates after each time step (or iteration if steady-state). The non-LTE rate equations are solved in statistical equilibrium, allowing for arbitrary velocity structures and radiation fields. Given the ionisation and excitation states, the opacity and emissivity of the gas are determined using advanced astrophysical radiative processes and atomic structure databases containing millions of line transitions, which set the cooling/heating rates. Such calculations are repeated for many iterations until the equilibrium in temperature and other parameters is achieved.

Chapter 3

X-ray Flouresence

The content of this chapter is drawn from the paper: "X-Ray Fluorescence from Super-Eddington Accreting Black Holes" by Thomsen L. L., Lixin Dai J., Ramirez-Ruiz E., Kara E., Reynolds C, 2019, The Astrophysical Journal Letter, ApJL, 884, L21. doi:10.3847/2041-8213/ab4518 with minor consistency and grammar modifications. As the paper's first author, I calculated the Fe Kα line spectra with a general relativistic ray-tracing code, analysed and interpreted the results, and contributed significantly to writing the paper.

X-ray reverberation has proven to be a powerful tool capable of probing the innermost region of accretion disks around compact objects. Current theoretical effort assumes that the disk is geometrically thin, optically thick, orbiting with Keplerian speed. Thus, these models cannot be applied to super-Eddington accretion systems because the thin disk approximation fails in this accretion regime. Furthermore, state-of-the-art numerical simulations show that optically thick winds are launched from the super-Eddington accretion disks, changing the reflection geometry significantly from the thin disk picture. We conduct theoretical investigations on this topic by focusing on the Fe Kα fluorescent lines produced from super-Eddington disks and show that the funnel geometry and wind acceleration shape their line profiles. We also systematically compare the Fe line profiles from super-Eddington thick disks to those from thin disks and find that the former is substantially more blueshifted and symmetric in shape. These results are consistent with the observed Fe Kα line from the jetted tidal disruption event, Swift J1644, in which a transient super-Eddington accretion disk was formed from stellar debris. Therefore, careful analysis of the Fe Kα line profile can be used to identify systems undergoing super-Eddington accretion.

3.1 Introduction

Some of the most luminous astrophysical sources, such as the active galactic nuclei (AGNs), X-ray binaries (XRBs) and long gamma-ray bursts (GRBs), are all powered by the accretion of gas onto black holes (BHs). Viscous or magnetic process in the gaseous disk transports angular momentum outwards and heats up the disk (Shakura & Sunyaev, 1973; Balbus & Hawley, 1991). In this process, part of the gas mass-energy is effectively converted into energy and released as radiation or large-scale outflows in the wind and jet regions. Therefore, it is of uttermost importance to study the detailed structure of accretion disks. While a Keplerian rotating thin disk with no outflows (Shakura & Sunyaev, 1973; Novikov & Thorne, 1973) is widely applied to explain many accreting systems, this disk model will break down when the accretion rate is very low or very high. For the latter case, it is because there exists a theoretical upper threshold of radiation level, which corresponds to the equilibrium when the radiation pressure force on a gas element balances the gravitational force it receives from the BH. This maximum luminosity, called the Eddington luminosity, $L_{\rm Edd}$, and the corresponding Eddington accretion rate, $\dot{M}_{\rm Edd}$, are given by the following equations

$$L_{\rm Edd} \approx 1.26 \times 10^{38} \left(\frac{M}{M_\odot} \right) \ {\rm erg\ s^{-1}} \quad \text{and} \quad \dot{M}_{\rm Edd} = \frac{L_{\rm Edd}}{\eta\, c^2}, \tag{3.1}$$

where $M/M_\odot$ is the mass of the central object in units of solar masses $M_\odot$, c is the speed of light, and η is called the radiative efficiency. When the accretion level exceeds this limit, the radiation pressure will become large enough to change the disk structure, making it geometrically and optically thick (Begelman, 1978; Abramowicz et al., 1980). Recently, great progress has also been achieved through numerical studies with the aid of general-relativistic radiation magnetohydrodynamic (GRRMHD) codes (Ohsuga et al., 2009; Jiang et al., 2014; McKinney et al., 2014; Sądowski et al., 2014; Dai et al., 2018). These simulations of super-Eddington accretion flows have shown that the Eddington luminosity limit can be broken, and large-scale optically-thick winds are launched from the disk. These findings have significant implications on how much of the supplied gas can eventually be accreted onto the BH, how much energy is carried away by outflows and how much radiation can escape. Fast winds, consistent with simulation results, have also been observed from ultra-luminous X-ray sources (ULXs) (e.g., Pinto et al., 2016) and tidal disruption events (e.g., Kara et al., 2016b, 2018; Alexander et al., 2017), both likely undergoing super-Eddington accretion.

Tremendous effort has been put into constraining the structures of accretion disks from observational features. In particular, X-ray reverberation, first proposed by Fabian et al. (1989), has proved to be very useful in directly measuring the inner disk geometry by combining the spectral and temporal information from this region. As presented in the review by Reynolds (2014), the classical approach to X-ray reverberation is to place a hot and compact corona above the cold accretion disk from where it emits non-thermally distributed X-rays. The disk is illuminated by the coronal emission, which

gives rise to an X-ray reflection spectrum. One notable feature of the reflection spectrum is the Fe Kα fluorescent lines that are produced from the irradiated and ionised disk (Matt et al., 1993). General relativistic (GR) and Doppler effects between the rotating disk and the observer jointly make the fluorescent line profiles broadened and skewed. This theoretical model has been successfully applied to constrain the spin of BHs in systems where the disk has a razor-thin structure and is rotating with relativistic Keplerian speed (e.g., Fabian et al., 1989; Reynolds & Begelman, 1997; Reynolds et al., 1999; Reynolds, 2014). The line profile depends on the BH spin because the innermost edge of a thin disk is given by the BH's innermost stable circular orbit (ISCO), which is smaller for a BH with a larger prograde spin. X-ray reverberation has also been used to study the nature of the coronal formation, for which a full understanding has not yet been achieved (Blandford et al., 2017; Yuan et al., 2019). Therefore, various coronal geometries have been investigated. The simplest and best-studied geometry is the "lamppost" model, where the corona is assumed to be an isotropically-radiating point source located at a few R_g above the BH (Matt et al., 1991; Reynolds & Begelman, 1997; Reis & Miller, 2013). Other coronal geometries that have been explored include an off-axis compact corona or an extended coronal source (see Wilkins & Fabian, 2012). Coronae with geometry changing on short timescales, likely associated with changes in the accretion states, have also been reported recently (Kara et al., 2019).

While most of the effort described above assumes a thin Keplerian disk structure, recently, some efforts have also been made to incorporate finite disk thickness from analytical disk models (Wu & Wang, 2007; Taylor & Reynolds, 2018a) or realistic structures from thin disk simulations (e.g., Schnittman et al., 2013). However, theoretical investigations on this topic have not been extended to accretion flow with optically-thick winds, which can be formed when a disk undergoes super-Eddington accretion. We expect the X-ray reverberation signatures from super-Eddington disks to be very different from those from thin disks because the coronal emission will no longer be reprocessed by the surface of the (thin) disk but by the optically thick winds. Also, we expect the trajectories of the reflected photons and their redshifts to be radically different due to the different geometry and motion of the optically thick winds compared to the usually assumed equatorial Keplerian flow. One of the main reasons for the lack of literature on this topic is that simulations did not resolve the detailed structure of super-Eddington accretion flow until about a decade ago. Another main reason is that observational evidence of X-ray reverberation from a definitively super-Eddington accretion flow has only been reported recently in Kara et al. (2016b), where they observed the energy-lag spectrum and a strongly blueshifted Fe line from the jetted TDE, Swift J1644. In order to successfully explain the salient observational features, the authors also conducted preliminary theoretical modelling by assuming the Fe lines were reflected by a conical funnel moving at a speed of few$\times 0.1\ c$, which corresponds to the speed of winds launched from a super-Eddington accretion disk formed by stellar debris.

As a first step towards better understanding X-ray reverberation from super-Eddington

accretion flows and motivated by the framework described in Kara et al. (2016b), we study the fluorescent Fe Kα emission line profiles derived from state-of-the-art super-Eddington disk simulations. We study in detail the profile of a super-Eddington disk, previously simulated in Dai et al. (2018), and calculate the reflection surface of the coronal emission, which is embedded in the optically thick winds, and its properties (Section 3.2). Since the wind region has a much lower density than dense thin disks, the ionisation level of the reflection surface is naturally higher, so hotter fluorescent Fe Kα lines with higher rest-frame energies are expected to be produced. Next, we apply GR ray-tracing techniques to trace the coronal photons from being reflected by this surface to reaching a faraway observer. We calculate the theoretical Fe Kα line profile and check its dependence on various parameters such as the observer inclination angle and coronal location (Section 3.3). Furthermore, we make a systematic comparison between the Fe Kα line profiles produced from the simulated super-Eddington accretion disk and those produced from standard thin disks (Section 3.4). We show that a typical Fe Kα line from super-Eddington disks exhibits a large blueshift while, depending on the observer's inclination angle, the thin disk counterparts are either dominated by redshift or show a much lower blueshift. Also, the Fe line from a super-Eddington disk has a more symmetric shape with respect to the line centre. Therefore, these morphological differences of the Fe Kα line can effectively indicate super-Eddington accretion rates. Lastly, we briefly compare the theoretical predictions to the observation of the Fe Kα line from the jetted TDE, Swift J1644, and discuss the implications and future directions of this work (Section 3.5).

3.2 Disk Profile, Funnel Geometry and Ionisation Level

First, let us briefly summarise the basic properties of super-Eddington accretion disks relevant to X-ray reverberation. In order to do this, we set the super-Eddington disk, simulated in Dai et al. (2018), in a classical X-ray reflection picture. Fig. 3.1 illustrates the corona, disk, wind and funnel structures. The disk surrounds a supermassive BH with a mass of $5 \times 10^6\ M_\odot$ and a fast dimensionless spin parameter of 0.8. We calculate the time and azimuthal-averaged profile of the disk after the inflow equilibrium has been established to $r \approx 100\ R_g$ ($R_g = GM_{\rm BH}/c^2$ is the gravitational radius of the BH, with G being the gravitational constant and $M_{\rm BH}$ being the BH mass). During this phase, the averaged accretion rate onto the BH is about 15 $\dot{M}_{\rm Edd}$. Consistent with theoretical predictions, the inner disk extends within the ISCO since the thick disk is supported by radiation pressure. A relativistic jet is launched magnetically due to the large-scale magnetic flux threading the inner disk region. Winds, which are denser and slower towards the equator, are also launched from the thick accretion disk, thus creating an optically thin "funnel" near the pole. Here we adopt the standard lamppost model and place a hard X-ray emitting and compact corona at the height of $h_{\rm LP} =$ few $\times\ R_g$ above the BH. (Note that the corona is placed artificially since the GR-RMHD disk simulation in Dai et al. (2018) and other global accretion disk simulations

cannot self-consistently produce compact coronae.) The corona's emission is reflected by and irradiates the wall of the funnel. We have also cut out the jet region (where the gas pressure over the magnetic pressure $\beta \approx 1$) since the gas density in the jet can be numerically boosted due to the large magnetic pressure near the jet base.

We take a simplified treatment in calculating the coronal reflection surface by assuming that the coronal photons are reflected by a photosphere of a single electron-scattering optical depth as seen by the corona. The optical depth is calculated by:

$$\tau_{\rm es} = \int \kappa_{\rm es}\, \rho {\rm d}l = \int 0.2(1+\chi)\rho \frac{{\rm cm}^2}{\rm g} dl = \int 0.34 \rho \frac{{\rm cm}^2}{\rm g} {\rm d}l, \tag{3.2}$$

where $\kappa_{\rm es}$ is the Thomson electron-scattering opacity, ρ is the density, and $\chi = 0.7$ corresponds to the hydrogen mass fraction with solar abundances. Here, only Newtonian calculations are used for the optical depth without considering the GR light-bending effect. Since the Fe lines are produced within the first few optical depths (Matt et al., 1993), we have calculated the $\tau = 1$ and $\tau = 3$ photospheres and showed them in Fig. 3.1. The two reflection surfaces lie close to each other since the density of the wind increases steeply away from the pole. Either surface resides mostly in the optically-thick winds with large outflow velocities ($v_r > 0.1c$). Also, the reflection surface has a narrow half-opening angle between $10 - 15^\circ$. Therefore, the optically thick disk and wind will obscure the coronal emission when viewed from the side, and the corona and its reflection emission can only be seen by an observer looking directly down the funnel.

Next, we investigate the motion of the reflection surface. As shown in Fig. 3.2a, close to the BH, the photosphere is embedded within a disk inflow region, but beyond $\rho \approx 6\ R_g$ (ρ is the cylindrical distance) it is embedded within the outflows. Along the photosphere, the 3-velocity in the radial coordinate direction from the black hole, v_r, increases and then saturates towards a terminal speed of $v_r \approx 0.4 - 0.5$c. The photosphere rotates at sub-Keplerian velocity, and the radial velocity dominates over the rotational velocity after $\rho \approx 10\ R_g$. Therefore, one will expect that the X-ray reflection spectrum is dominated by the radial motion of the winds instead of the Keplerian motion of the disk, as in the case of a standard thin disk. The radial velocity of the photosphere of $\tau = 3$ has been fitted (within 5% deviation in the wind region) with the following equation:

$$\frac{v_r}{c} = 0.5 - \frac{6.2 R_g}{6R_g + \rho}. \tag{3.3}$$

Last, we investigate a crucial parameter – the ionisation level. The ionisation parameter, ξ, depends on the density of the reflection surface and the hard X-ray irradiation flux of the corona, and it is calculated as (Reynolds & Begelman, 1997):

$$\xi(r) = \frac{4\pi F_x}{n(r)}, \tag{3.4}$$

where $n(r)$ is the gas number density of the reflection surface, and F_x is the coronal flux

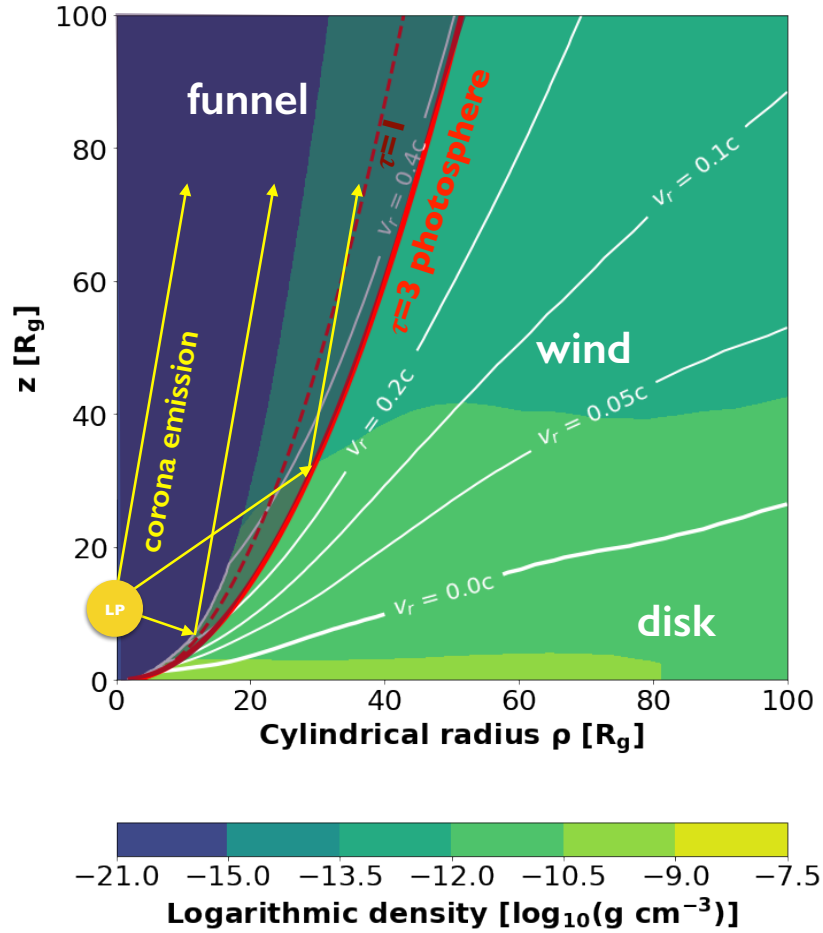

Figure 3.1: The geometry of the disk, winds, corona and its reflection surface for the simulated super-Eddington disk structure. The density of the disk and winds are shown by the background colour in $\log_{10}$ of cgs units [g cm^{-3}]. Here, the x-axis and y-axis are the cylindrical radius ρ and the vertical height z, both in units of the gravitational radius R_g. We have illustrated the jet (with $\beta < 1$) as the dark blue region around the pole. The white lines are contours of constant radial velocity in the wind region, which shows that the winds move faster at small inclination angles. An optically-thin funnel (the shaded region) exists around the pole, which is surrounded by optically-thick winds. The yellow circle represents the (artificially placed and size-exaggerated) lamppost corona located at 10 R_g above the BH. The thick red line and thin dashed red line are, respectively, the electron-scattering photospheres with a Thompson optical depth of $\tau = 3$ and $\tau = 1$ integrated from the corona, and they represent the reflection surface for coronal emission. An observer looking down the funnel can see the direct emission from the corona and the coronal emission reflected by the funnel (including the Fe Kα fluorescent lines).

crossing the reflection surface. Using the Newtonian irradiation profile, the coronal irradiation flux can be expressed analytically as:

$$F_x = \frac{L_x \cos(\psi)}{4\pi R_{\rm LP}^2}, \tag{3.5}$$

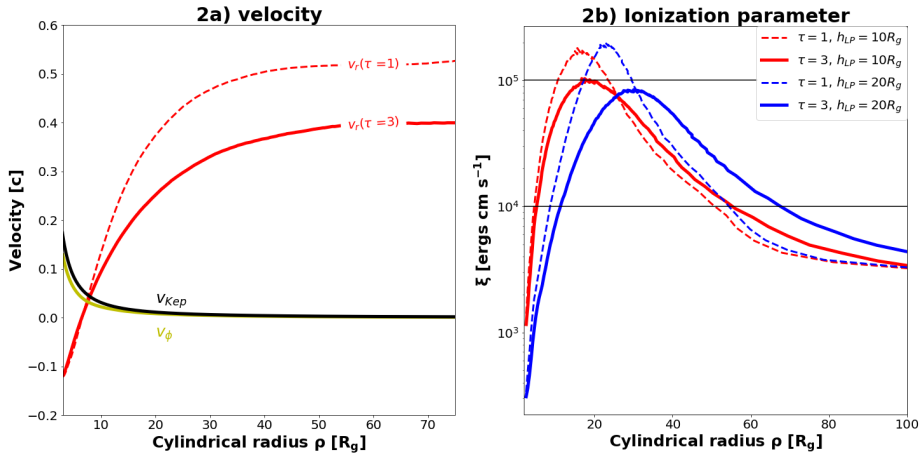

Figure 3.2: Properties along the reflection surfaces. 2a. The radial and rotational velocity of the reflection surface. The velocities plotted here are the equivalent Newtonian three-velocity converted from the GR four-velocity of the gas in the simulated accretion flow. The red curve is the radial velocity of the photosphere with $\tau = 3$, and the thin dashed curve is that for the $\tau = 1$ photosphere. The rotational velocities of the two photospheres lay almost on top of each other (yellow curve). As a comparison, we also plot the Keplerian rotational velocity (black curve) and show that the thick disk/wind rotation is sub-Keplerian. v_θ is relatively unimportant and is therefore not illustrated. Along the reflection surface, it can be seen that the wind starts to accelerate, and eventually, it saturates at a terminal velocity of $v_r \approx 0.3$-0.5 c. The outward radial motion of the wind dominates over the rotation beyond $\rho \approx 10\ R_g$. Therefore, the Fe reflection spectrum is primarily determined by the radial motion of the winds instead of the Keplerian motion of the (thin) disk. **2b. The ionisation level of the reflection surface.** We show the ionisation parameter, ξ, in cgs units [ergs cm s^{-1}] along the photosphere as a function of the cylindrical distance ρ. The ionisation level is not very sensitive to the choice of coronal height or optical depth of the photosphere. With the assumption that the hard X-ray coronal luminosity scales similarly with the accretion rate as in standard thin disks, then for our system, we have $L_x = 1\%\ \dot{M}c^2 \approx 0.1\ L_{\rm Edd}$, and thus the ionisation level is much higher compared to the thin disk case ($\xi \lesssim 1000$ erg cm s^{-1}). Therefore, the production of hot Fe lines is favoured. The two horizontal black lines mark the range of the ionisation parameter where the hot Fe Kα fluorescent line with rest-frame energy of 6.97 keV is likely produced.

where L_x is the luminosity of the hard X-ray coronal photons, $R_{\rm LP}$ is the distance from the lamppost corona to the gas element on the reflection surface, and ψ is the angle the vector from the corona to the reflection surface produces with the normal vector of the reflection surface.

The ionisation level will determine whether Fe Kα fluorescent lines can be produced, and if so, whether a higher or lower ionisation line (e.g., 6.4, 6.7 or 6.97 keV) is emitted (Ross et al., 1999; Ballantyne & Ramirez-Ruiz, 2001). Since there is still not a good understanding of how the corona power should scale with the accretion rate in super-Eddington accretion, we assume that the coronal luminosity scales with the accretion rate as $L_x = \eta_x \times \dot{M}c^2$, and we adopt $\eta_x = 0.01$ as conventionally used for thin

disk coronal models (Reynolds et al., 1999). Under this assumption, the coronal luminosity is $L_x \approx 0.1\, L_{\rm Edd}$ for our simulated disk with an accretion rate of about $15 \times \dot{M}_{\rm Edd}$. As illustrated in Fig. 3.2b, the ionisation level is several orders of magnitudes higher than that of the theoretical thin disk (usually with $\xi \lesssim 100$ erg cm s^{-1} outside the ISCO, see e.g., Reynolds & Begelman, 1997). This is mainly because the density of the gas in the wind is much more dilute than a dense thin accretion disk. Fig. 3.2b also shows that the ionisation level primarily lies between 10^4 and 10^5 ergs cm s^{-1}, independent of the assumptions for the τ-value of the reflection surface or the lamppost height. This high ionisation interval strongly favours the production of the hot and warm Fe Kα lines with rest-frame energies of 6.97 and 6.7 keV instead of the cold 6.4 keV Fe line, usually assumed to be produced from thin disks (Ballantyne & Ramirez-Ruiz, 2001).

3.3 Line Profile

In this section, we study how an initial Fe Kα line emitted at a single energy in the co-moving frame of the emitting gas appears skewed and broadened due to the relative motion and different gravitational potentials between the emitting gas and the observer. This is calculated using general-relativistic ray-tracing. In Section 3.3.1, we give a brief summary of the GR ray-tracing theory and introduce our methodology. In Section 3.3.2, we present the calculated Fe Kα emission line profiles and show how it depends on physical parameters such as the viewing angle, the choice of the optical depth for the reflection surface and the height of the corona.

3.3.1 Methodology for GR Ray-Tracing

When photons are emitted by gas in one frame and observed in another frame, the intensity shift of the photons between the two frames can be calculated using the Louivilles Theorem, which states that the photon phase-space density, I_ν/ν^3, is conserved along the ray (Cunningham, 1975). Here, I_ν is the specific intensity at frequency ν. We denote $I^{\rm obs}_{\nu_o}$ to be the observed specific intensity at the observed frequency ν_o and $I^{\rm emit}_{\nu_e}$ to be the emitted specific intensity at the emitted frequency ν_e. Thus we have:

$$I^{\rm obs}_{\nu_o} = I^{\rm emit}_{\nu_e}(\nu_o/\nu_{\rm e})^3 = g^3 I^{\rm emit}_{\nu_e}. \tag{3.6}$$

Here, g is the energy shift (or the redshift) from the emitted photon to the observed photon, and it is defined by:

$$g \equiv \frac{\nu_o}{\nu_e} = \frac{E_{\rm obs}}{E_{\rm emit}}, \tag{3.7}$$

where E is the energy of the photon. Therefore, we can calculate the total intensity, integrated over all frequencies, by:

$$I^{\rm obs} = \int I^{\rm obs}_{\nu_o}\, d\nu_o \propto \int I^{\rm emit}_{\nu_e} g^3\, d\nu_o = \int I^{emit}_{\nu_e} g^3\, d(g\,\nu_e) \propto g^4\, I^{\rm emit}. \tag{3.8}$$

For faraway sources, we note that the observed flux and intensity are proportional. The reason for this is that the specific flux at the observed frequency, ($F^{\rm obs}_{\nu_0}$) is the observed specific intensity ($I^{\rm obs}_{\nu_0}$) integrated across the solid angle of the emitting surface as seen by the observer. Therefore, we have:

$$F^{\rm obs}_{\nu_o} = \int_{\rm source} I^{\rm obs}_{\nu_o} \cos(\theta_i)\, d\Omega \approx I^{\rm obs}_{\nu_o} \Omega \propto I^{\rm obs}_{\nu_o}. \tag{3.9}$$

Here Ω is the solid angle of the reflection surface as seen by the faraway observer, and θ_i is the angle between the direction of the BH and incoming rays from the reflection surface. Since the observer is assumed to be far away, then $\cos(\theta_i) \approx 1$. Therefore, the total flux goes like $F \propto g^4$ as well.

We employ a GR ray-tracing code (Dai, 2012, based on equations from Fuerst & Wu 2004) to calculate the photon trajectory from the emitting gas to a faraway stationary observer. The code uses the Boyer-Lindquist spherical coordinate system to describe the space-time around a Kerr black hole with the line element (in geometric units $G = M = c = 1$):

$$ds^2 = -\left(1 - \frac{2r}{\Sigma}\right) dt^2 - \frac{4ar\sin^2\theta}{\Sigma}\, dt\, d\phi + \frac{\Sigma}{\Delta}\, dr^2 + \Sigma\, d\theta^2 + \left(r^2 + a^2 + \frac{2a^2 r \sin^2\theta}{\Sigma}\right) \sin^2\theta\, d\phi^2, \tag{3.10}$$

where (t, r, θ, ϕ) is the Boyer-Lindquist spherical coordinates and $\Delta = r^2 - 2\,r + a^2$ and $\Sigma = r^2 + a^2\,\cos^2\theta$. In this code, we calculate the geodesic of particles by evolving the six variables $t, r, \theta, \phi, p_r, p_\theta$ using the following equations:

$$\begin{aligned}
&p_t = -E \quad \dot{t} = E + \frac{2r(r^2+a^2)E - 2aL}{\Sigma\Delta} \\
&p_r = \frac{\Sigma}{\Delta}\dot{r} \quad \dot{p}_r = \frac{(r-1)\left((r^2+a^2)H - \kappa\right) + rH\Delta + 2r(r^2+a^2)E^2 - 2aEL}{\Sigma\Delta} - \frac{2p_r^2(r-1)}{\Sigma} \\
&p_\theta = \Sigma\dot{\theta} \quad \dot{p}_\theta = \frac{\sin\theta\cos\theta}{\Sigma}\left(\frac{L^2}{\sin^4\theta} - a^2(E^2+H)\right) \\
&p_\phi = L \quad \dot{\phi} = \frac{2arE + (\Sigma - 2r)L/\sin^2\theta}{\Sigma\Delta}
\end{aligned} \tag{3.11}$$

Here, p_t and p_ϕ are constants of motion representing the conservation of energy, E, and angular momentum around the spin axis, L. Furthermore, we have two additional constants: H is the Hamiltonian (which is 0 for photons and -1 for massive test particles) and $\kappa = Q + L^2 + a^2(E^2 + H)$, where Q is Carter's constant given by $Q = p_\theta^2 - a^2 E\cos^2\theta + L^2\cot^2\theta$.

Evolving these six variables along a ray enables one to calculate the photon energy shift, g, from the frame of the emitting gas to the faraway observer as:

$$g = \frac{E_{\rm obs}}{E_{\rm emit}} = \frac{(p_\mu u^\mu)_{\rm obs}}{(p_\mu u^\mu)_{\rm emit}} = \frac{-E}{(p_\mu u^\mu)_{\rm emit}}. \tag{3.12}$$

The four-velocity for a faraway stationary observer only has a time component of $u^t = \left(1 - 2r/\Sigma\right)^{-1} \approx 1$, and $u^\mu_{\rm emit}$ is the four-velocity of the emitting gas along the reflection surface. For a thin disk, the reflection surface lies in the equatorial plane and orbits with the GR Keplerian four-velocity (Bardeen et al., 1972):

$$\tilde{u}_{\rm disk} = u^t(1, 0, 0, \Omega), \quad \text{where } \Omega = (a + \rho^{3/2})^{-1}, \quad \text{and } u^t = \frac{a + \rho^{3/2}}{\sqrt{\rho^3 - 3\rho^2 + 2a\rho^{3/2}}}. \tag{3.13}$$

When calculating the Fe line profile from the super-Eddington disk, the four-velocity of the emitting gas element along the chosen photosphere is directly obtained from the GRRMHD simulation. Since the irradiation parameter drops very fast with distance from the BH, we only include emission from the disk region extending from the ISCO to 100 R_g when calculating the thin disk profile. We have a maximum cylindrical radius of $\rho = 100\ R_g$ for super-Eddington disks.

We also assume that the emitted fluorescent line intensity scales with the coronal irradiation flux crossing the reflection surface (see Eq. 3.5). Therefore, the observed Fe Kα line intensity can be calculated using the following equation:

$$I^{\rm obs} = I^{\rm emit}\, g^4 \propto g^4\, \frac{\cos(\psi)}{R^2_{\rm LP}}. \tag{3.14}$$

In the ray-tracing code, we use the standard fifth-order Runge-Kutta integrator to evolve these equations with adaptive step sizes, so the curved photon trajectories close to the BH can be accurately traced. We also adopt the standard procedure to start from an image plane, placed at $r = 1000\ R_g$, and trace the photons backwards in time to the accretion disk to save computing power.

3.3.2 Fe Kα Reflection Spectrum from Super-Eddington Accretion Flow

In this section, we will present the calculated X-ray fluorescent Fe Kα line profiles from the simulated super-Eddington accretion disk. These line profiles look very different from the thin disk Fe lines primarily because the coronal reflection surface has fundamentally different geometry and motion. While various simulations of super-Eddington accretion disks have shown that the details of the wind profile can depend on the BH mass, spin, or the accretion rates (McKinney et al., 2015; Sądowski & Narayan, 2016; Jiang et al., 2019), these simulations have also shown that the basic structure of the accretion inflow and outflow stays the same and the wind speeds in the funnel region are consistent to the first order. Therefore, the basic coronal irradiation picture, as illustrated in Fig.3.1, should generically apply to super-Eddington systems. In this work, we only calculate the Fe reflection spectrum from one simulated super-Eddington disk structure (Dai et al., 2018) to highlight its morphological differences from the standard Fe line spectra produced by thin disks since the exploration of how the exact funnel geometry or wind speed depends on various physical parameters goes beyond the scope of this short letter.

Our fiducial configuration for the Fe line profile of the super-Eddington accretor is obtained using the following parameters: $\tau = 3$ (following Matt et al., 1993), $h_{\rm LP} = 10\ R_g$ and $i = 5^\circ$ (from the pole), and it is plotted in all panels of Fig. 3.3 using thick red lines. We plot this line profile together with a few representative Fe line profiles of thin disks in Fig. 3.3a. Consistent with previous studies (Reynolds & Begelman, 1997; Dabrowski et al., 1997; Reynolds et al., 1999), the thin disk Fe line profile has a strong viewing-angle dependence, and it is always skewed bluewards due to an extended red wing caused by gravitational redshift. Only when a thin disk is viewed almost edge-on can one observe a significant blueshifted component (with $g = E_{\rm obs}/E_{\rm emit} > 1$) due to the Doppler motion of the disk. However, for the face-on super-Eddington disk case, one can see that the Fe line is very strongly blueshifted due to the reflecting gas elements in the fast winds, which are moving towards the observer looking down the funnel. We will discuss more details of these differences in Section 3.4.

In the following part of this section, we will check whether the Fe line profiles, produced by the super-Eddington disk, stay robust against changes in the choice of the optical depth of the reflection surface, τ, and the height of the lamppost corona, $h_{\rm LP}$, and whether they sensitively depend on the inclination angle of the observer, i.

First, we investigate the dependence on the choice of the photosphere. As shown in Fig. 3.3b, the Fe line spectra produced from different τ-surfaces have similar line shapes, while the peak of the Fe line profile is more blueshifted in the case of smaller τ values. The reason for this is that the photosphere with a smaller τ value lies closer to the pole (see Fig. 3.1), where the wind moves faster. Also, the Fe line profile from the photosphere with a smaller τ value has a broader width due to the more significant velocity variance of the wind speed along this photosphere. Note we have simplified the reflection geometry to be a reflection surface of a single τ value. However, photons should have gone through multiple scatterings in the optically-thick wind region at different optical depths before being reflected towards the observer. A detailed radiative transfer calculation is needed to obtain an accurate Fe line profile. However, the similarities between the line shapes across different τ-surfaces indicate that the Fe line profile obtained this way is a good approximation.

Next, we show in Fig. 3.3c that the observed Fe line profile has a very weak dependence on the inclination angle of the observer – as long the observer is looking directly into the funnel. Since the funnel is narrow (with a half-opening angle of $10 - 15^\circ$), only minor changes in the viewing angles are possible, so one would not expect to see any significant differences in the Fe line profiles. However, observing the corona and its reflected emission does depend heavily on the viewing angle, in the sense that the optically thick disk and wind will obscure the emission for observers looking at the system from other directions. The viewing-angle dependence is further weakened since the radial motion of the wind dominates over its rotation.

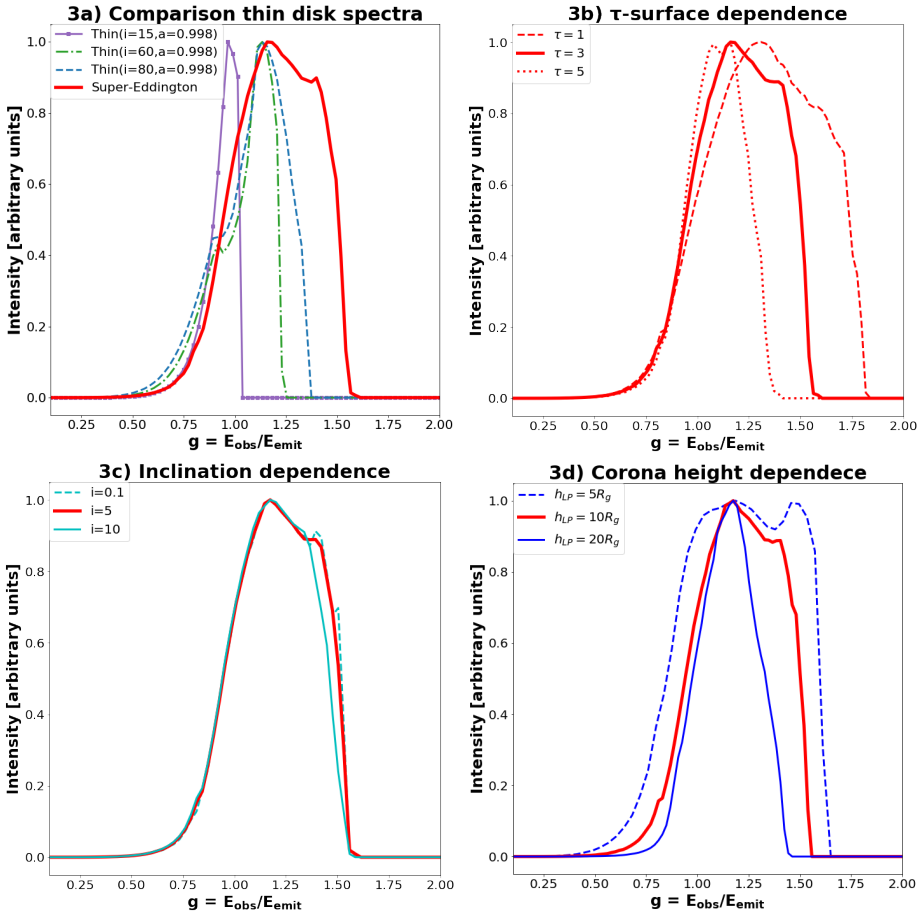

Figure 3.3: The intensity of fluorescent Fe Kα line profiles from the simulated super-Eddington disk with different τ-surfaces, inclination angles and lamppost heights, and also in comparison with thin disk line profiles. The thick red line in all panels represent the fiducial super-Eddington disk case using $\tau = 3$, $h_{\rm LP} = 10\ R_g$ and $i = 5^\circ$. All the line profiles are scaled to have the maximum at 1. **3a. Comparison between the Fe line from the super-Eddington disk and representative thin disks.** The thin disk Fe lines are plotted using thin lines. All the thin disks have the same spin parameter of $a = 0.998$. It can easily be seen that the Fe line profile of the face-on super-Eddington disk is even more blueshifted than line profiles of thin disks viewed from along the disk direction. **3b. Dependence on the choice of the τ-surface.** We fix the height of the corona at 10 R_g and the inclination at 5°, but vary the optical-depth of the reflection surface, τ. With increasing τ values, the funnel becomes wider with a lower wind terminal velocity along the funnel wall, which reduces the overall blueshift and the width of the Fe line produced. **3c. Dependence on the viewing angle from the pole.** Here, we fix $h_{\rm LP} = 10\ R_g$ and $\tau = 3$ and vary the viewing angle to the observer. Since the half-opening angle of the funnel is very narrow ($i \approx 10 - 15^\circ$), there is not much freedom in i for the observer to see the coronal emission and reflection. Therefore, the Fe line profiles are almost independent of i as long the observer looks down into the funnel. **3d. Dependence on the height of the compact corona.** We only vary $h_{\rm LP}$ and keep everything else the same as in the fiducial case. A lower coronal height gives more weight to the irradiation of the inner disk and therefore induces more gravitational redshift. It also induces more blueshift to the line profile since the funnel, as seen by the corona, becomes narrower and lies in a faster wind region. Therefore, the width of the Fe line is correlated with the height of the corona.

Last, we investigate the dependence that the height of the corona has on the line profile. Since the photosphere is calculated from the corona, its geometry, velocity and irradiation profile all depend on the location of the corona. In the thin disk case, a compact corona at $h_{\rm LP}$ = few R_g usually fits the observations (see Reis & Miller, 2013). For a super-Eddington disk, we assume that the corona is located at a similar height, and here we show the Fe line profiles using three different coronal heights of 5, 10, and 20 R_g in Fig. 3.3d. The photosphere calculated from a higher coronal height has a larger half-opening angle at large radii. Therefore, the corresponding Fe line profile is less blueshifted and narrower. It can further be seen that lowering the height of the corona to 5 R_g will greatly broaden the red wing of the line. This is because the photosphere close to the BH, where the gravitational redshift is the strongest, will receive more irradiating flux and contribute more to the line profile. This effect will become even more dramatic if the irradiation profile is calculated using general relativity with light-bending effects.

3.4 Identifying Super-Eddington Systems from their Iron Kα Line Profiles

In the previous section, we compared Fe line profiles produced from the super-Eddington disk with a few representatives produced from (razor) thin disks. In this section, we will make a further systematic comparison and show that the Fe line signatures between the two types of disks are morphologically different.

1. Rest-frame energy of the line: As we have shown in Section 3.2, the reflection surface in the case of a super-Eddington disk has a much higher ionisation level, which will more likely produce hot Fe Kα lines, such as the 6.97 keV rest-frame energy line, instead of the cold 6.4 keV line. Apart from this, the shape and the temporal signatures of the line profiles from the two types of disks are also distinguishable, and it is caused by the different geometry in the reflection surfaces together with relativistic effects. In order to demonstrate these differences, we show all the Fe line spectra as a function of the redshift, g, instead of the observed energy.

2. Photon energy and emission radius correlation: Photons emitted from various radii on the reflection surface from the two types of disks contribute very differently to the line spectra. For thin disks in Fig. 3.4a, 3.4b and 3.4c, one can see that more than half of the line flux is contributed by photons emitted from within $\rho = 25\ R_g$ of the disk since the irradiation profile drops quickly faraway from the BH. As a comparison, for the super-Eddington disk case (Fig. 3.4d), there is a considerable contribution to the line flux by photons emitted from $\rho \approx 25 - 50\ R_g$ (which corresponds to a larger radial distance from the BH compared to the $\rho \approx 25 - 50\ R_g$ region on a thin equatorial disk). This result can be attributed to two factors. First, in the super-Eddington disk case, the irradiation flux drops more slowly at intermediate to large distances from the BH because the reflection surface curves towards the pole. Second, the wind accelerates

along the reflection surface, and the photon intensity scales with the blueshift as $I \propto g^4$. Note that for a face-on thin disk, all parts of the disk only produce redshifted photons.

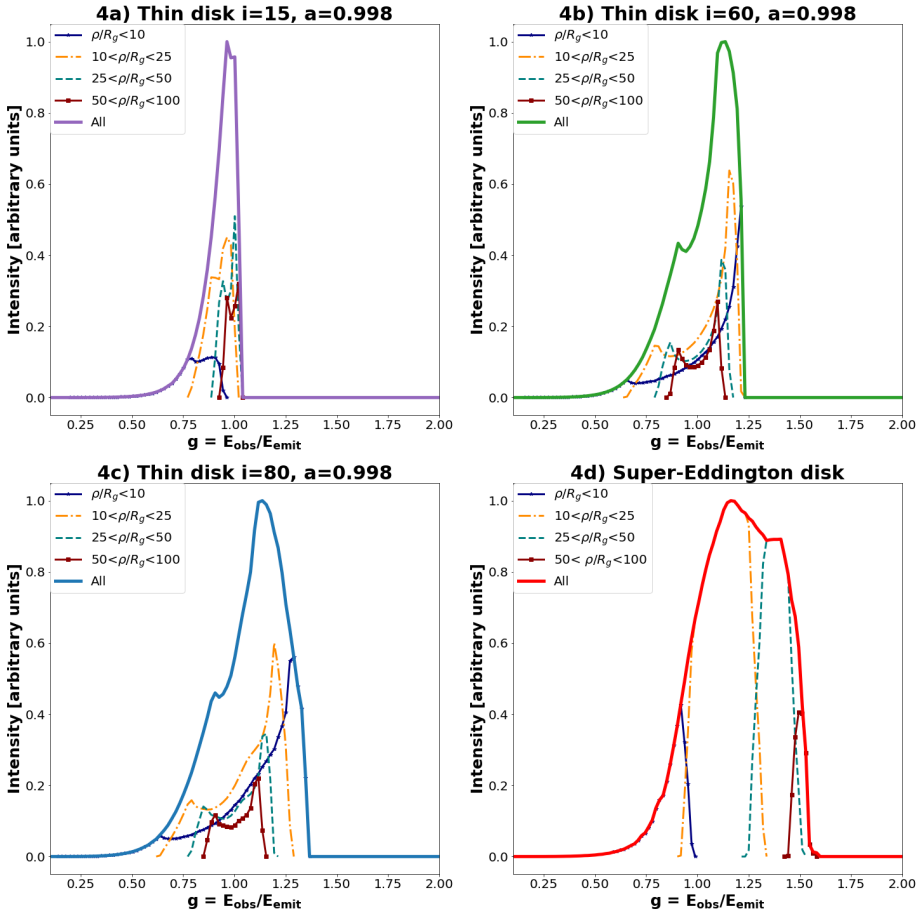

Figure 3.4: Decomposition of the Fe line energy profile based on the radii of emission. All panels show the contribution from each cylindrical radial bin (see their respective labels for the interval) towards the total line profile, which is illustrated as the thick solid lines. All line profiles are scaled to have the maximum at 1. **4a, 4b, 4c) Radial contribution towards the line profile for thin accretion disks with spin a $= 0.998$ and respective inclination angles of i $= 15^\circ$, 60° or 80°.** For all three thin disk spectra, the contribution from within $\rho < 25\ R_g$ dominates the total line flux since the irradiation flux drops very quickly with radii. Also, when compared to the line spectra from the outer disk regions, the line spectrum produced from the innermost disk region is the broadest, with both the strongest gravitational redshift and Doppler shift (when viewed from the side). **4d) Radial contribution towards the line profile for the super-Eddington accretion disk.** It can be seen that the innermost region close to the BH horizon contributes solely to the red wing of the line profile since the strong gravitational redshift dominates the innermost region as the photosphere lies in either inflow or low-velocity outflow regions. It can further be seen that the bluest part of the line profile is produced at the largest distances due to wind acceleration and large terminal velocity. Also, the contribution from $\rho > 25\ R_g$ is more significant compared to the thin disk line profiles due to the curvature of the photosphere and relativistic Doppler boosting.

Due to the Doppler effects, thin disks with moderate-to-large viewing angles (Fig. 3.4b and 3.4c) produce a double-peak line feature for each annulus of the disk. Also, the most dramatic redshifted and blueshifted parts of the line profile are both produced from the innermost part of the disk ($\rho < 10\ R_g$), where the rotation speed is the fastest, and the gravitational redshift is the strongest. However, for a face-on super-Eddington disk, the Fe line photons emitted from the inner part of the reflection surface only contribute to the red wing. The photon blueshift gradually increases as it is emitted farther away from the BH due to wind acceleration. Therefore, the case of thin disks and super-Eddington disks should be distinguishable by conducting a careful temporal study on the response at different energy ranges of the Fe line spectra to changes in the coronal continuum emission.

Blueshift and shape of the line: When studying Fig. 3.3a, one can see that the Fe line profile produced from the super-Eddington disk is both more blueshifted and symmetric with respect to the line centre than in any of the thin disk cases. In order to test if these two differences are generic, we have generated a phase-space plot in Fig. 3.5, where we have calculated these two line features for both the super-Eddington disk and a sample of 1500 thin disks. The thin disk sample is created by randomly sampling from a uniform distribution of BH spin between a Schwarzchild BH ($a = 0$) to a maximally rotating astrophysical BH ($a = 0.998$) (Thorne, 1974), and at the same time, random sampling from a uniform distribution of solid angles with inclination angles up to 80° (beyond which the disk is usually obscured by itself or some torus at large radius). We quantity the blueshift of the Fe line, $\tilde{F}$, as the percentage of the total integrated line intensity above $g = 1$. For the symmetry with respect to the line centre, $\tilde{w}$, we define it as the ratio between the width of the blue wing to the width of the red wing. Here, the line centre is defined as the place from where each side has half of the integrated line flux. The blue wing refers to the side bluer than the line centre containing $50 - 95\%$ of the line flux, and the red wing is the redder side containing $5 - 50\%$ of the total line flux. Both these parameters can be visualised in the two panels on the left-hand side in Fig. 3.5. The main panel on the right-hand side shows the two parameters, $\tilde{F}$ and $\tilde{w}$, calculated from the Fe line profiles of 1500 thin disks and the super-Eddington disk. It can be seen that the Fe line profiles from the super-Eddington disk have a much larger blueshift than all of the thin disk cases. Additionally, for thin disks, a strong correlation between the blueshift parameter, $\tilde{F}$, and the inclination angle of the observer can be seen, and depending on the angle, the lines can either be redshifted or blueshifted. (Here, we acknowledge that our Newtonian emissivity profile (Eq. 3.5) does not include light bending towards the BH, thus giving less weight to the innermost disk region. Therefore, the difference brought by the spin is underestimated and challenging to observe.) We can also see that the Fe line from the super-Eddington disk is significantly more symmetric (with width ratio $\tilde{w} \approx 1$) when compared to the thin disk cases. All the Fe lines produced by thin disks are skewed to the blue wing because of relativistic beaming effects and gravitational redshift. Therefore, the shape of the Fe line of a thin disk is generally less symmetric than in the super-Eddington case.

For the super-Eddington case, we have tested the robustness against the choice of lamp-post height ($h_{\rm LP} = 5 - 20\ R_g$) and optical depth of the reflection surface ($\tau = 1 - 5$). It can be seen that the assumptions on these parameters do not affect the qualitative conclusion.

In summary, we have demonstrated that the super-Eddington disk Fe lines should occupy a significantly different parameter space when analysing their rest-frame energy, blueshift and the symmetry of the lines profile. When combining these factors and aided with energy-lag analysis, one can distinguish super-Eddington accretion disks from thin disks.

3.5 Discussion and Future Work

In this letter, we have presented the first theoretical investigation of the Fe Kα fluorescent line profile produced when a realistic super-Eddington accretion disk, resolved in GRRMHD simulations, is irradiated by a lamppost corona. The main results are summarised below.

- The reflection surface of the coronal emission, where the Fe Kα fluorescent lines are produced, can be represented by the wall of an optically-thin funnel surrounded by optically-thick winds. Therefore, the geometry and motion of the reflection surface are very different from the standard case where reflection happens on the surface of a (razor) thin Keplerian disk.
- When viewed at large inclination angles from the pole, the optically-thick disk and wind produced in super-Eddington accretion will obscure the coronal emission and its reflection spectrum. Therefore, the Fe Kα lines can only be seen by observers looking at the system along the funnel direction.
- The ionisation level of the reflection surface is high, so the production of hotter Fe Kα lines with rest-frame energies of 6.97 or 6.7 keV is favoured over the cold 6.4 keV Fe line.
- The Fe line profile from a super-Eddington disk is primarily determined by the geometry of the funnel wall and the motion of the winds. The line spectrum is largely blueshifted. Also, photons emitted outside 10 R_g contribute more to the line flux due to the acceleration of the wind until large radii and the curvature of the reflection surface.
- The Fe line profile is robust against choosing different values of the optical depth to calculate the reflection surface, which indicates that our simple treatment of assuming that all coronal emission is reflected at a single τ-value surface is a good approximation of the realistic multiple-scattering scenario. The first-order features of the line profile are also robust against changes in the height of the lamppost corona.

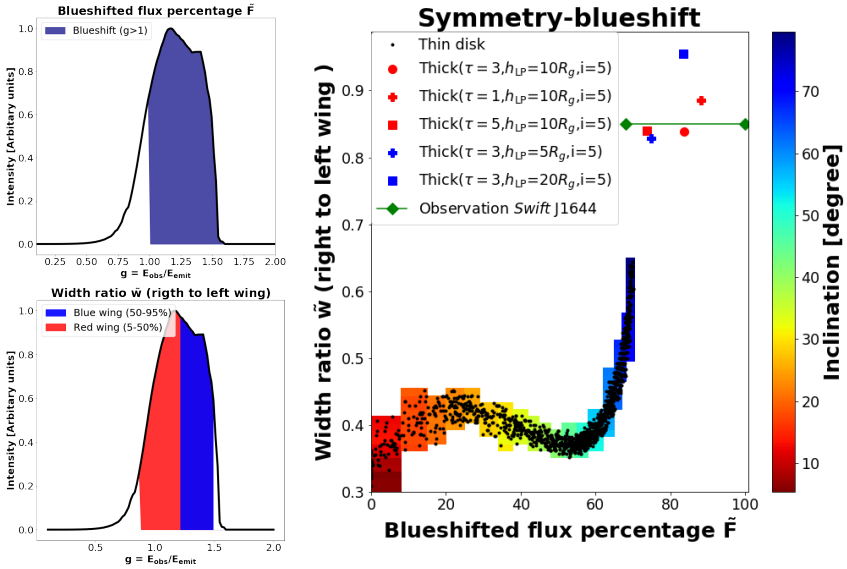

Figure 3.5: Phase-space diagram illustrating the morphological differences (in terms of the blueshift of the line and the symmetry of the line shape) between Fe Kα line profiles from super-Eddington and thin disks. The two panels on the left-hand side illustrate how we calculate the two phase-space parameters: **the blueshifted flux percentage ($\tilde{F}$)** and **the width ratio ($\tilde{w}$)**. Here, $\tilde{F}$ is defined as the percentage of the total integrated Fe line flux with observed energy above the rest-frame energy (or $g > 1$), and $\tilde{w}$ is the width ratio between the blue wing (where 50%-95% of the total line flux lies) to the red wing (with 5%-50% of the total line flux). In the main panel on the right-hand side, we show the phase-space diagram that illustrates these two line profile parameters calculated from both the simulated super-Eddington disk as well as approximately 1500 thin disks, which we randomly sampled from a uniform distribution of spin parameters between 0 and 0.998 and a uniform distribution of solid angles up to an inclination angle of 80°. In the phase space diagram, the Fe lines produced by the super-Eddington disk with different choices of τ and $h_{\rm LP}$ are marked with the prominent red/blue symbols on the top right corner. The thin disk lines are marked with black points, and the colour scheme in their background indicates the inclination angle, i, of the observer (red – face on, blue – edge on). One can see that $\tilde{F}$ is strongly correlated with i for thin disks. However, even the thin disks observed from the largest inclination angles do not produce lines as blueshifted as those from the super-Eddington disk. Furthermore, for thin disks, $\tilde{w}$ is always smaller than 1 since their line profiles are always skewed towards the blue side due to the gravitational redshift (which produces an extended red wing) and the relativistic beaming (which breaks the symmetry of the double-peak features). The Fe lines from super-Eddington disks are much more symmetric in shape since emission from the inner disk carries less weight due to the funnel geometry and the large terminal wind speed, which greatly broadens the blue wing of the Fe line spectrum. The Fe lines observed from the jetted TDE, Swift J1644, are marked with two green diamonds. (See Section 3.5 on why there are two data points.) Despite the uncertainty of the line profile, as indicated by the green line connecting the two points, the Fe Kα line observed from Swift J1644 clearly resides in the phase-space region predicted for super-Eddington accreting systems.

- By comparing the Fe Kα line profiles from the super-Eddington disk to those from thousands of thin disks sampled with random spin parameters and orientation,

we have shown that the Fe Kα line profile from a super-Eddington disk is distinctively more blueshifted and symmetric in shape with respect to the line centre. This result is also robust against the choice of the lamppost height and the reflection surface τ value.

Actually, the strongly blueshifted hot Fe Kα fluorescent lines from super-Eddington disks, as modelled here, have been observed from the jetted TDE, Swift J1644 (Kara et al., 2016b). TDEs are believed to be super-Eddington accretors if the BH mass is smaller than a few$\times 10^7$ $M_\odot$ (Rees, 1988; Evans & Kochanek, 1989; Ramirez-Ruiz & Rosswog, 2009; Guillochon & Ramirez-Ruiz, 2013; Dai et al., 2015; Wu et al., 2018), and the existence of a relativistic jet in Swift J1644 (Burrows et al., 2011; Bloom et al., 2011; Berger et al., 2012; De Colle et al., 2012) further supports that a transient magnetised thick disk has been formed by the stellar debris (Tchekhovskoy et al., 2014). In Kara et al. (2016b), the observed Fe line has energy peaked at $\approx$ 8 keV, which for an Fe Kα line with rest-frame energy of 6.97 keV corresponds to an energy-shift of $g = 1.15$ or an outflow velocity of $0.2 - 0.5$c (depending on the half-opening angle of the funnel and thus the lamppost height, see Fig. 3.3d). Also, since we are looking directly along the jet in this system, we are likely looking at the disk face-on. This strongly disfavors using a standard thin disk model to explain Swift J1644, since the Fe line can only be gravitationally redshifted from a face-on thin disk.

The observed Fe Kα line of Swift J1644 is illustrated together with the theoretically predicted values in the phase-space diagram in Fig. 3.5. We use two data points to illustrate Swift J1644 in the phase space. The two points have the same line symmetry parameter, $\tilde{w}$, but different blueshifted flux percentages, $\tilde{F}$. This is because the directly observed Fe line is very narrow, but the energy-lag analysis suggests that the line should be broader. For the broader line calculated from the lag, the blueshifted flux percentage is $\tilde{F} = 0.68$, and the width ratio is $\tilde{w} = 0.85$. If we use the directly observed narrower spectral line, then it is 100% blueshifted and seems very symmetric! This might be caused by over-ionisation (see Fig. 3.2b) or multi-scattering effects in the funnel or in the optically-thick wind. For this reason, we adopt the lower value of $\tilde{w}$ for both points. We acknowledge that the discrepancy in the line width has not been fully understood, so we link the two data points with a line to represent the uncertainty. Nonetheless, it can clearly be seen that both of the two Swift J1644 data points reside in the "super-Eddington disk zone" on the phase-space diagram, where the line blueshift is higher, and the line shape is more symmetric compared to thin disks. A reminder is that the blueshifted flux percentage, $\tilde{F}$, is calculated assuming a 6.97 keV rest-frame energy. Therefore, the observed blueshift of this event is even harder to be explained using thin disks.

We aim to extend the fruitful study of X-ray reverberation from thin disk models to super-Eddington accretion disk geometries. In this letter, we have shown that the Fe Kα fluorescent line profiles can be used to effectively distinguish super-Eddington systems from sub-Eddington systems, which is supported by the resemblance of the Fe

line profiles observed from Swift J1644 to the lines modelled here. Future studies, such as investigating the energy-lag spectrum, calculating the irradiation profile in a rigorous GR setting, experimenting with different corona and disk geometries and tracing multiple scatterings of photons in the optically thick winds, can all improve our understanding of this topic. The study of X-ray reverberations of super-Eddington accretion flow can be widely applied to probe the funnel geometry and wind launching in TDEs, ULXs and super-Eddington Narrow-Line Seyfert 1 Galaxies, which are likely all super-Eddington systems with different Eddington ratios. Such studies can also show how quasars in the early universe can produce winds and provide kinetic energy feedback to their host galaxies.

3.6 Acknowledgement

We acknowledge helpful discussions with Roger Blandford, Cole Miller, Sandra Raimundo, Corbin Taylor, Marianne Vestergaard, Dan Wilkins, and Yajie Yuan. We also thank the anonymous referee for constructive comments. We are indebted to the David and Lucile Packard Foundation, the Heising-Simons Foundation and the Danish National Research Foundation (DNRF132) for their support. Some of the simulations carried out for this project were performed on the University of Copenhagen high-performance computing cluster funded by a grant from VILLUM FONDEN (project number 16599).

Chapter 4

X-ray Reverberation

The content of this chapter is drawn from the published paper: Relativistic X-Ray Reverberation from Super-Eddington Accretion Flow by Thomsen L. L., Dai L., Kara E., Reynolds C., 2022, The Astrophysical Journal, 925, 151. doi:10.3847/1538- 4357/ac3df3 with minor consistency and grammar modifications. As the paper's first author, I conducted the general relativistic ray-tracing simulations to calculate the time-dependent Fe Kα line, analysed and interpreted the results, and contributed significantly to writing the paper.

The summary of the paper is as follows: X-ray reverberation is a powerful technique which uses the echoes of the coronal emission reflected by a black hole accretion disk to map out the inner disk structure. While the theory of X-ray reverberation has been developed almost exclusively for standard thin disks, reverberation lags have recently been observed from likely super-Eddington accretion sources such as the jetted tidal disruption event Swift J1644+57. In this paper, we extend X-ray reverberation studies into the regime of super-Eddington accretion, focusing on investigating the lags in the fluorescent Fe Kα line region. We find that the coronal photons are reflected mainly by the fast and optically thick winds launched from the super-Eddington accretion flow, and this funnel-like reflection geometry produces lag-frequency and lag-energy spectra with unique observable characteristics. The lag-frequency spectrum exhibits a step-function-like decline near the first zero-crossing point. As a result, the magnitude of the lag scales linearly with the black hole mass for a large parameter space, and the shape of the lag-energy spectrum remains almost independent of the choice of frequency bands. Not only can these features be used to distinguish super-Eddington accretion systems from sub-Eddington systems, but they are also key for constraining the reflection geometry and extracting parameters from the observed lags. When fitting the observed reverberation lag of Swift J1644+57 to our modelling, we find that the super-Eddington disk geometry is slightly preferred over the thin disk geometry, and we obtain a black hole mass of 5-6 million solar masses and a coronal height of around 10 gravitational radii.

4.1 Introduction

The accretion of gas onto supermassive black holes (SMBHs) plays a significant role in shaping the evolution of the universe. The well-established $M_{\rm BH} - \sigma_{\rm bulge}$ relation between the mass of the SMBH ($M_{\rm BH}$) and the velocity dispersion of the stars in the bulge ($\sigma_{\rm bulge}$) indicates that the growth of the SMBHs are coupled to the growth of their host-galaxies (Magorrian et al., 1998; Kormendy & Ho, 2013). One key factor contributing to this scaling relation is believed to be the feedback in the forms of radiation, winds and relativistic jets produced by active galactic nuclei (AGNs) (Silk & Rees, 1998; Heinz et al., 2006). The radiation produced from a black hole (BH) system is often expressed in terms of its Eddington luminosity $L_{\rm Edd}$:

$$L_{\rm Edd} \approx 1.26 \times 10^{38} \left(\frac{M_{\rm BH}}{M_\odot} \right) \ {\rm erg\ s^{-1}} \tag{4.1}$$

where $M_\odot$ is the solar mass. The accretion rate corresponding to $L_{\rm Edd}$ is called the Eddington accretion rate $\dot{M}_{\rm Edd}$:

$$\dot{M}_{\rm Edd} = \frac{L_{\rm Edd}}{\eta\, c^2}, \tag{4.2}$$

where c is the speed of light and η is the radiative efficiency. For this study, we adopt the conventional value of 0.1.

The recent discovery of massive quasars with $10^{9-10} M_\odot$ at large redshifts of $z = 6 - 8$ (Mortlock et al., 2011; Wu et al., 2015; Bañados et al., 2018) promotes the idea that super-Eddington accretion, in which gas is accreted onto a black hole faster than the Eddington accretion rate, likely plays an important role in the growth of quasars in the early universe. Many theoretical studies have been conducted to study super-Eddington accretion around black holes. In the conventional, semi-analytical models such as the 'slim disk' or the 'Polish doughnut' model, the accretion flow does not produce a wind (see the review by Abramowicz & Fragile, 2013). However, recent general relativistic radiation magnetohydrodynamic (GRRMHD) simulations of super-Eddington disks (Ohsuga et al., 2009; Jiang et al., 2014; McKinney et al., 2014; Sądowski et al., 2014) have unanimously shown optically and geometrically thick winds launched by the immense radiation pressure in the disk. Such winds have anisotropic profiles with velocity decreasing and density increasing as the inclination deviates from the pole (Sądowski & Narayan, 2016; Dai et al., 2018). The ultrafast outflow (UFO) component, with speeds of $v_r \approx$ few $\times\, 0.1c$, has been detected in several super-Eddington sources such as ultra-luminous X-ray sources (ULXs) (e.g., Walton et al., 2016; Pinto et al., 2016, 2017; Kosec et al., 2018) and tidal disruption events (TDEs) (e.g., Kara et al., 2018). Since powerful super-Eddington winds from AGNs can deeply impact their host galaxies (King, 2003), it is desirable to have a method to probe their geometry and energy directly.

X-ray reverberation is a technique developed to probe the structure of the BH accretion disk by analysing the time dependence and energy shifts of photons. This technique has been widely applied to study AGNs and X-ray binaries (e.g. Fabian et al., 1989; Nowak et al., 1999; Reynolds et al., 1999; Zoghbi et al., 2012; Wilkins & Fabian, 2012; Uttley et al., 2014; Cackett et al., 2014, 2021). These works usually adopt the geometry of a point-like lamppost corona irradiating a geometrically thin, Keplerian disk. In this standard picture, a very hot and compact corona is placed above the BH from where it emits non-thermal X-ray photons. About half of the coronal photons freely escape to the observer, while the other half irradiates the cold accretion disk, giving rise to a reflection spectrum. The most prominent feature of the reflection spectrum is the Fe Kα fluorescent lines, produced from the photoionisation of an inner K-shell electron of Fe (Fabian et al., 1989; Matt et al., 1993). Due to general relativistic (GR) effects and the relativistic Doppler effect between the rotating disk and the observer, the Fe line profile becomes broadened and skewed. The spectral shape of the Kα lines can be used to effectively probe the innermost disk geometry and constrain the BH spin in systems which have geometrically thin disks rotating with relativistic Keplerian speed and truncated at the innermost stable circular orbit (ISCO) (e.g., Reynolds et al., 1999; Reynolds, 2014; Cackett et al., 2014; Taylor & Reynolds, 2018a). Moreover, temporal changes in the reflection spectrum are expected to lag behind the driving coronal continuum emission because the reflected photons need to travel a longer distance to the observer and are gravitationally time delayed (Shapiro, 1964). Therefore, resolving these lags can allow us to further constrain the BH parameters along with the coronal geometry and location (Wilkins et al., 2016; Cackett et al., 2014) as well as the vertical disk structure (Taylor & Reynolds, 2018b).

We propose extending the well-established X-ray reverberation technique to probe the structure of super-Eddington accretion flow. In this accretion regime, the coronal photons are expected to be reflected by the optically thick winds launched from the geometrically thick accretion flow. Therefore, the reflection and reverberation signals should, in principle, give us an insight into the geometry and kinematics of the wind. The best observational evidence of X-ray reverberation from super-Eddington accretion flow so far has come from the jetted TDE Swift J164449.3+573451 (Swift J1644 hereafter) (Burrows et al., 2011; Bloom et al., 2011; Levan et al., 2011; Zauderer et al., 2011). In this event, a star was disrupted by a SMBH and its debris accreted onto the SMBH at a super-Eddington accretion rate (Rees, 1988; Evans & Kochanek, 1989; Guillochon & Ramirez-Ruiz, 2013). The SMBH mass is estimated to be a few $\times 10^6\ M_\odot$ constrained by X-ray variability timescales. The very high isotropic X-ray luminosity can be explained using a relativistic jet launched from the magnetised accretion disk and beamed towards the observer (Tchekhovskoy et al., 2014). A highly blueshifted Fe Kα line and a relatively symmetric lag-energy spectrum in the Fe line region have been observed from this system (Kara et al., 2016b). Since the inner disk is likely aligned with the jet and therefore observed face-on, the most plausible explanation of the observed Fe line blueshift is that the observer is viewing down an optically thin funnel surrounded by

the optically-thick winds launched by the super-Eddington disk, and the fast-moving wind reflects the coronal photons. Inspired by this discovery, we have previously conducted a theoretical study (Thomsen et al., 2019) to investigate the characteristics of the Fe Kα lines produced from super-Eddington accretion disks, in which we have demonstrated that such disks do produce Fe Kα lines with signatures consistent with the one observed in Swift J1644.

In this paper, we extend the groundwork in Thomsen et al. (2019) to include the temporal response of the Fe Kα fluorescent line and further implement rigorous GR calculations from the corona to the reflection surface. The paper is structured as follows: In Section 4.2, we show the geometry, dynamics and ionisation of the reflection surface for the super-Eddington accretion flow. We also calculate the emissivity profile under rigorous GR. In Section 4.3, we present the 2D transfer function as well as the energy and frequency-dependent X-ray reverberation lags. Here we compare the lags produced by super-Eddington disks and standard thin disks and show their characteristics are very different. In Section 4.4, we apply our model to the observed lags of Swift J1644 and fit various physical parameters. Lastly, in Section 4.5, we summarise our findings and discuss the prospect of using the X-ray reverberation technique to effectively extract information from super-Eddington accretion systems.

4.2 Reflection Geometry and Emissivity Profile

4.2.1 The Geometry and Kinematics of the Reflection Surface

Following Thomsen et al. (2019), we use the super-Eddington disk profile from Dai et al. (2018) simulated using the GRRMHD code HARMRAD (McKinney et al., 2014, 2015) for this study. The simulated disk surrounds a SMBH with a mass of $M_{\rm BH} = 5 \times 10^6\ M_\odot$ and a fast spin with the dimensionless spin parameter $a = 0.8$. The disk has an average accretion rate of $\sim 15\ \dot{M}_{\rm Edd}$ and an average outflow rate of $\sim 10\ \dot{M}_{\rm Edd}$.

For super-Eddington accretion flow, the coronal photons are reflected by the funnel wall, which is surrounded by optically thick winds. We illustrate this concept in Fig. 4.1a by showing the time and azimuthally-averaged disk profile. The relativistic jet launched by the Blandford-Znajek process (Blandford & Znajek, 1977) is marked by the dark blue regions where the magnetic pressure dominates over the gas pressure. The density inside this region is ignored since the gas density at the base of the jet can be artificially boosted due to numerical reasons. The disk wind, launched by high radiation and magnetic pressure, is denser and slower towards the equator. This means an optically thin funnel is formed in the polar region, which has a half-opening angle around $10 - 15^\circ$ for the simulated disk we use. Therefore, an observer needs to look directly into the funnel to see the coronal emission and its reflection. If viewed at larger inclination angles, the X-ray photons are likely absorbed and reprocessed in the optically thick disk and wind.

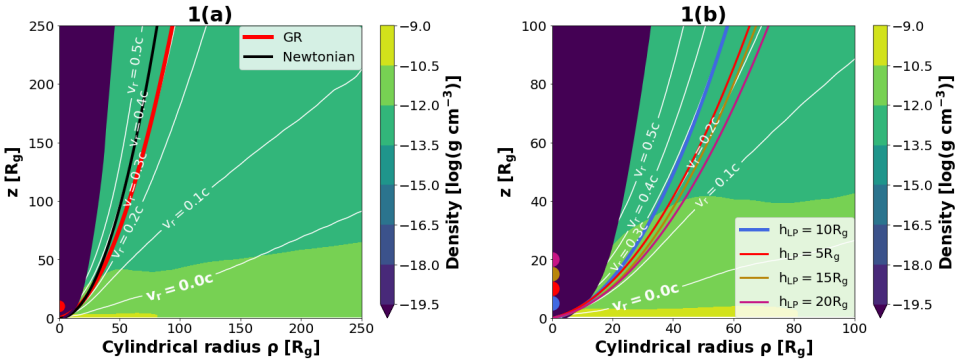

Figure 4.1: The corona reflection geometry for the simulated super-Eddington disk. The x-axis is the cylindrical radius ρ and the y-axis is the vertical height z. The background colour depicts the density profile of the disk. The jet is illustrated as the dark blue region around the pole, which is assumed to be optically thin. The wind closer to the pole has a lower density and moves faster, with the white lines showing contours of constant v_r. We place an artificial corona at some height $h_{\rm LP}$ and calculate the reflection surface of the coronal emission as the electron-scattering photosphere with a certain Thompson optical depth τ. **1a. Comparison between the GR and the Newtonian reflection surface:** For $h_{\rm LP} = 10R_g$ and $\tau = 3$, the thick red curve shows the reflection surface calculated using rigorous GR ray-tracing, while the thick black curve shows the reflection surface calculated using Newtonian calculation. **1b. Reflection surfaces for different $h_{\rm LP}$:** The red, thick curve is the same as the reflection surface in Fig. 4.1a with $h_{\rm LP} = 10R_g$, while the thin curves show the GR reflection surfaces when the lamppost corona is placed at different $h_{\rm LP}$. It can be seen that the coronal reflection surface is not sensitive to $h_{\rm LP}$.

We place an artificial lamppost corona at a few gravitational radii (R_g) above the black hole, which irradiates isotropically in its local (Minkowski) frame (see Section 2.1.2 for isotropic ray-tracing from a point source in a curved space-time). While we recognise that the coronal photons should go through multiple scatterings inside the thick accretion flow, we take a simplified approach by assuming all the reflected photons originate from a single reflection surface in this work. This reflection surface is obtained by following the geodesics of photons emitted by the corona using our GR ray-tracing code (see Section 2.1.2 for the description) until a certain optical depth τ is reached. Furthermore, we adopt the special relativistic correction to the optical depth, τ, to reflect that photons moving in the same direction as the gas flow should generally travel longer before being scattered (Abramowicz et al., 1991):

$$\tau = \int \gamma \left(1 - \beta \cos(\theta)\right) \kappa_{\rm es,0}\, \rho_0\, ds, \tag{4.3}$$

where $\kappa_{\rm es,0} = 0.34$ cm^2 g^{-1} is the Thomson electron-scattering opacity (assuming solar abundance), ρ_0 is the rest-frame gas density, θ is the angle between the photon momentum and the gas velocity, and ds is the length of the light path in the curved space-time. Here β and γ are the magnitudes of the 3-velocity and the Lorentz factor between the frame of the gas and that of the Zero-Angular-Momentum-Observer (ZAMO) in the

Kerr space-time around the black hole. This rigorously relativistic approach used to calculate the reflection surface differs from the Newtonian approach used in Thomsen et al. (2019).

We show in Fig. 4.1a the reflection surface obtained using this GR approach in comparison with the Newtonian one, both using the $\tau = 3$ photosphere from a lamp-post corona at the height of $h_{\rm LP} = 10R_g$. To the first order, both surfaces lie in the optically thick, fast-moving winds with speeds at few$\times 0.1c$. The relativistic correction in Eq. 4.3 causes the effective opacity to be smaller since the photon and gas generally move in the same direction. Therefore, the GR reflection surface lies at a larger inclination angle from the pole, with a slightly lower terminal speed than the Newtonian one. We also vary the lamppost height between $5 - 20R_g$ and find that the reflection surface stays almost unchanged, as seen in Fig. 4.1b. Therefore, for simplicity, we adopt the reflection surface with $\tau = 3$ calculated for lamppost corona at $h_{\rm LP} = 10R_g$ throughout this study unless otherwise specified.

Next, we check the kinematics of the reflection surface. Fig. 4.2a shows the equivalent 3-velocity of the gas along the reflection surface. At small cylindrical radii $\rho < 4R_g$, the reflection surface lies within the disk inflow region, thus having negative radial velocities. Beyond $\rho \approx 10R_g$, the reflection surface lies within fast winds, and the radial motion dominates over its rotation.

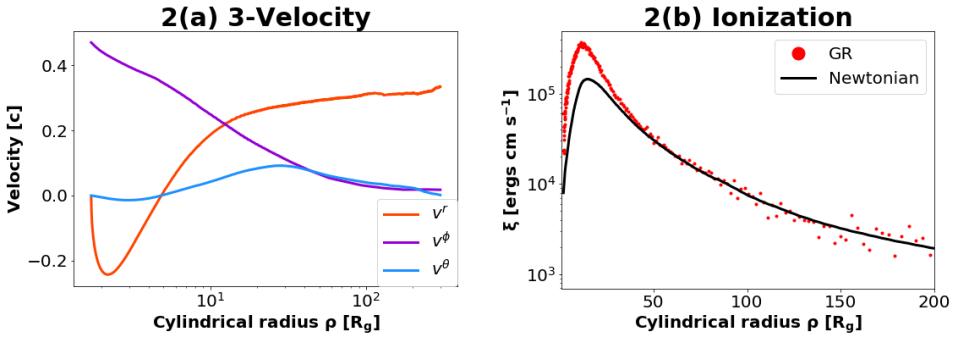

Figure 4.2: 2a. The equivalent Newtonian 3-velocity of the gas along the reflection surface. The wind accelerates quickly, and the out-flowing motion dominates over-rotation starting from $\rho \approx 10\ R_g$, after which the wind quickly reaches a terminal radial velocity of about 0.3c. **2b. The ionisation parameter ξ along the reflection surface.** By accounting for the GR effects (red dotted curve), ξ is a few times larger in the inner disk region as compared to that obtained using Newtonian calculations (thin black curve).

Last, we investigate the X-ray ionisation parameter of the gas, ξ, which determines whether Fe Kα fluorescent lines can be produced, and if so, which lines (i.e., with rest-frame energy of 6.4, 6.7 or 6.97 keV) are produced (Ross et al., 1999; Ballantyne & Ramirez-Ruiz, 2001; García & Kallman, 2010). The ionisation parameter is calculated as (Reynolds & Begelman, 1997):

$$\xi(r) = \frac{4\pi F_{\rm X-ray}}{n(r)}, \tag{4.4}$$

where $n(r)$ is the gas number density at the reflection surface and $F_{\rm X-ray}$ is the hard X-ray flux over certain energy band (e.g., Ballantyne & Ramirez-Ruiz, 2001, uses 0.01-100keV). For this study, we assume that the efficiency of producing hard X-rays from accretion η_X is about 1%, similar to that in thin disks (Reynolds et al., 1999). Therefore, $F_{\rm X-ray}$ is scaled so that the total hard X-ray luminosity of the corona from the simulated disk is $L_{\rm X-ray} \approx \eta_x \dot{M}c^2 \approx 10^{44}$ erg s^{-1}. As shown in Fig. 4.2b, ξ is enhanced by a factor of a few in the inner regions when including the GR effects (with details to be explained in the next section). ξ is high in the super-Eddington case ($10^3 - 10^5$ ergs cm s^{-1}) compared to the thin disk scenarios ($\xi \lesssim 100$ ergs cm s^{-1}) since the reflection surface lies in the wind with relatively low densities. The high ξ value favours the production of the Fe Kα lines with larger rest-frame energies (6.97 and 6.7 keV) over the 6.4 keV line (Ballantyne & Ramirez-Ruiz, 2001), although in this paper, we assume the same rest-frame energy for the Fe Kα lines produced throughout the entire reflection surface and present the results in terms of the energy shift factor, g, between the observed line energy and the emitted line energy.

4.2.2 The Emissivity Profile

The emissivity profile gives the strength of the coronal irradiating emission received at each annulus of the photosphere. By following the photons from the corona to the reflection surface using GR ray-tracing, we automatically account for the light-bending effects, the energy shifts of the photons, and the Shapiro time delay. Other general relativistic effects, such as the general relativistic correction to the area of the reflection surface, need to be addressed separately. Following Wilkins & Fabian (2012); Dauser et al. (2013); Gonzalez et al. (2017), the emissivity profile, $\epsilon(\rho)$, is given by:

$$\epsilon(\rho) \propto \frac{N(\rho, d\rho)}{g_{\rm LP}^{\Gamma} \gamma A(\rho, d\rho)}. \tag{4.5}$$

Here $N(\rho, d\rho)$ is the number of coronal photons hitting an annulus of the photosphere at cylindrical radius ρ with a width $d\rho$, and $A(\rho, d\rho)$ is the area of the annulus as seen by the ZAMO observer at the reflection surface. In order to calculate the area in a rigorous GR setting, we perform a Jacobian transformation from $(r(\rho), \theta(\rho), \phi)$ to (ρ, ϕ), and the details are presented in Section B.2 following the approach in Taylor & Reynolds (2018a). The Lorentz factor, γ, accounts for the length contraction of the area between the ZAMO observer and the rest frame of the photosphere. Lastly, $g_{\rm LP}$ is the energy shift between the photons emitted from the corona ($E_{\rm LP}$) and the photons received by the reflection surface ($E_{\rm disk}$), which is defined as:

$$g_{\rm LP} = \frac{E_{\rm LP}}{E_{\rm disk}} = \frac{\left(p_\mu u^\mu\right)_{\rm LP}}{\left(p_\nu u^\nu\right)_{\rm disk}}. \tag{4.6}$$

We propagate photons using the GR ray-tracing code, and we calculate the energy as the product of the photon's four-momentum (p_μ) and the gas' four-velocity (u^μ) evaluated at observation/emission. The power of the energy shift in Eq. 4.5 arises from assuming a power-law emission from the corona with a photon index Γ (Dauser et al., 2013; Gonzalez et al., 2017). We adopt the conventional value $\Gamma = 2$ for this study, which is also appropriate for Swift J1644 (Burrows et al., 2011). A detailed derivation of isotropic emission in a GR setting (how to transform from one frame to another) is presented in Section 2.1.2 and Appendix B.1.1.

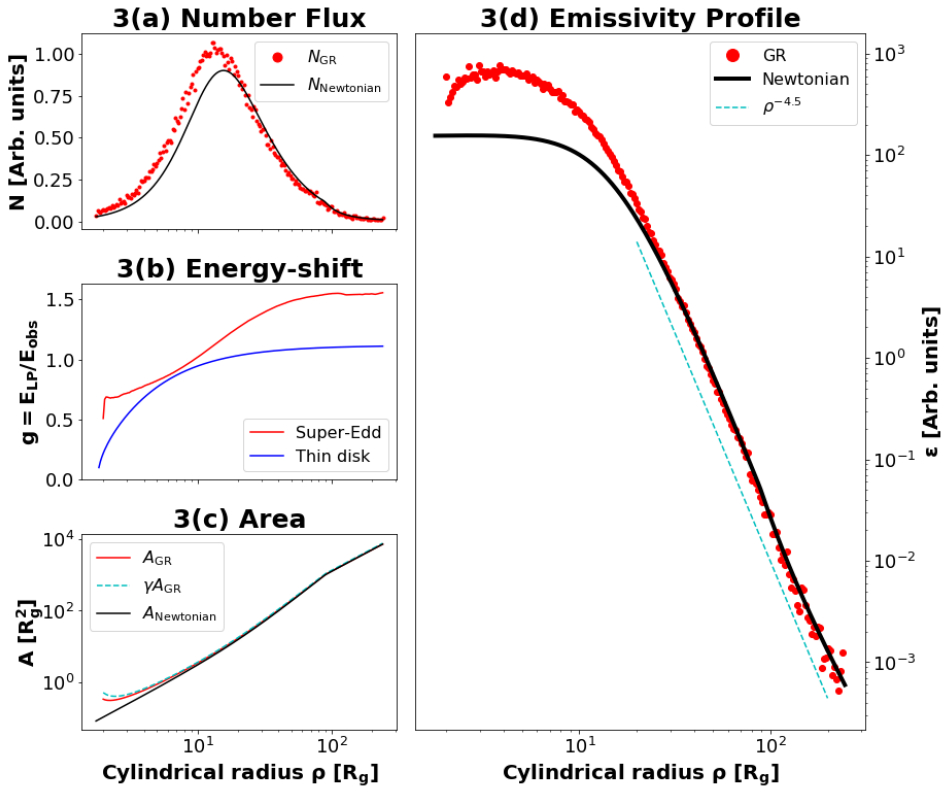

Figure 4.3: We show each component contributing towards the emissivity profile. **3a) The number flux, *N*:** The GR number flux is plotted together with the Newtonian one. We see the GR light-bending effects enhance the flux of photons in the inner region. **3b) The photon energy shift, g_{LP}:** We show the ratio between the energy of the emitted photons from the corona and the energy as seen by the gas elements in the reflection surface for both the super-Eddington and thin disks. $g_{LP} < 1$ means the photon, as seen by the disk, is blueshifted compared to emission. **3c) The area, *A*:** We show 3 different areas: the classical Newtonian area (black solid), the proper area as seen by the ZAMO (cyan dashed), the relativistic proper area as seen by the reflection surface (red solid). One can see that the classical area substantially undervalues the area within $\rho = 5R_g$ as compared to the two proper areas. **3d) The emissivity profile, ϵ of the super-Eddington accretion disk:** We show the GR emissivity profile (red dotted) (Eq. 4.5) in comparison to the Newtonian one (black line). The GR effects enhance the emission from the inner region. Approximately, the emissivity profile follows a power law $\propto \rho^{-4.5}$ (cyan dashed) in the outer region and remains rather flat in the inner region.

We show in Fig. 4.3 how each component above contributes to the total emissivity profile. In Fig. 4.3a, we show the number flux, $N(\rho, d\rho)$, of photons hitting the annulus calculated using the GR or Newtonian approach. The light-bending effect is clearly illustrated by the enhanced flux in the innermost $\rho < 20R_g$ region. Next, in Fig. 4.3b, we show the photon energy shift, $g_{\rm LP}$, from the corona to the reflection surface as a function of the cylindrical radius for both the super-Eddington disk and a standard thin disk. For both disks, the coronal photons experience gravitational blueshift when travelling down to the inner region of the reflection surface. For the super-Eddington disk geometry, the inner reflection surface is embedded in the disk region with a large inflow velocity, which gives a Doppler redshift for the coronal photons and therefore reduces the overall blueshift of the photons. At the outer region of the super-Eddington accretion flow, the reflection surface lies in the outflow, which moves away from the incoming coronal photons. Therefore, the energies of the coronal photons received by the reflection surface are Doppler redshifted. In Fig. 4.3c, we show the relativistic proper area, $A(\rho, d\rho)$, of the reflecting surface compared to the Newtonian area. In the innermost region, the relativistic area is amplified, and the Lorentz factor further enhances this effect, which will slightly decrease the emissivity/irradiation in this region.

Putting these together, we obtain the GR emissivity, $\epsilon(\rho)$, as shown in Fig. 4.3d, which is compared to the Newtonian analytical emissivity profile calculated in Thomsen et al. (2019). The GR emissivity profile is drastically enhanced in the inner region ($\rho \lesssim$ few $\times 10R_g$) mainly due to light-bending effects and the photon energy shift from the corona to the accretion flow. This increases the weight of the fluorescent lines produced in the inner disk regions. $\epsilon(\rho)$ can be fitted to a power law of $\epsilon \propto \rho^{-4.5}$ far away, but stays roughly constant within $\rho \approx 10R_g$.

4.3 Results

4.3.1 2D Transfer Function

We first construct the 2D transfer function, $\Psi(E, t)$, also known as the impulse response function (Reynolds et al., 1999; Uttley et al., 2014). $\Psi(E, t)$ describes how the photons, emitted by an instantaneous coronal flare, travel to different locations on the reflection surface and then get reflected towards the observer by recording the unique observed energy (E), time delay (t), and intensity ($I_{\rm obs}$) of each reflected photon. Here, t measures the time difference between the arrival time of the reflected photons and the initial coronal flare. The energy shift of the reflected photon between emission and observation is calculated as $g = E_{\rm obs}/E_{\rm emit} = (p_\mu u^\mu)_{\rm obs}/(p_\mu u^\mu)_{\rm emit}$. The observed intensity of the photon goes as $I_{\rm obs} \propto g^4$ (see Eq. 2.11 for derivation), which is weighted using the relativistic emissivity profile ϵ obtained in Section 4.2.2.

We show the 2D transfer functions of the super-Eddington disk and a standard razor-thin disk with the same BH spin of $a = 0.8$ for a direct comparison in Fig. 4.4.

Throughout this study, unless otherwise specified, we adopt $h_{\rm LP} = 10R_g$, a photosphere extending to $r_{\rm max} = 1000R_g$, and an observer located at $r_{\rm obs} = 5000R_g$. For the super-Eddington accretion flow, we put the observer at an inclination angle of $i = 5^\circ$, which is within the half-opening angle of the funnel is $\theta_{\rm funnel} = 15^\circ$. For the thin disk, the observer inclination is put at either $i = 5^\circ$ (low inclination) or $i = 80^\circ$ (high inclination). The 2D transfer functions are shown with time delays (t) on the x-axis and energy shifts (g) on the y-axis. The colour indicates the intensity, $I_{\rm obs}$, with the darkest regions being the strongest. By integrating $\Psi(E,t)$ over the energy, we obtain the 1d response function, $\Psi(t)$, which illustrates the intensity evolution of the reflected photons and is shown in the bottom panels of the subfigures. Likewise, the Fe Kα line spectrum, $\Psi(E)$, is the time-averaged of $\Psi(E,t)$ and is presented in the left-hand-side panels of the subfigures [1].

We give a brief description of the behaviours of the 2D transfer functions, starting from the razor-thin disk one, which has been extensively discussed in the literature (Reynolds et al., 1999; Cackett et al., 2014; Ingram et al., 2019; Wilkins et al., 2016, 2020). For a face-on thin disk (Fig. 4.4e), it takes longer for photons to travel to the outer part of the disk and get reflected towards the observer (upper branch), while photons reflected closer to the BH experience stronger Shapiro time delay and gravitational redshift (lower branch). Therefore, the first arriving photons are reflected at a few R_g outside the inner edge of the disk. For an edge-on thin disk (Fig. 4.4f), the photons reflected by the outer part of the disk on the side closest to the observer arrive first. Afterwards, photons reflected by the inner disk are gradually received, where Doppler-shift largely broadens the width of the observed energy spectrum. Then the maximum intensity is reached when photons from the innermost region of the disk arrive. And eventually, the photons reflected by the outer disk on the other side reach the observer.

The $\Psi(E,t)$ of the super-Eddington disk for different τ-surfaces and lamppost heights are shown in Fig. 4.4a, 4.4b, 4.4c and 4.4d. The overall shapes of these functions are similar to that of the low-inclination thin disk case. However, there are two notable differences: 1) The observed energy is mainly blueshifted due to the fast outflow speed of the funnel. 2) Most of the reflected photons are received within a short time delay range, which results from the narrow funnel reflection geometry in super-Eddington accretion. We can also see that varying the τ-surface or $h_{\rm LP}$ does not change the first-order behaviour of $\Psi(E,t)$. In general, decreasing the coronal height gives shorter time delays to the reflected photons. At the same time, the reflected spectrum gets less blueshifted and broader since a lower corona height illuminates the inner, slower-moving part of the funnel more.

In Fig. 4.5, we highlight the average time delay as a function of energy shift. For thin disks, we can see that the photons with the longest time delays have $g \approx 1$, meaning these photons originate from the outer part of the disk. For super-Eddington disks,

[1]. For visualisation purposes, we have produced videos showing how a coronal flare illuminates the accretion flow for a super-Eddington disk https://youtu.be/MYeRAN9MjB4; a low-inclination thin disk: https://youtu.be/pVurM3540F4; a high-inclination thin disk: https://youtu.be/pVurM3540F4

the photons with the longest time delays also have the most significant redshifts (innermost region) or the largest blueshifts (outermost region). Also, the average time delays from super-Eddington disks are much smaller due to their reflection geometry.

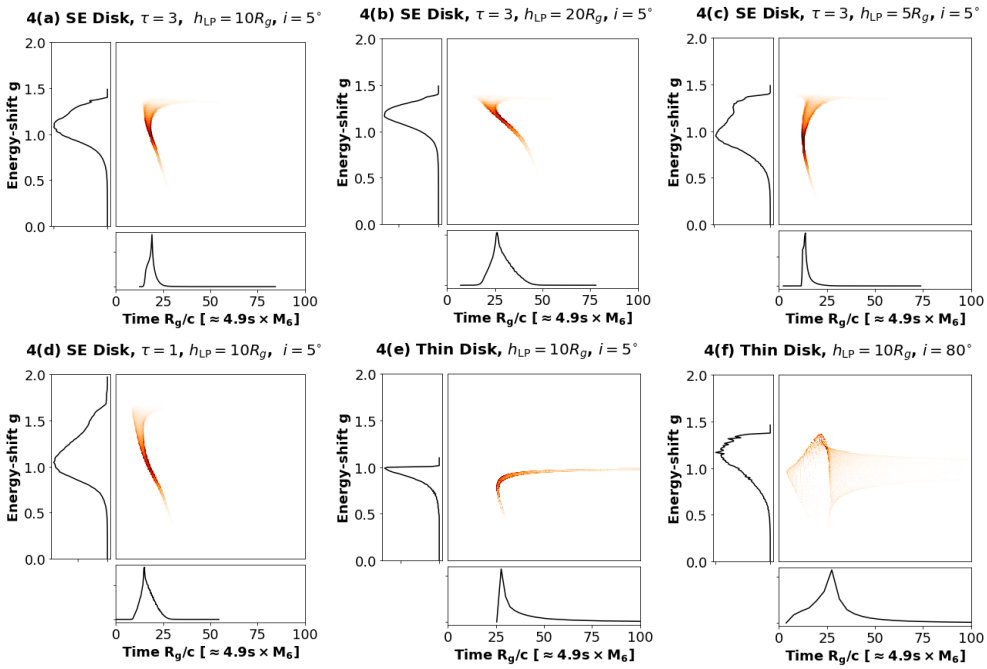

Figure 4.4: 2D transfer functions for different super-Eddington (SE) and thin disk configurations. The BH spin for all configurations is $a = 0.8$. The x-axis shows the time delay of the reflected photons in gravitational units, which can be converted to real units as $R_g/c \approx 4.9s \times M_6$, with $M_6 \equiv M_{\rm BH}/10^6 M_\odot$. The energy shift is shown on the y-axis. A darker red colour indicates stronger intensity, $I_{\rm obs}$. The 1d response function, $\Psi(t)$, and the Fe Kα line profile, $\Psi(E)$, are shown respectively in the bottom and left panels of each subfigure. For SE disks, we fix the inclination angle to $i = 5^\circ$ and vary the optical depth of the reflection surface (τ) and the lamppost height between $h_{\rm LP} = [5 - 20R_g]$ in Fig. 4.4a - 4.4d. As a comparison, for the thin disks, we have two inclination angles: face-on ($i = 5^\circ$) (Fig. 4.4e) and edge-on ($i = 80^\circ$) (Fig. 4.4f).

4.3.2 Frequency and Energy-Dependent Lags

The variations of reflection-dominated parts of the spectrum, such as the soft excess (0.1-1) keV band and the Fe Kα (4-7) keV band, are expected to lag behind that of the continuum-dominated part of the spectrum. Since the first detection of Fe K-lags in AGNs by Zoghbi et al. (2012), more than 20 AGNs with Fe K-lags have been observed and found to lag a few 100-1000s behind the continuum (see Kara et al., 2016a; Frederick et al., 2018; Vincentelli et al., 2020, and references therein). This lag timescale corresponds to the travelling time of photons reflected from the inner disk within a few gravitational radii ($t = $ few $\times R_g/c = $ few $\times 49 \frac{M_{\rm BH}}{10^7 M_\odot} s$). Due to the limitations of current X-ray observations in terms of resolution, it is not possible to fully recover the 2D transfer function of the Fe Kα line for direct comparison. However, we can compare

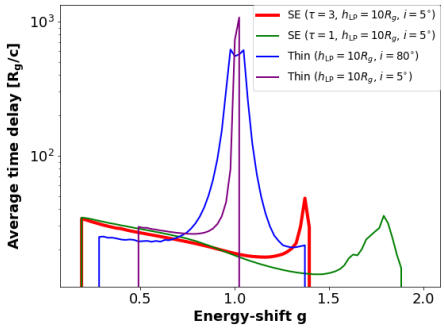

Figure 4.5: The average arrival time of photons as a function of energy shift for different disk configurations. For thin disks, the longest average arrival time corresponds to $g \approx 1$. For super-Eddington cases, it is found that the longest photon travel time corresponds to the regions with the largest red/blueshifts, i.e., the innermost/outermost regions of the reflection surface.

our models to the observed energy and frequency-dependent lags between the reflection and continuum-dominated energy bands. This is achieved by taking the Fourier transform of the 2D transfer function. This technique has been successfully applied in X-ray reverberation studies of AGNs (Zoghbi et al., 2013; Kara et al., 2014; Cackett et al., 2021).

We adopt the standard approach in Nowak et al. (1999), Cackett et al. (2014), and Uttley et al. (2014) to calculate the frequency and energy-dependent lags between the Fe line and the continuum. Assuming the coronal flare is a δ-function impulse, the frequency-dependent lags are calculated as (Cackett et al., 2014):

$$\phi(f) = \tan^{-1}\left(\frac{R \times \Im\big(\tilde{\Psi}(f)\big)}{1 + R \times \Re\big(\tilde{\Psi}(f)\big)}\right), \quad \text{and} \quad T(f) = \frac{\phi(f)}{2\pi f}, \tag{4.7}$$

where $\tilde{\Psi}(f)$ is the Fourier transform of the energy-averaged 1d response function: $\tilde{\Psi}(f) = \int_0^\infty \Psi(t) e^{-i2\pi f t} dt$, which is normalised ($\int \Psi(t) dt = 1$). The imaginary and real part of $\tilde{\Psi}(f)$ are respectively $\Im\big(\tilde{\Psi}(f)\big)$ and $\Re\big(\tilde{\Psi}(f)\big)$. Here, $\phi(f)$ and $T(f)$ are the phase and time lag at Fourier frequency, f, respectively. The diluting factor, R, is the ratio between the reflected flux and the driving coronal flux, accounting for the dilution of the reflected Fe line flux by the continuum flux. A value of $R = 1$ means an equal contribution of the continuum and reflected flux in the given energy bin. Furthermore, we assume R to be constant across the entire Fe line since we do not model the reflected flux strength relative to the continuum level. Therefore, the diluting factor decreases the overall lags by a factor $\sim R/(1+R)$.

The energy-dependent lags are calculated similarly. However, instead of averaging over all energies, we calculate the average lag in a given frequency band for each energy

bin of $\Psi(E,t)$.

$$\phi(E_j,f) = \tan^{-1}\Big(\frac{R\times\Im\big(\tilde{\Psi}(E_j,f)\big)}{1+R\times\Re\big(\tilde{\Psi}(E_j,f)\big)}\Big), \quad \text{and} \quad T(E_j) = \text{mean}\Big(\frac{\phi(E_j,f)}{2\pi f}\Big). \tag{4.8}$$

Here, $\tilde{\Psi}(E_j,f) = \int_0^\infty \Psi(E_j,t)e^{-i2\pi ft}dt$ and $\Psi(E_j,t)$ is normalised, such the energy where the line peaks, E_0, is $\int \Psi(E_0,t)dt = 1$ (Cackett et al., 2014). $T(E_j)$ is the energy-dependent lag averaged over the chosen frequency band. We perform zero-padding when calculating the Discrete Fourier Transform to increase the frequency resolution of the transform by adding 0s at the end of the time vector - leading to a more closely sampled Fourier frequency vector.

Frequency Dependence of Lags

We calculate the lag-frequency spectra of the super-Eddington accretion and thin disks using Eq. 4.7 and show the results in Fig. 4.6. The x-axis, the Fourier frequency f, corresponds to the emissions with characteristic time delays shorter than $t = 1/2f$. Therefore, the low frequencies probe all reflected emissions, while the high frequencies only probe emissions with the shortest time delays. The y-axis, the lag, indicates the average time delay of photons. The lag stays constant at very low frequencies until a frequency $f_o \approx 1/2t_{\rm max}$, where $t_{\rm max}$ is the maximum time delay between the direct coronal and reflected photons as seen by a faraway observer. As frequencies increase above f_0, the photons with longer time delays are gradually phase-wrapped out. Therefore, the average time delay and the overall lag decrease with increasing frequencies. This trend lasts until the phase wraps completely and the lags turn negative, which is also known as the first zero lag crossing (see Uttley et al., 2014, Section 4 for a more detailed description). Beyond the first zero lag crossing, the lags become negative and then have a few oscillations at higher frequencies due to an artefact from Fourier analysis (Cackett et al., 2014; Uttley et al., 2014).

We compare the lag-frequency spectra produced from the super-Eddington and thin disk structures in Fig. 4.6a. The most prominent difference is that the lags of the super-Eddington disks change abruptly from being nearly constant to rapidly decaying, whereas the thin disk lags decay more gradually. This is because for super-Eddington disks, as shown in Fig. 4.4a to 4.4d, photons being reflected by the narrow funnel have a very short time delay within $t_{\rm max} = \text{few}\times 10R_g/c$. Therefore, we have $f_0 \approx 1/2t_{\rm max} \approx 1/(\text{few}\times 10\ \text{R}_\text{g}/\text{c}) \approx\ \text{few}\times 10^{-2}\ \text{c}/\text{R}_\text{g}$. For the thin disks, $t_{\rm max}$ depends on the inclination and the outer radius of the disk. Since we set the disks with a radius of $1000R_g$, their phase wrapping starts from $f_o \approx 1/(\text{few}\times 1000\ \text{R}_\text{g}/\text{c}) \sim \text{few}\times 10^{-4}\ \text{c}/\text{R}_\text{g}$. The rate of lag decay reflects how concentrated the photon time delays are. The super-Eddington cases have a compact 1d response function, $\Psi(t)$, so their frequency-dependent lags have a sharp drop at f_0. The thin disks, however, have more gradually decreasing lags because their 1d response functions have a large spread. The

fine structure of the lag spectra, such as the faster decay around few $\times 10^{-2}$ c/R$_g$ for thin disks, indicate that most photons can travel to the observer within few $\times 10R_g/c$.

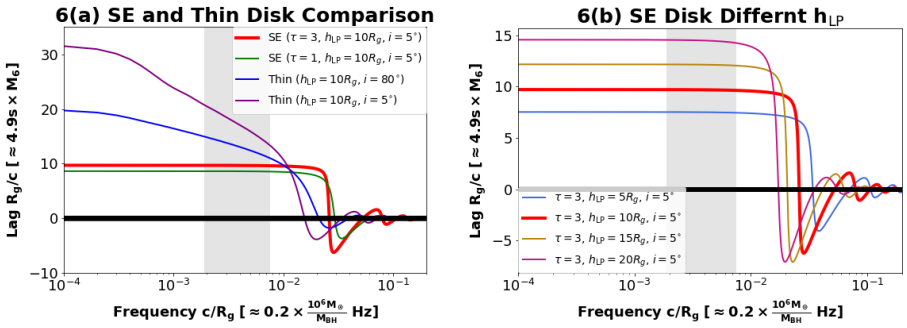

Figure 4.6: Lag-frequency spectra: The frequency and time units are expressed in natural units. The BH spin is $a = 0.8$, and the reflection surface is cut at $R_{\rm out} = 1000R_g$ in all cases. The shaded region is the low-frequency band used to calculate the energy-dependent lags in Section 4.3.2. **6a:** Comparison between SE and thin disk cases (see labels for the configurations). $h_{\rm LP}$ is fixed at $10R_g$. **6b:** Comparison between different $h_{\rm LP}$ for the SE disk.

The first zero lag crossing (at frequency $f_{\rm zl}$) is roughly set by the peak of $\Psi(t)$. A lower $f_{\rm zl}$ indicates more photons return at a later time. Therefore, we can see in Fig. 4.6b that increasing $h_{\rm LP}$ leads to longer lags as well as lower $f_{\rm zl}$. We can approximate $f_{\rm zl} \propto c/(4h_{\rm LP})$. One might notice that if we plot the frequency-dependent lag spectrum in physical units, then $h_{\rm LP}$ and $M_{\rm BH}$ are somewhat degenerate since increasing $M_{\rm BH}$ will also linearly increase the physical time lags and decrease the frequency of $f_{\rm zl}$. However, this degeneracy can be broken by calculating the energy-dependent lags, which we will show in Section 4.3.2.

It is worth noting that Wilkins (2013) have shown that if the corona has any physical extent, the frequency-lag decay will become even smoother for thin disks, which might also apply to the super-Eddington case. Also, as discussed above, the very slow decay of the thin disk lag-frequency spectra from constant lags to f_{zl} results from using the standard α-disk model with no vertical dimension. As a comparison, Taylor & Reynolds (2018b) have performed X-ray reverberation studies using realistic thin disk models with geometric thickness. They have found that as the disk becomes thicker as a result of increasing accretion rate, the disk lag-frequency spectrum decays at a faster rate, which is qualitatively consistent with our results. Therefore, we expect that the lag-frequency spectrum evolves from a slow decline to very sharp decay as the accretion rate increases from just below the Eddington accretion rate to the super-Eddington accretion rate.

Energy Dependence of Lags

In this subsection, we investigate the energy dependence of the Fe K lags. The lag-energy spectrum depends on the frequency band used to carry out the calculations

in Eq. 4.8. Throughout this section, we mainly assume the frequency band $\Delta f_{\rm XMM} = (0.9-3.6)\times10^{-4}Hz = (1.9-7.6)\times10^{-3}\left(M_{\rm BH}/(5\times10^6 M_\odot)\right)\, c/R_g$, which is a typical low-frequency range used in observational analysis (e.g., Kara et al., 2014). For our fiducial $M_{\rm BH} = 5\times10^6 M_\odot$, this frequency band is marked as the shaded grey region in Fig. 4.6, where it can be seen that in this frequency range the lag-frequency spectrum is still in the main decay phase.

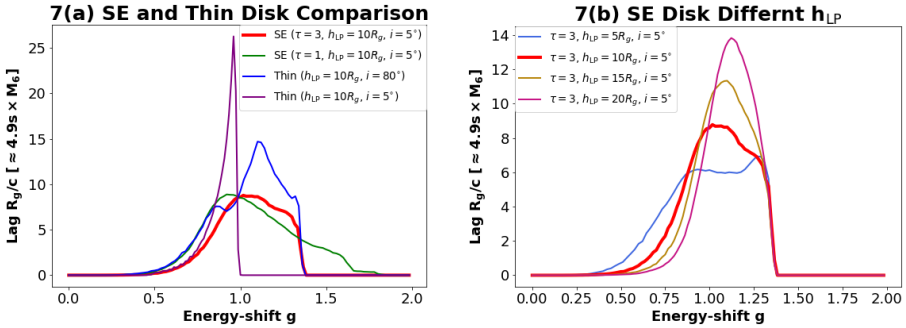

Figure 4.7: Lag-energy spectra in the observed frequency band $\Delta f_{\rm XMM} = (0.9-3.6)\times10^{-4}Hz = (1.9-7.6)\times10^{-3}c/R_g$. **7a:** Comparison between the SE disk and thin disk cases (see legends). **7b:** Comparison between different $L_{\rm LP}$ for the SE disk.

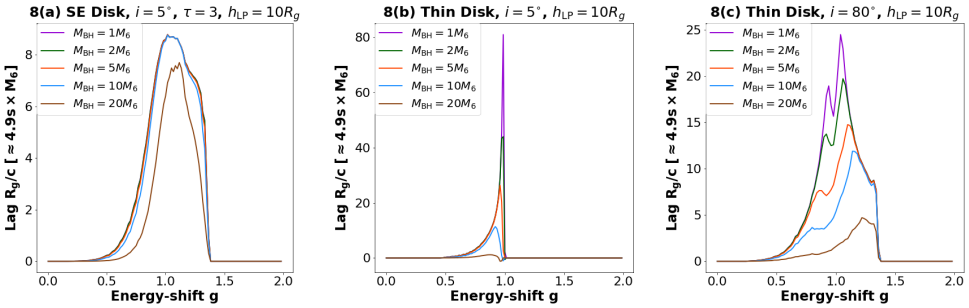

Figure 4.8: We show how the lag-energy spectrum changes with the BH mass in the frequency band $\Delta f_{\rm XMM} = (0.9-3.6)\times10^{-4}$ Hz, for a few representative $M_{\rm BH} = (1,2,5,10,20)\times M_6$, where $M_6 = 10^6 M_\odot$. Note that we show the lags in units of R_g/c, so its magnitude in physical units should be multiplied with $M_{\rm BH}$. **8a:** For the SE disk, the profile of the lag-energy spectrum remains almost constant as the $M_{\rm BH}$ increases all the way up to $2\times10^7 M_\odot$. **8b & 8c:** For a thin disk, its lag-energy profile changes substantially with $M_{\rm BH}$. Also the lag magnitude does not exactly scale linearly with $M_{\rm BH}$.

We first compare the lag-energy spectra produced from thin and super-Eddington disks in Fig. 4.7a. It has been shown previously that for thin disks, the shape of the Fe K lag-energy spectrum roughly mimics that of the Fe K line spectrum (Kara et al., 2013; Cackett et al., 2014). Here we find that the same holds for the super-Eddington case. The lag-energy spectra from super-Eddington disks are more blueshifted than their thin disk counterparts and generally have less skewed profiles. For the high-inclination thin disk case, the lag-energy spectrum is even more skewed to the right than its spectral counterpart, as seen in Fig. 4.4f. This is caused by photons with the longest time delays

(which have energies of $g \approx 1$ as seen Fig. 4.5) have been omitted due to the onset of phase-wrapping. In Fig. 4.7a and 4.7b, we also vary the τ surface or the coronal height for the super-Eddington disk case. One can see that despite the variance in these parameters, the lag-energy spectrum of the super-Eddington case stays largely blueshifted and relatively symmetric in shape. We also find that the profile of the lag-energy spectrum from the super-Eddington geometry is quite sensitive to the lamppost height. By lowering the coronal height, the irradiation of the inner disk increases, which introduces more gravitational redshift to the lag-energy spectrum and broadens the overall profile.

Next, we investigate how the lag-energy spectrum depends on the BH mass. Here we assume that all super-Eddington disks, regardless of their $M_{\rm BH}$ or other parameters, all have the same reflection geometry as the one we use. As shown in Fig. 4.6, the frequency band in natural units is correlated with the BH mass as $f = c/R_g \propto 1/M_{\rm BH}$. Therefore, increasing $M_{\rm BH}$ equivalently shifts the chosen frequency band closer to the first zero lag crossing, and its effect on the lag-energy spectrum is shown in Fig. 4.8. Overall, for the super-Eddington disk (Fig. 4.8a), the shape of the lag-energy spectrum is almost independent of $M_{\rm BH}$, especially for $M_{\rm BH} \lesssim 10^7 M_\odot$. The reason is that for this $M_{\rm BH}$ range, we are sampling from the almost constant part of the lag-frequency spectrum at frequencies lower than $f_{\rm zl}$. Only for the largest $M_{\rm BH} = 2 \times 10^7 M_\odot$, the lag-energy profile becomes slightly narrower. This is a result of the frequency range starting to approach the first zero lag crossing with increasing $M_{\rm BH}$, so the photons with the longest time delays are phase-wrapped out, which come from either the base of the funnel with long Shapiro time delays and the largest redshift or the outermost reflection surface with the longest travel paths and the largest blueshift. As a comparison, the shapes of the lag-energy spectra of thin disks change substantially with $M_{\rm BH}$ (Fig. 4.8c and 4.8b) because the onset of phase-wrapping occurs at very low frequencies for thin disks. For a low-inclination thin disk, the photons with the longest time delays come from the edge of the disk where the energy shifts are minimal and $g \approx 1$. Therefore, as $M_{\rm BH}$ increases, the central peak component at $g \approx 1$ decreases. For a high-inclination thin disk, the photons with the longest time delays come from the outer disk opposite the observer. Therefore, as $M_{\rm BH}$ increases, the lag-energy spectrum transits from a more Newtonian-like double horn profile to a more relativistically skewed and broadened profile. Another important difference is that the magnitude of the lag (in units of R_g/c) remains constant in the super-Eddington case, while that of a thin disk can vary with $M_{\rm BH}$. For example, for the high inclination thin disk, the lags (in units of R_g/c) decrease by a factor of 5 as the $M_{\rm BH}$ increases from $10^6 M_\odot$ to $2 \times 10^7 M_\odot$.

Last, we show how the lag-energy spectrum depends on the exact frequency band in Fig. 4.9. The possible frequency bands for data analysis are usually set by the telescope's cadence and the object's brightness. Here we choose 4 narrow frequency bands. The first two narrow frequency bands adopted are $\Delta f_1 = (0.8 - 1.6) \times 10^{-4}$ Hz and $\Delta f_2 = (1.6 - 3.2) \times 10^{-4}$ Hz, which are also inspired by the observations such as Kara et al. (2014) (solid and dotted blue lines in Fig. 4.9). The last two high-frequency bands

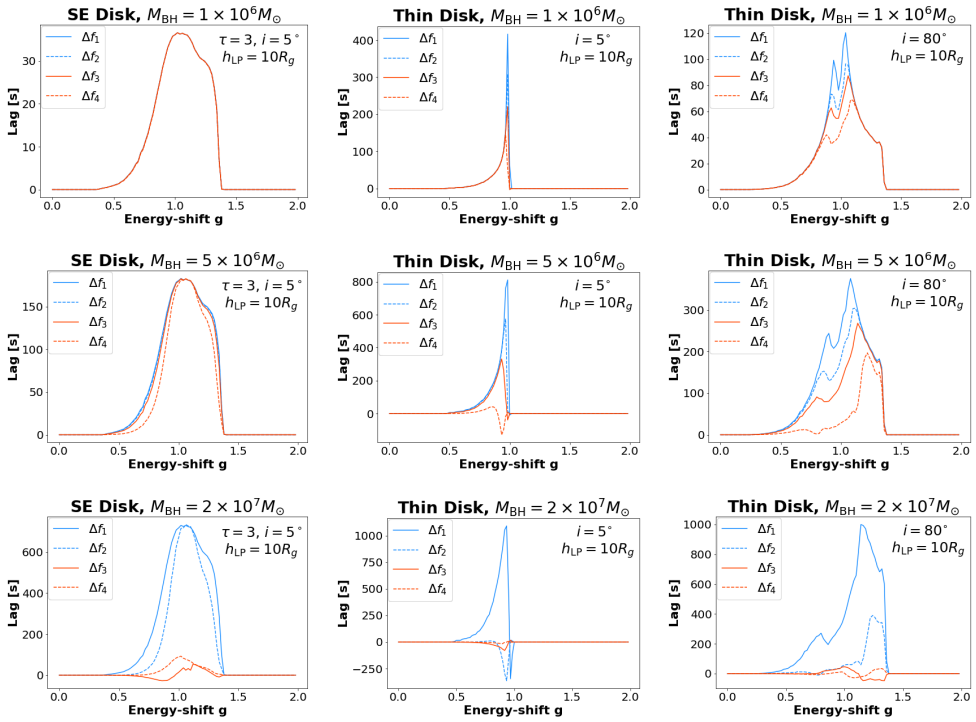

Figure 4.9: We show explicitly how the lag-energy spectrum depends on the exact frequency band. Here we use narrower frequency bands. The blue solid/dotted curves represent the narrow low-frequency bands of $\mathbf{\Delta f_1} = (0.8 - 1.6) \times 10^{-4} Hz = (0.34 - 0.67) \times 10^{-3} M_6\ c/R_g$ and $\mathbf{\Delta f_2} = (1.6 - 3.2) \times 10^{-4} Hz = (0.67 - 1.34) \times 10^{-3} M_6\ c/R_g$, where $M_6 = M_{BH}/10^6 M_\odot$. The red solid/dotted curves are for the narrow high-frequency bands $\mathbf{\Delta f_3} = (2 - 6) \times 10^{-4} Hz = (0.84 - 2.52) \times 10^{-3} M_6\ c/R_g$ and $\mathbf{\Delta f_4} = (6 - 10) \times 10^{-4} Hz = (2.52 - 4.20) \times 10^{-3} M_6\ c/R_g$. The three columns (left to right) represent different disk configurations: a) the SE disk, b) a low-inclination thin disk, and c) a high-inclination thin disk. Each row has a different $M_{BH} = (1, 5, 20) \times 10^6 M_\odot$. The most notable distinction between the two disk geometries is that the lag-energy spectrum of the SE disk remains almost the same despite the change in the frequency band until M_{BH} becomes sufficiently large.

are $\Delta f_3 = (2 - 6) \times 10^{-4}$ Hz and $\Delta f_4 = (6 - 10) \times 10^{-4}$ Hz, which arise from splitting the observed frequency band of Swift J1644 (Kara et al., 2016b) into two (solid and dotted red lines). The three columns in Fig. 4.9 represent the different disk configurations: the super-Eddington disk, a low inclination thin disk and a high inclination thin disk. The three rows represent different $M_{BH} = (1, 5, 20) \times 10^6 M_\odot$. Here we see the scenario is similar to when we change M_{BH}. For the super-Eddington disk, the shape of the lag-energy spectrum is almost the same for the four chosen frequency bands as long as $M_{BH} < 2 \times 10^7 M_\odot$. On the contrary, the thin disks have their lag-energy spectra varying with all frequency bands. Therefore, we propose that if the lag-energy spectrum of the Fe K line remains constant between two close, narrow frequency bands, it means the 1d response function is very compact, which is a sign of a narrow funnel reflection. The exact change in the lag-energy profile we expect to see between the two narrow

frequency bands depends on the $M_{\rm BH}$, $h_{\rm LP}$, frequency band, inclination angle, etc. To be conservative, for the $M_{\rm BH}$ and frequency bands range in Fig. 4.9, if we see less than a 5-10% difference in the lag magnitude and no morphological change in the lag profile between two narrow frequency bands, it is likely a super-Eddington accreting source.

4.4 Application onto the Super-Eddington TDE Swift J1644

In this section, we model the observed X-ray reverberation lags of the jetted TDE Swift J1644. Using the 25ks XMM-Newton observation over multiple energy bands from 0.3 to 10 keV, Kara et al. (2016b) discovered that the jetted TDE showed signs of a strongly blueshifted Fe K line. Furthermore, they found that the 5.5-8 keV band lagged around 100s behind the continuum-dominated regions at 4-5 keV and 9-13 keV in the galaxy's rest-frame frequency band ($\Delta f_{\rm swift} = (2-10)\times10^{-4}(1+z)$ Hz with the host galaxy at redshift $z = 0.354$), and in the 5.5-8 keV band an energy-dependent Fe K lag was preferred over a constant lag with $>$ 99.9% confidence interval. The observed lag-energy spectrum was consistent with a largely blueshifted reflection component.

We apply our theoretical calculation of X-ray reverberation to model the observed lags of Swift J1644. We use a Markov Chain Monte Carlo (MCMC) module called *emcee* in Python (Foreman-Mackey et al., 2013) to draw random sets of parameters ($M_{\rm BH}, h_{\rm LP}, R$) and simultaneously fit the observed lag-energy spectrum and the observed lag-frequency spectrum (the latter is calculated between the continuum dominated energies at $(3-4)\times(1+z)$ keV and the reflection dominated energies at $(5-6)\times(1+z)$ keV for this study). This MCMC method, based on a Bayesian framework, calculates the log-likelihood function $-\chi^2/2$, where χ^2 is the chi-square. The best fit with parameters minimising the log-likelihood function is shown in Fig. 4.10, where we also show the 1D and 2D posterior probability distributions of the parameters using the Python package Corner (Foreman-Mackey, 2016) in Fig. 4.11. When performing the fitting routine, we vary the mass of the BH, $M_{\rm BH} = [10^5 - 10^8]\ M_\odot$, the height of the corona, $h_{\rm LP} = [5-100]\ R_g$, and the dilution factor, $R = [0.01, 2]$. For the super-Eddington disk, we assume the reflection surface always stays the same as our fiducial one, and the inclination angle is fixed at 5°. For the thin disk, we vary the inclination angle between $i = [35-80]^\circ$ to fit a blueshifted reflection component. The rest-frame energy of the Fe Kα line is tested for both 6.4 keV (usually assumed for thin disks) and 6.7 keV (expected for super-Eddington disks due to the high ionisation level).

The best fits for the super-Eddington disk model with Fe Kα rest-frame energies of 6.4 and 6.7 keV are shown in Fig. 4.10a and 4.10b respectively. We find that the super-Eddington disk model can simultaneously explain the observed energy and frequency-dependent Fe K lags, with a reduced chi-square of $\chi^2_\nu \approx 1.13$ (6.4 keV) and $\chi^2_\nu \approx 1.17$ (6.7 keV). However, the small difference in the value of χ^2_ν is not significant enough to choose one line energy over the other, which can also be seen from the small difference in Bayesian information criteria $\Delta{\rm BIC} \approx 0.51$, where ${\rm BIC} = \chi^2 - k\ln(n)$ and k is the number of model parameters and n the number of data points. For both line

energies, we obtain a rather narrow and similar posterior distribution around the most probable values for all the fitted parameters as seen in Fig. 4.11a and 4.11b. Namely, we can constrain the $M_{\rm BH}$ to be around 3-6 million solar masses, $h_{\rm LP}$ to be between 10-20 R_g above the BH and R to be around 0.5-0.6. (Note that the best fitting parameters shown in Fig. 4.10 are not the same as the most probable parameters given by the 50th percentile in Fig. 4.11 since the probability distributions are not symmetric.) The degeneracy existing between $M_{\rm BH}$ and $h_{\rm LP}$ discussed previously is reflected as the linear correlation in the $h_{\rm LP} - M_{\rm BH}$ panel. The low R value means that the flux of the reflection component is around 50-60% of the continuum flux in this energy range. We note that Kara et al. (2016b) used the calibrated correlation between the $M_{\rm BH}$ and lag time of Seyfert galaxies and estimated a $M_{\rm BH}$ value which is of the same order of magnitude but slightly smaller than the $M_{\rm BH}$ value we obtained. This discrepancy is consistent with our prediction that the scaling calibration between $M_{\rm BH}$ and lag time for the two disk geometries should not be the same since the super-Eddington funnel geometry produces a shorter lag compared to a thin disk for the same $M_{\rm BH}$ and $h_{\rm LP}$. However, other complications can also contribute to this discrepancy, e.g., R might not be constant over this energy range.

As a comparison, we also fit a standard thin disk and show the results in Fig. 4.10c and 4.10d. We see that a thin disk viewed at a large inclination ($i = 70^\circ$ and $i = 65^\circ$ for the two rest frame Fe line energies) can also fit the data with $\chi^2_\nu \approx 1.25$ for both. The thin disk models give a smaller $M_{\rm BH} = (2-4) \times 10^6 M_\odot$, a similar $h_{\rm LP} = 9 - 19 R_g$, and a slightly larger $R = 0.65 - 0.95$ as seen in Fig. 4.11c and 4.11d. The thin disk fits give BIC values larger by 2-3 (marginal significance), which means that the super-Eddington disk model is slightly preferred over the thin disk model. This large disk inclination angle may induce a problem when explaining the jet being aligned with the line of sight since it is usually believed that the orbital angular momentum of the innermost accretion disk, the jet direction, and the spin axis of the BH are aligned (Bardeen & Petterson, 1975; Stone & Loeb, 2012) (also see Section 4 and references therein of the review paper Dai et al., 2021).

We do not attempt to directly fit the Fe Kα spectral line profile observed in Swift J1644, given line flux above the continuum is weak. However, if we use the best-fit parameters obtained from fitting the lag spectra to calculate a line profile, then the thin disk Fe line would have a very small portion of the emission between the observed energies 7.5-8.5 keV (less than 20%) and almost none reaching 8.5 keV. The super-Eddington disk Fe line, on the other hand, has a higher portion of the spectra in the observed energy range ($\sim$ 30%) and can reach energies above 8.5 keV. The line profiles from both disk models, however, appear too broad compared to the observed line width. This could be due to factors such as: 1) Some regions along the photosphere are over/under ionised and should not contribute to the Fe line production. 2) For the super-Eddington disk geometry, the coronal photons can have multiple reflections in the funnel and multiple scatterings in the wind. Including the latter in the calculation can introduce additional time delays and energy shifts, which will change the fitting of

parameters. We plan to extend our calculations to include these components in future studies.

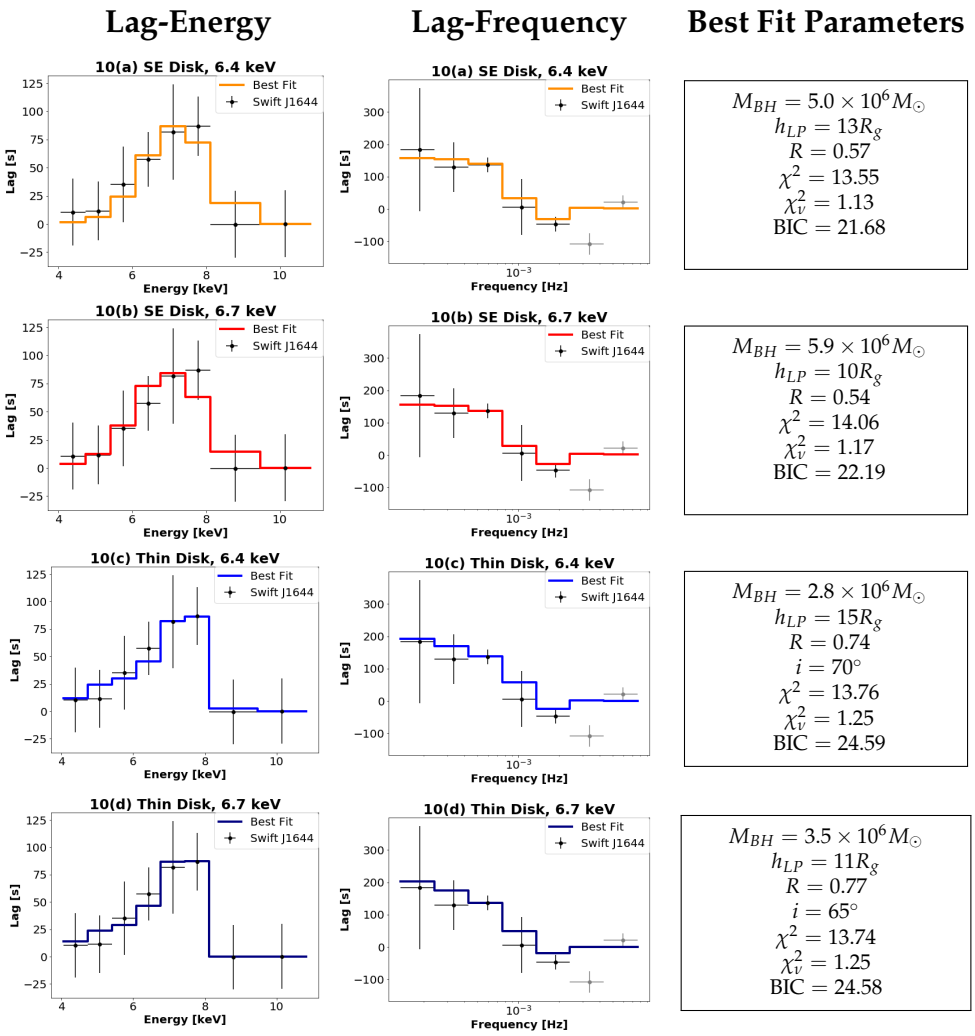

Figure 4.10: We apply the MCMC algorithm to obtain the best fit for the observed frequency, and energy-dependent lags of Swift J1644 using both the SE accretion disk model and thin disk model and assume the Fe K line has rest-frame energy of either 6.4 or 6.7 keV. We vary the mass of the BH ($M_{\rm BH} = [10^5 - 10^8]\ M_\odot$), the height of the corona ($h_{\rm LP} = [5 - 100]\ R_g$), and the dilution factor ($R = [0.01, 2]$). For the SE disk model, the observer inclination angle, i, is fixed at 5°, while for the thin disk model, i is an extra free parameter in the range of $[35° - 80°]$. The best-fit parameters are listed on the right side of each row together with the chi-square, reduced chi-square and BIC values. The Swift J1644 observed lag spectra are plotted as black dots with error bars, and the best-fit modelled lag spectra are plotted using coloured lines. All observational points are within 1σ from all model predictions except the last two high-frequency lag points in Fig. 9b (coloured grey). At these high frequencies, it is increasingly difficult to disentangle the lag contribution due to a loss of coherence (see Uttley et al., 2014, Section 2) and the Poisson Noise further reduce the S/N in this regime, so the two data points are not trustworthy. The best-fit parameters across all configurations indicate a black hole mass of $M_{\rm BH} = (2 - 6) \times 10^6 M_\odot$ with the lamppost corona located at $h_{\rm LP} = 10 - 15 R_g$ above the black hole. The SE models are slightly preferred over the thin disk models. Also, see Fig. 4.11 for the 1D and 2D probability functions of the MCMC fit, the most probable parameters and the uncertainty.

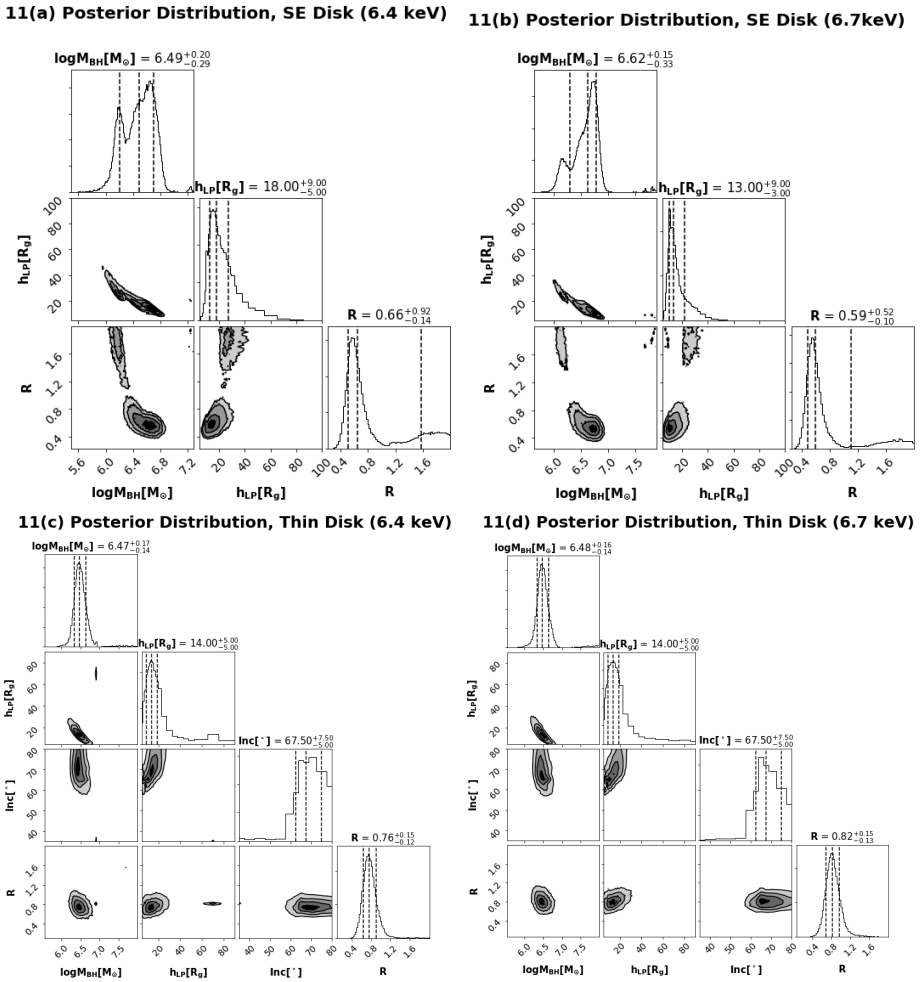

Figure 4.11: The 1d histograms located on the top of each column show the posterior distribution for each parameter from the MCMC algorithm. Note that the values shown are the most probable values of the parameters, which are different from best-fit parameters giving the lowest χ^2 presented in Fig. 4.10. The vertical dashed lines mark the 16th, 50th, and 84th percentile of probability. Also, for each parameter pair, we show the joint 2D histogram of the posterior distribution. The contours correspond to the 16th, 50th, and 84th percentile.

Lastly, we briefly mention that the observed isotropic X-ray luminosity of Swift J1644 at the peak is $L_X \approx 10^{47}$ erg s^{-1}, which is usually interpreted as the jet emission is highly beamed inside the relativistic jet. However, the low dilution factor obtained from our fits suggests that if the corona production is linked to the jet, then the base of the jet ($\sim 10R_g$) has not accelerated to a relativistic speed yet, consistent with the proposal in Kara et al. (2016b). We also note that there exists another theoretical explanation of the observed reverberation lag (Lu et al., 2017), where the corona is assumed to be far away from the BH ($\approx 100R_g$) and moving at relativistic speed together with the jet. Since we assume a stationary corona and do not include coronal multiple Compton scatterings in our model, we cannot test this hypothesis.

4.5 Summary and Discussions

In this study, we extend the technique of X-ray reverberation, which has been extensively used to probe geometrically thin accretion disks, to the regime of super-Eddington accretion. The main results are summarised below:

- The coronal photons are reflected inside a funnel surrounded by the optically thick wind launched by the super-Eddington accretion disk. As a result, the coronal emission and its reflection are visible only when the observer looks into the funnel. Due to the narrow funnel opening angle, the reflected photons have shorter lags compared to those from the thin disk geometry. Also, the Fe Kα fluorescent line induced by coronal irradiation has a large blueshift since the wind flows almost radially towards the observer with a terminal speed of few$\times 0.1c$.
- Another consequence of the narrow funnel geometry is that the frequency-dependent Fe K lag behaves almost like a step function near the first minimum (i.e., transiting from being constant at low frequencies to dropping abruptly). As a result, the shape of the energy-lag spectrum is independent of the $M_{\rm BH}$, while the magnitude of the lag scales linearly with the $M_{\rm BH}$.
- We propose that the funnel/wind reflection geometry produced in super-Eddington accretion systems can be identified using the following Fe Kα line characteristics: 1) In the lag-frequency spectrum: a drastic decrease from constant lag to the first minimum; 2) In the lag-energy spectrum: the spectrum profiles in two low-frequency, narrow bands remain almost the same; 3) In the spectral line / lag-energy spectrum: a large blueshift and less skewed profile, especially when the viewing angle can be independently constrained to be small.
- We have fitted the observed lag-frequency and lag-energy spectra of the jetted TDE Swift J1644 with our modelling. The MCMC fitting shows that the super-Eddington model fits the observed lag spectra slightly better than any of the thin disk configurations. The best fit using the super-Eddington model gives $M_{\rm BH} = (5-6)\times 10^6\ M_\odot$ and $h_{\rm LP} = 10-13\ R_g$.

In summary, this work shows that the X-ray reverberation lags produced from super-Eddington accretion flow have morphologically different signatures compared to thin accretion disk lags. Such signatures can be used to identify super-Eddington accretion systems around black holes. Furthermore, we have demonstrated that modelling the lag spectrum with a realistic super-Eddington disk structure is necessary for precisely constraining physical parameters from observations. In the future, we plan to explore further how X-ray reverberation signals can help us constrain the funnel geometry and wind acceleration profile, which are likely linked to the accretion rate and the BH spin. We also plan to carry out more detailed radiative transfer studies to include the multiple scattering of photons inside the super-Eddington funnel and the accretion flow. These theoretical studies, coupled with observations from current and next-generation X-ray instruments such as *Athena* and *XRISM*, will shed light on how

black holes grow at super-Eddington rates and give feedback to their host galaxies by launching powerful winds.

4.6 Acknowledgments

We are grateful to Javier García, Enrico Ramirez-Ruiz and Dan Wilkins for useful discussions. We also thank the anonymous referee for constructive comments. LT and LD acknowledge the support from the Hong Kong government through the GRF Grants (HKU17305920 and HKU27305119) and the HKU Seed Fund 104005595. Some of the simulations carried out for this project were performed on the HPC computing facilities offered by ITS at HKU and the Tianhe-2 supercluster. EK acknowledges support from NASA ADAP grant 80NSSC17K0515. CSR thanks the UK Science and Technology Facilities Council (STFC) for support under the Consolidated Grant ST/S000623/1, as well as the European Research Council for support under the European Union's Horizon 2020 research and innovation program (grant 834203).

Chapter 5

Dynamical Tidal Disruption Model

The content of this chapter is drawn from the published paper: "Dynamical Unification of Tidal Disruption Events" by Thomsen L. L., Kwan T. M., Dai L., Wu S. C., Roth N., Ramirez-Ruiz E., 2022, The Astrophysical Journal Letters, 937, L28. doi:10.3847/2041-8213/ac911f with minor consistency and grammar modifications. As the paper's first author, I performed post-processing simulations to calculate the TDE spectra, analysed the results and contributed to much of the paper writing.

The summary of the paper is as follows: The ∼100 tidal disruption events (TDEs) observed so far exhibit a wide range of emission properties both at peak and over their lifetimes. Some TDEs radiate predominantly at X-ray energies, while others radiate mainly at UV and optical wavelengths. While the peak luminosities across TDEs show distinct properties, the evolutionary behaviour can also vary between TDEs with similar peak emission properties. In particular, for optical TDEs, while their UV and optical emissions decline somewhat following the fallback pattern, some events can greatly brighten in X-rays at a late time. In this Letter, we conduct three-dimensional general relativistic radiation magnetohydrodynamics simulations of TDE accretion disks at varying accretion rates in the regime of super-Eddington accretion. We use Monte Carlo radiative transfer simulations to calculate the reprocessed spectra at various inclinations and evolutionary stages. We confirm the unified model proposed by Dai et al. (2018), which predicts that the observed emission largely depends on the viewing angle of the observer with respect to the disk orientation. Furthermore, we find that disks with higher accretion rates have elevated wind and disk densities, which increases the reprocessing of the high-energy radiation and thus generally augments the optical-to-X-ray flux ratio along a particular viewing angle. This implies that at later times, as the accretion level declines, we expect that more X-rays will leak out along intermediate viewing angles. Such a dynamical model for TDEs can provide a natural explanation for the diversity in the emission properties observed in TDEs at peak and along their temporal evolution.

5.1 Introduction

The tidal disruption of stars by massive black holes (MBHs) offers a unique probe of MBH demographics (Mockler et al., 2019b; Gezari, 2021), host galaxy properties (French et al., 2020), stellar dynamics (Pfister et al., 2020; Stone et al., 2020), and black hole accretion and jet physics (Dai et al., 2021). When a star with mass $m_\star$ and radius $r_\star$ approaches a MBH with mass $M_{\rm BH}$, the star is disrupted within the tidal radius $R_t \approx (M_{\rm BH}/m_\star)^{1/3} r_\star$, where the MBH's tidal force exceeds the stellar self-gravity. About half of the stellar debris orbits back to the vicinity of the MBH following a characteristic pattern that first quickly increases to a peak and then declines with time following a mass fallback rate $\dot{M}_{\rm fb} \approx t^{-5/3}$ (Rees, 1988; Evans & Kochanek, 1989; Guillochon & Ramirez-Ruiz, 2013). When $M_{\rm BH} \sim 10^6 M_\odot$, $\dot{M}_{\rm fb}$ can exceed the Eddington accretion rate by two orders of magnitude at peak and stays super-Eddington for years after the peak. Here we define the Eddington accretion rate of a black hole as $\dot{M}_{\rm Edd} = L_{\rm Edd}/(\eta_{\rm NT}\, c^2)$, where $L_{\rm edd} = 4\pi G M_{\rm BH} c/\kappa$ is the Eddington luminosity for an opacity κ, and $\eta_{\rm NT}$ is the nominal accretion efficiency for the Novikov-Thorne thin-disk solution (Novikov & Thorne, 1973).

With the recent launches of all-sky transient surveys, including ZTF and eROSITA, the number of detected tidal disruption event (TDE) candidates has reached around 100 (e.g., Gezari, 2021; Sazonov et al., 2021; Hammerstein et al., 2023). TDEs have been categorized into two classes based on their main emission type at peak: X-ray TDEs (Auchettl et al., 2017; Saxton et al., 2021) and optical TDEs (van Velzen et al., 2020). Most X-ray-selected TDEs emit soft X-rays with effective temperatures at $10^5 - 10^6$K, while only three of them emit beamed, hard X-rays that are associated with relativistic jets (e.g., Bloom et al., 2011; Burrows et al., 2011; Cenko et al., 2012; De Colle et al., 2012). In contrast, the optical TDEs have lower effective temperatures of a few$\times 10^4$K. Interestingly, as the luminosity of a TDE typically declines by around one order of magnitude over tens to hundreds of days after the peak, its effective temperature usually undergoes a peculiar non-evolution. Recently, a large number of TDEs have been followed up for longer than a year. Somewhat surprisingly, a few initially optically strong TDEs brighten in the X-rays so that their X-ray and UV/optical fluxes reach similar levels after about a year (e.g., Gezari et al., 2017; Holoien et al., 2018; Wevers et al., 2019; Hinkle et al., 2021; Liu et al., 2022).

Many theoretical models have been proposed to explain these TDE emission properties (Roth et al., 2020). While the X-ray emissions have been predicted by classical accretion disk models (Ulmer, 1999), UV/optical emissions are argued to be produced from either the reprocessing of X-ray photons in an extended envelope or outflows (Loeb & Ulmer, 1997; Strubbe & Quataert, 2009; Lodato & Rossi, 2011; Coughlin & Begelman, 2014; Guillochon et al., 2014; Metzger & Stone, 2016; Roth et al., 2016; Parkinson et al., 2020, 2022) or the shocks powered by debris stream self-intersection (Piran et al., 2015; Bonnerot & Stone, 2021). The late-time brightening of X-rays in TDEs can

be accounted for by either a change in the disk morphology as the accretion rate declines from super-Eddington to sub-Eddington or the delayed onset of accretion (van Velzen et al., 2019; Hayasaki & Jonker, 2021). The latter model, however, is disfavored by recent simulations showing that a large fraction of the debris already settles into a disk with moderate eccentricity within dynamical times for at least a subset of TDE parameters (Bonnerot & Stone, 2021; Andalman et al., 2022).

In search for a unified model that can explain both the optical and X-ray TDEs, Dai et al. (2018) have carried out the first three-dimensional (3D) general relativistic radiation magnetohydrodynamics (GRRMHD) simulation tailored for TDE super-Eddington accretion flow. The simulated disk, around a black hole with $M_{\rm BH} = 5 \times 10^6 M_\odot$ and spin parameter $a = 0.8$, has an accretion rate of $\dot{M}_{\rm acc} \sim 10\ \dot{M}_{\rm Edd}$, representing a typical accretion level in TDEs. The spectra of the disk have been obtained by post-processing the simulated disk with a novel radiative transfer code. It is found that the observed emission type largely depends on the viewing angle of the observer with respect to the disk orientation. When viewed face-on, X-ray emissions can escape from the optically thin funnel surrounded by winds. When viewed edge-on, X-ray emissions are heavily reprocessed in the geometrically and optically thick wind and disk, so only UV/optical emissions can be observed.

While this study gives a good first-order description of TDE disks and spectra, recent simulations also show that the properties of a super-Eddington disk depend on the accretion rate, the black hole mass and spin, and the magnetic flux threading the disk (Jiang et al., 2014, 2019; McKinney et al., 2015; Sądowski & Narayan, 2016). Although the black hole spin and disk magnetic flux might only mildly affect the main structure of the disk, they determine whether a relativistic jet can be launched (Blandford & Znajek, 1977; Curd & Narayan, 2019). At first glance, the black hole mass is not expected to affect the disk spectra significantly since most TDE host MBHs have masses in a narrow range $\approx 10^5 - 10^7\ M_\odot$. However, the peak fallback rate of the TDE debris sensitively depends on the black hole mass with the relation $\dot{M}_{\rm fb,peak}/\dot{M}_{\rm Edd} \propto M_{\rm BH}^{-3/2}$. Therefore, TDEs from smaller MBHs should, in general, have much higher accretion rates at peak than those from larger MBHs (Ramirez-Ruiz & Rosswog, 2009). In addition, further variances in the accretion rates of different TDEs can be introduced by the difference in the masses and ages of the disrupted stars (Law-Smith et al., 2020).

In this Letter, we investigate how the accretion rate at super-Eddington rates influences the TDE disk structure and the accompanied emission. We conduct three 3D GRRMHD simulations of super-Eddington disks with similar structures but varying accretion rates and post-process the simulated disks to obtain their spectra at different inclination angles. These simulations are useful for understanding the diversity of the emissions observed from different TDEs, as well as the evolution of single TDEs as their fallback and accretion rates decline after peak. In Section 5.2, we introduce the setup of the GRRMHD and radiative transfer simulations. In Section 5.3, we give the main results and compare them with TDE key observables. In Section 5.4, we draw a

summary and discuss the implications and future work.

5.2 Methodology

5.2.1 Disk Simulation Setup

We carry out 3D simulations of super-Eddington disks using the GRRMHD code HARMRAD with M1 closure (McKinney et al., 2014). In all simulations the MBH has $M_{\rm BH} = 10^6 M_\odot$ and $a = 0.8$. The radial grid has 128 cells spanning from $R_{\rm in} \approx 1.2R_g$ to $R_{\rm out} = 8500R_g$ ($R_g = GM_{\rm BH}/c^2$ is the gravitational radius of the MBH), with cell size increasing exponentially until $R_{\rm break} \approx 500R_g$ and then increasing hyper-exponentially. The θ-grid has 64 cells spanning from 0 to π with finer resolution in the jet and disk regions. The *phi* grid has 32 grids spanning uniformly from 0 to 2π with periodic boundary conditions. The gas is assumed to have solar chemical abundances (mass fractions of H, He, and "metals", respectively, $X = 0.7, Y = 0.28, Z = 0.02$). Frequency-mean absorption and emission opacities are used as in McKinney et al. (2015), except that the Chianti opacity is removed, as it is unimportant for the disk temperature of our TDE models. Thermal Comptonisation is also included.

We tailor the disk's initial conditions to be consistent with realistic TDE scenarios following the setup described in Dai et al. (2018). The accretion disk is initialized with Keplerian velocity profile with a rest-mass density that is Gaussian in z with a height-to-radius ratio of $H/R \approx 0.3$, so that the initial density profile is given by

$$\rho(r,z) = \rho_0 r^{-1.3} e^{-z^2/(2H^2)}, \tag{5.1}$$

where H is the scale height and ρ_0 is the initial reference density. The initial disks in the three simulations have masses varying in the range of a few$\times(0.1-1)\ M_\odot$. Adjusting ρ_0 leads to different accretion rates after the disk reaches the quasi-equilibrium state. As $\dot{M}_{\rm fb,peak}$ can reach $\approx 100\dot{M}_{\rm Edd}$ in a TDE around a $10^6 M_\odot$ black hole, and a large fraction of the debris mass is expected to escape in outflows, we set the aimed accretion rates to be a few to a few tens of $\dot{M}_{\rm Edd}$ (Table 5.1).

A large-scale poloidal magnetic field is initially seeded. As adopted in McKinney et al. (2015), for r smaller than a breaking radius $R_b = 500R_g$, the ϕ component of the vector potential is given by $A_\phi = MAX(r\ 10^{40} - 0.02, 0)(\sin\theta)^5$. For $r \geq R_b$, the field transitions to a split monopolar field, which is given by $A_\phi = MAX(R_b\ 10^{40} - 0.02, 0)(\sin\theta)^{1+4(R_b/r)}$. The field is normalised so that the initial ratio of gas+radiation pressure to magnetic pressure $\beta \equiv (p_{\rm gas} + p_{\rm rad})/p_b$ has a minimum value of 10.

5.2.2 Radiative Transfer Setup

We use the Monte Carlo radiative transfer code, Sedona (Kasen et al., 2006), to post-process the simulated disks and calculate the escaping radiation. More specifically, we calculate the bound electron level populations under non-local thermal equilibrium

(non-LTE) as in Roth et al. (2016) and the Comptonisation of electrons as in Roth & Kasen (2018). We track the free–free interactions, as well as the bound–bound and bound–free interactions. The bound–bound cross sections are obtained from the atomic database `CMFGEN`, and the bound–free cross sections are calculated using the hydrogenic approximation

$$\sigma_{\rm bf}(\nu, n_{\rm pq}, Z) = \begin{cases} \sigma_0 n_{\rm pq}/Z^2\ (\nu/\nu_{\rm tresh})^{-3}, & \text{if } \nu > \nu_{\rm thresh}. \\ 0, & \text{otherwise.} \end{cases} \tag{5.2}$$

Here $\sigma_0 = 6.3 \times 10^{-18}{\rm cm}^2$, $n_{\rm pq}$ is the principal quantum number, Z is the nuclear charge of the ion, ν is the photon frequency, and $\nu_{\rm tresh}$ is the ionisation threshold frequency set by the binding energy of the (least) bound electron. The gas is assumed to consist of only H, He, and O with solar abundances. For the radiative transfer calculations in this work, we focus on calculating the spectral energy distribution (SED) and leave the line modelling to a future study requiring higher-frequency resolution to accurately resolve the intrinsic narrow line width.

For each accretion rate, we calculate the spectra for four inclination bins at $\theta_{\rm bin} = 10^\circ, 30^\circ, 50^\circ$ and 70°. For each bin, we calculate the 1D-averaged density, velocity, and temperature profiles by using the time and ϕ- averaged profiles obtained in the GRRMHD simulations over $\theta_{\rm bin} \pm 5^\circ$. Since the simulated jet density is likely numerically boosted, for the bins at $\theta_{\rm bin} = 10^\circ$ and 30° we also reduce the jet density by 100 times before taking the average. We note that the first-order behaviour of the spectra does not depend on this arbitrary choice of density rescaling inside the jet. We set the source to be a blackbody spectrum with a single temperature of 10^6K, which is consistent with the inner disk temperature. The source photons are injected from an inner boundary set at the border between the inflow and outflow, which is typically at a few R_g except for the bin at $\theta_{\rm bin} = 70^\circ$, which is partly in the disk inflow region. For the latter, we place the inner boundary at $R = 20R_g$ instead and always set the gas velocity to zero. The photons are then propagated in 3D by assuming that the gas density, temperature, and radial velocity profiles are spherically symmetric. The photons propagate outward until they leave the computational domain set at $R = 4000R_g$ or have become a part of the kinetic/thermal pool. The total masses of the accretion flow in the regions we have used for post-processing ($i = 0^\circ - 75^\circ$) are 0.012, 0.024, and 0.072 $M_\odot$ for the three simulations.

Based on the Monte Carlo calculations, we iterate the gas temperatures, gas ionisation state, bound electron states, and radiative transfer solution under the assumption of radiative equilibrium until a steady solution has been reached (after approximately 20 iterations). Since GRRMHD simulations show that the luminosities of super-Eddington disks are not always capped by $L_{\rm Edd}$, we also tweak the source photon luminosity and obtain the spectra under two limits – the escaped bolometric luminosity is either $L_{\rm bol} = L_{\rm Edd} \approx 10^{44}$ ergs^{-1} or $L_{\rm bol} = 0.1\ \dot{M}_{\rm acc}c^2 \approx (\dot{M}_{\rm acc}/\dot{M}_{\rm Edd})\ L_{\rm Edd}$.

Table 5.1: Black hole and accretion disk parameters

Model	$M_{\rm BH}$ $(M_\odot)$	a	$\dot{M}_{\rm acc}$ $(\dot{M}_{\rm Edd})$	$\dot{M}_w$ $[\dot{M}_{\rm Edd}]$	$L_{\rm RAD}$ $(L_{\rm Edd})$
M6a08-1	10^6	0.8	7	1.4	5.4
M6a08-2	10^6	0.8	12	4.5	3.3
M6a08-3	10^6	0.8	24	14	8.1

5.3 Results

5.3.1 Properties of the Accretion Flow

In all three GRRMHD simulations, it takes an initial time period of $t =$ few $\times\, 1000R_g/c$ for the accretion flow to get established. As the disk evolves, magnetic fluxes accumulate near the MBH, and their strength further grows via the magnetorotational instability (MRI; Balbus & Hawley, 1991). Here we focus on the final stage of the simulations when the accretion flow has reached a steady state, and the wind has established equilibrium at most inclination angles. The black hole parameters and some basic quantities of the accretion disks averaged over the period of $t = (15,000 - 20,000)R_g/c$, are listed in Table 5.1. The disk profiles used for post-processing are also first ϕ-averaged and then time-averaged over the same period. More numerical details of the simulated disks are given in Appendix C.1.

The averaged accretion rates onto the event horizon of the MBH in these three simulations are $\dot{M}_{\rm acc} \approx 7$, 12 and 24 $\dot{M}_{\rm Edd}$. To first order, these super-Eddington accretion flows have similar structures to those described in Dai et al. (2018). As shown in the top panels of Fig. 5.1, geometrically and optically thick disks are formed with half-angular thickness $H/R \approx 0.20 - 0.25$, with, as expected, higher gas density toward the equatorial plane. The disks have achieved quasi-equilibrium for the inner $(200 - 300)R_g$ region. The rotation profile of the resultant thick disks is sub-Keplerian. Wide-angle winds are launched by the large radiation and magnetic pressure, which are also optically thick at most angles except close to the polar axis. There are roughly two components of the wind: an ultra-fast outflow (UFO) with speeds faster than $0.1c$ within $\lesssim 45^\circ$ from the pole, and a slower but denser wind outside $\gtrsim 45^\circ$ inclination. At larger accretion rates, the disk and wind densities increase, and the winds become slower as a result of mass loading. However, the wind geometry stays fairly similar.

The emission properties of the accretion flow should be examined near the photosphere. The optical depth for an opacity κ is calculated using $\tau(r) = \int \rho\kappa dl$ along the radial direction, r, from the outer boundary $R_{\rm out} = 8500R_g$ toward the event horizon. (Here relativistic effects are included so that $dl = -f_\gamma dr$, with $f_\gamma \approx u^t(1 - v/c)$ and $v/c \approx 1 - 1/(u^t)^2$). The electron-scattering photosphere is defined by $\tau_{\rm es}(r) = 1$ with $\kappa = \kappa_{\rm es} \approx 0.2(1 + X)$ cm^2 g^{-1}. The effective photosphere is defined as the outermost surface where photons are unlikely to undergo significant changes in their energy due to free-free, bound-bound, or bound-free opacities. Instead, they scatter towards the

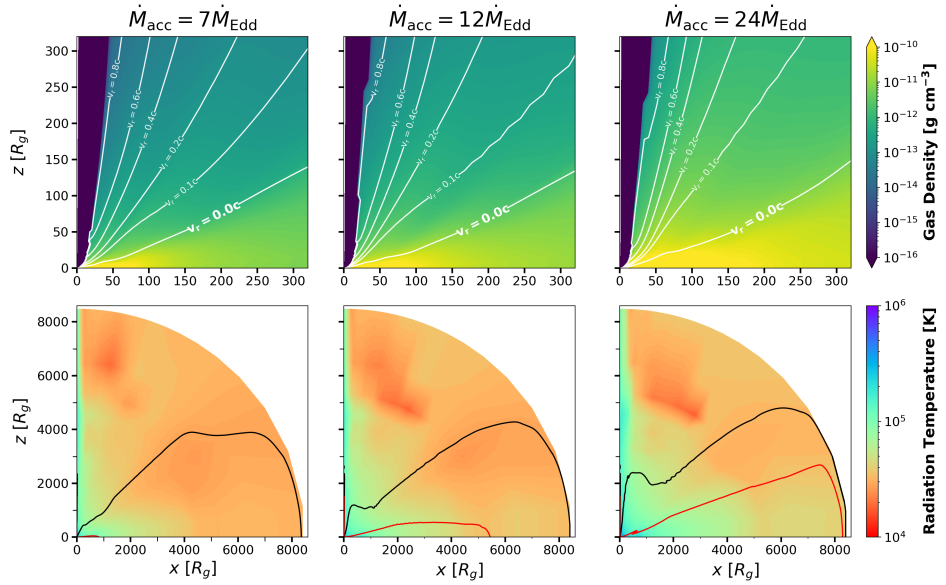

Figure 5.1: The 2D vertical profiles of time and ϕ-averaged gas rest-mass density ρ_0 (top panels, zoomed into the inner regions) and radiation temperature $T_{\rm RAD}$ (bottom panels, whole range of the simulation box). Three rows corresponding to three runs with different accretion rates (from left to right: $\dot{M}_{\rm acc} = 7\dot{M}_{\rm Edd}$, $12\dot{M}_{\rm Edd}$ and $24\dot{M}_{\rm Edd}$) in the quasi-equilibrium state. In the top panels, we show the contours of constant lab-frame radial velocity ($v_r \equiv u^r/u^t$) as white lines and show the jet regions, where the electromagnetic energy is larger than the rest-mass energy of the gas, in dark blue. In the bottom panels, the black lines indicate the electron-scattering photosphere with $\tau_{\rm es} = 1$, and the red lines indicate the effective photosphere with $\tau_{\rm eff} = 1$. Larger accretion rates induce larger disk/wind density and higher gas/radiation temperature, while the gas distribution and velocity structure remain rather robust against the variance in accretion rates. The sizes of photospheres generally increase as the accretion rate increases.

observer. Electron scattering plays a crucial role in establishing this surface by contributing to the gas becoming optically thick. This causes the photons to undergo a random walk, increasing the likelihood of free-free absorption as they escape the accretion flow through multiple electron scatterings in three-dimensional space. Therefore, the effective photosphere is given by $\tau_{\rm eff}(r) = 1$ with the effective opacity being $\kappa_{\rm eff} = \sqrt{3\kappa_{\rm ff}\kappa_{\rm total}} = \sqrt{3\kappa_{\rm ff}(\kappa_{\rm ff} + \kappa_{\rm es})}$. Here, we have only considered free-free opacity $\kappa_{\rm ff} \approx 3.82 \times 10^{22} Z(1+X)(1-Z)\rho T_g^{-3.5}$ in the scattering-dominated gas, where T_g is the gas temperature since it is dominating over the other opacities (McKinney et al., 2014). Both photospheres are plotted over the disk profiles in the bottom panels of Fig. 5.1. As expected, we see the presence of an optically thin "funnel" near the rotation axis where the wind density is correspondingly lower. The wind becomes more opaque as the accretion rate increases, reducing the funnel's angular size.

The effective photospheres reside mostly within $r \sim 5000R_g$ except along the equatorial direction for the disk with the largest $\dot{M}_{\rm acc}$. Therefore, we select to evaluate various physical quantities at $r = 5500R_g$. This gives averaged wind mass rates of $\dot{M}_w =$

1.4, 4.5 and 14 $\dot{M}_{\rm Edd}$, and averaged bolometric luminosities at $L_{\rm RAD}$= 5.4, 3.3 and 8.1 $L_{\rm Edd}$, respectively, for the three simulations. The radiation temperature of the accretion flow is also plotted, which varies from $\approx 10^6$ K near the black hole to $\approx 10^4$ K in the outer part of the disk and wind. The radiation flux varies with the inclination as shown in Dai et al. (2018) and leaks out through the region of least resistance, the funnel.

The accretion flow drags magnetic fluxes and accumulates near the MBH. The inner regions quickly enter the regime of magnetically arrested accretion disks (MADs; Narayan et al., 2003). Relativistic jets are launched magnetically in all simulations through the Blandford–Znajek mechanism (Blandford & Znajek, 1977). In this Letter, we focus on calculating the emission properties from the disk, and we leave the analysis of the jets for future study.

5.3.2 Spectra from Post-Processing

In this section, we investigate how the emission reprocessing depends on a few key parameters: the viewing angle, accretion rate, and luminosity. The dependence on viewing angle has been previously studied by Dai et al. (2018). They show that for a fixed accretion rate, there is a clear trend of the SED moving toward larger wavelengths with increasing inclination angles. At low inclinations, the gas density is lower, so X-rays produced from the inner disk easily escape. On the other hand, the optically thick wind and outer disk serve as an effective reprocessing envelope at relatively large inclinations. More specifically, in the fast wind region, the photons lose energy as they go through multiple scatterings in the expanding outflow before escaping. In the disk and the slow wind region, the reprocessing is mainly caused by the absorption of X-ray photons and the thermal Comptonisation of electrons.

We reexamine the emission viewing angle dependence in the three new simulated disks. Fig. 5.2a, 5.2b, and 5.2c show how the escaped spectrum varies with inclination, when $\dot{M}_{\rm acc} = 7, 12,$ and 24 $\dot{M}_{\rm Edd}$ respectively. The escaped spectra are calculated from the inclination bins at $i = 10^\circ$, 30°, 50°, 70°, with the first three bins residing in the wind and the last one at the boundary between the wind and disk. The properties of gas in these bins are set mainly by the winds launched from the inner disk that has achieved a quasi-equilibrium state and has specific angular momentum smaller than that of the disrupted star. At any of these accretion rates, the SED still evolves from X-ray to optically dominated as the inclination increases. However, the exact angle at which this transition occurs depends on the accretion rate. One can clearly observe that at low accretion rates $\approx$ few $\times$ $\dot{M}_{\rm Edd}$, the escaped emission is dominated by X-ray emission at most inclinations unless the inclination angle is substantial (e.g., $i \gtrsim 70^\circ$ for $\dot{M}_{\rm acc} = 7\ \dot{M}_{\rm Edd}$), while at very high accretion rates $\approx$ few $\times$ 10 $\dot{M}_{\rm Edd}$, the escaping radiation is mainly optically dominated except near the polar region (e.g., $i \lesssim 10^\circ$ for $\dot{M}_{\rm acc} = 24\ \dot{M}_{\rm Edd}$). For a more detailed discussion of the radiative transfer physics, see Appendix C.2.

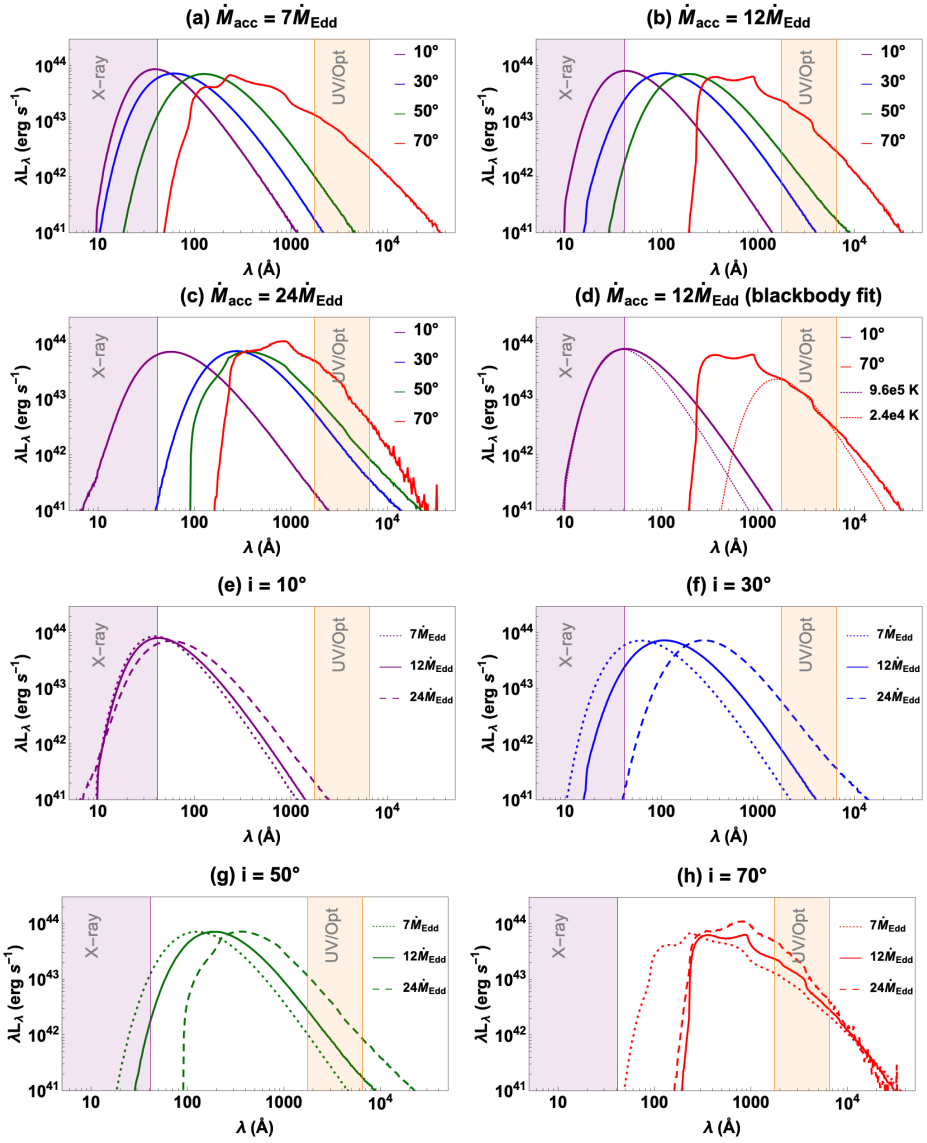

Figure 5.2: The simulated escaping spectra of the accretion disk at different accretion rates ($\dot{M}_{acc}$ = (7, 12, 24)$\dot{M}_{Edd}$) and inclinations ($i = 10°, 30°, 50°, 70°$). The bolometric luminosity of the spectra is assumed to be $L_{bol} = L_{Edd}$ for all spectra. The purple-shaded region indicates the X-ray band with an energy above 0.3 keV. The orange-shaded region corresponds to Swift UVOT band at 1700-6500 Å. Panel (a)–(c) show the spectral evolution with inclination angles at fixed accretion rate. All spectra change from X-ray strong to UV/optical strong as the inclination goes from the polar direction to the disk direction. Panel (d) is the same as panel (b) but only includes the spectrum at $i = 10°$ with a blackbody spectrum fitting its X-ray continuum component and the spectrum at 70° with another blackbody spectrum fitting its UV/optical continuum component. Panel (e)–(h) show the spectral evolution with accretion rates at fixed inclinations. Three types of evolution can happen as the accretion rate decreases: X-ray-strong at all times (small inclination), optical/UV strong at early times, and X-ray brightening at the late time (intermediate inclination), and optical/UV strong at all times (large inclination).

We expect a TDE to be observed along a fixed viewing angle during its entire evolution unless the disk experiences some axial precession. Therefore, we show the spectral evolution with $\dot{M}_{\rm acc}$ at fixed inclination angles in Fig. 5.2e–5.2h. As the accretion rate declines after the peak, the amount of reprocessing material is reduced, so the SED universally shifts toward shorter wavelengths. However, the exact behaviour of the spectrum depends sensitively on the inclination angle. At very small inclinations ($i = 10^\circ$), the TDE stays X-ray dominated throughout its evolution. At intermediate inclinations ($i = 30^\circ$ and 50°), the TDE can be optically strong at early times (if $\dot{M}_{\rm acc}$ can be sufficiently large) and then brightens at X-ray energies at a late time when the accretion rate diminishes. At very large inclinations ($i = 70^\circ$), the TDE stays UV/optically strong throughout its entire evolution.

While we have assumed that the bolometric luminosities of the escaped radiation are always close to $L_{\rm Edd}$ in the analysis above, GRRMHD simulations show that the escaped luminosity from super-Eddington disks can exceed the Eddington limit, with more flux leaking out through the funnel (e.g., Sądowski & Narayan, 2016). Therefore, we also calculated the spectra when the escaped radiation has a bolometric luminosity $L_{\rm bol} = 10\%\ \dot{M}_{\rm acc}c^2$, which are shown in Fig. C.2. When the reprocessing is driven by adiabatic expansion, the SED shape stays unchanged while the magnitude of the flux scales with the luminosity. When the reprocessing mechanism is driven by absorption and Comptonisation, increasing the luminosity makes the gas more ionised and reduces bound–free and free–free absorption, which shifts the spectral energy peak to slightly higher energies. However, the spectral shape is rather insensitive to luminosity. In general, the setting of the luminosity within the explored range does not alter how the escaped radiation depends on the viewing angle and accretion rate.

5.3.3 Comparison with Observations: Blackbody Luminosity, Temperature, and Photosphere Radius

In this section, we compare our model predictions to the observed properties of TDEs. We start from the TDE catalogue in Gezari (2021), which also lists the observed blackbody luminosities and temperatures, and then only include TDEs that have their masses estimated from the $M - \sigma$ relation as in Wong et al. (2022). This gives us 7 X-ray-selected TDEs (Table C.2) and 16 optically-selected TDEs (Table C.3). We plot their observed blackbody luminosities, effective temperatures and photosphere radii as functions of $M_{\rm BH}$ in Fig. 5.3a - 5.3c. The observed $L_{\rm BB}$ varies between $10^{-3} - 10\ L_{\rm Edd}$, and can exceed $L_{\rm Edd}$ when $M_{\rm BH} \lesssim 10^6 M_\odot$. Interestingly, $L_{\rm BB}$ commonly has a dependence on $M_{\rm BH}$ following the fallback rate trend: $\dot{M}_{\rm fb}/\dot{M}_{\rm Edd} \propto M_{\rm BH}^{-3/2}$. The observed $T_{\rm BB}$ clearly depends on whether the TDE is optically selected ($\approx$ few $\times\ 10^4$ K) or X-ray selected ($\approx\ 10^5 - 10^6$ K). The observed $R_{\rm BB}$, calculated from $L_{\rm BB}$ and $T_{\rm BB}$ using the Stefan–Boltzmann law, also has a bimodal distribution. The optically-selected TDEs have $R_{\rm BB}$ reaching $10^2 - 10^4 R_g$ and always exceeding both the circularisation radius

$R_{\rm circ} = 2R_t$ and the stream self-intersection radius $R_{\rm int}$ (Dai et al., 2015). The X-ray-selected TDEs, however, sometimes have $R_{\rm BB}$ even within the event horizon. This puzzling issue has also been noted by Yao et al. (2022), who propose a few possible causes, including: (1) the measured temperature being higher than the true temperature owning to Comptonisation effects and (2) the existence of some patch obscuring material that suppresses the X-ray flux without changing its spectral shape, though the nature of the material is uncertain. We point out that the large uncertainty in TDE host black hole mass estimates might also contribute to this issue.

As the observed properties of TDEs are usually inferred from their spectra in monochromatic bands, we also fit the simulated spectra in either the X-ray or UV/optical band with blackbody spectra. For example, in Fig. 5.2d we show the emergent spectra for $\dot{M}_{\rm acc} = 12\dot{M}_{\rm Edd}$ at $i = 10^\circ$ and 70° and the blackbody radiation fits to the spectra in the X-ray band (0.3–10 keV) or the part of the spectrum in the UV/optical band (the 170–650 nm Swift UVOT band). It can be seen that the X-ray and UV/optical emission can be individually well approximated by blackbody radiation. Similarly, for each spectrum (at $\dot{M}_{\rm acc} = (7, 12, 24)\ \dot{M}_{\rm Edd}$ and inclination $i = 10^\circ, 30^\circ, 50^\circ, 70^\circ$), we obtain two blackbody radiation fits in the X-ray band and the UV/optical band. The escaped bolometric luminosity is assumed to be varying between $L_{\rm Edd}$ and $0.1\%\ \dot{M}_{\rm acc}c^2$. The luminosities, temperatures, and radii of the best-fit blackbody radiation spectra are listed in Table C.4 and plotted in Fig. 5.3d - 5.3f (UV/optical fit) and Fig. 5.3g - 5.3i (X-ray fit). We further categorize whether a modelled TDE spectrum is an X-ray strong or optically strong by comparing the luminosity in the X-ray band (0.3-10 keV) and the blackbody luminosity inferred from the UV/optical band. We compare the model predictions to the observed properties below:

1. *Luminosity*: The modeled $L_{\rm BB}$ mostly lies between $0.01L_{\rm Edd}$ and a few $L_{\rm Edd}$. The simulated spectrum usually peaks in EUV and has a broader shape than a single-temperature blackbody spectrum. Therefore, the inferred blackbody luminosity ($L_{\rm O,BB}$ or $L_{\rm X,BB}$) is always smaller than the bolometric luminosity $L_{\rm bol}$ of the escaped radiation. $L_{\rm O,BB}/L_{\rm bol}$ for optically strong TDEs and $L_{\rm X,BB}/L_{\rm bol}$ for X-ray strong TDEs are typically a few$\times(1-10)\%$ (Fig. C.3). This naturally explains the missing energy problem in TDE (Stone & Metzger, 2016; Lu & Kumar, 2018; Mockler & Ramirez-Ruiz, 2021) – the majority of the energy is emitted in the EUV band, which is difficult to be detected.

2. *Temperature*: Our modelling reproduces the bimodal distribution of TDE temperatures, i.e., optically-strong TDEs have temperature $T_{\rm O,BB} \approx$ few $\times\ 10^4$K, and X-ray-strong TDEs have temperature $T_{\rm X,BB} \lesssim 10^6$K. Furthermore, our modelling shows that the inferred temperatures of optical TDEs are not highly sensitive to accretion rates or observer inclination, which explains why TDEs have relatively constant $T_{\rm BB}$ throughout the evolution (van Velzen et al., 2020).

3. *Photosphere radius*: The optically strong TDEs have far larger photosphere radii ($R_{\rm O,BB} \approx 10^2 R_g - 10^4 R_g$) than X-ray-strong TDEs ($R_{\rm X,BB} \approx$ few $\times\ R_g$). A

comparison between the observed $R_{\rm O,BB} = 10^3 - 10^4 R_g$ and the modelled $R_{\rm O,BB}$ suggests that optically selected TDEs either are commonly observed from large inclinations or have $L_{\rm bol} > L_{\rm Edd}$.

We note that our predictions for the X-ray quantities, particularly in the $i = 10^\circ$ bin, are sensitive to the setting of the radiative transfer calculations. Here we always inject a blackbody spectrum with a constant $T = 10^6$K, so our predicted $T_{\rm X,BB}$ at small inclinations also fall into a very narrow range.

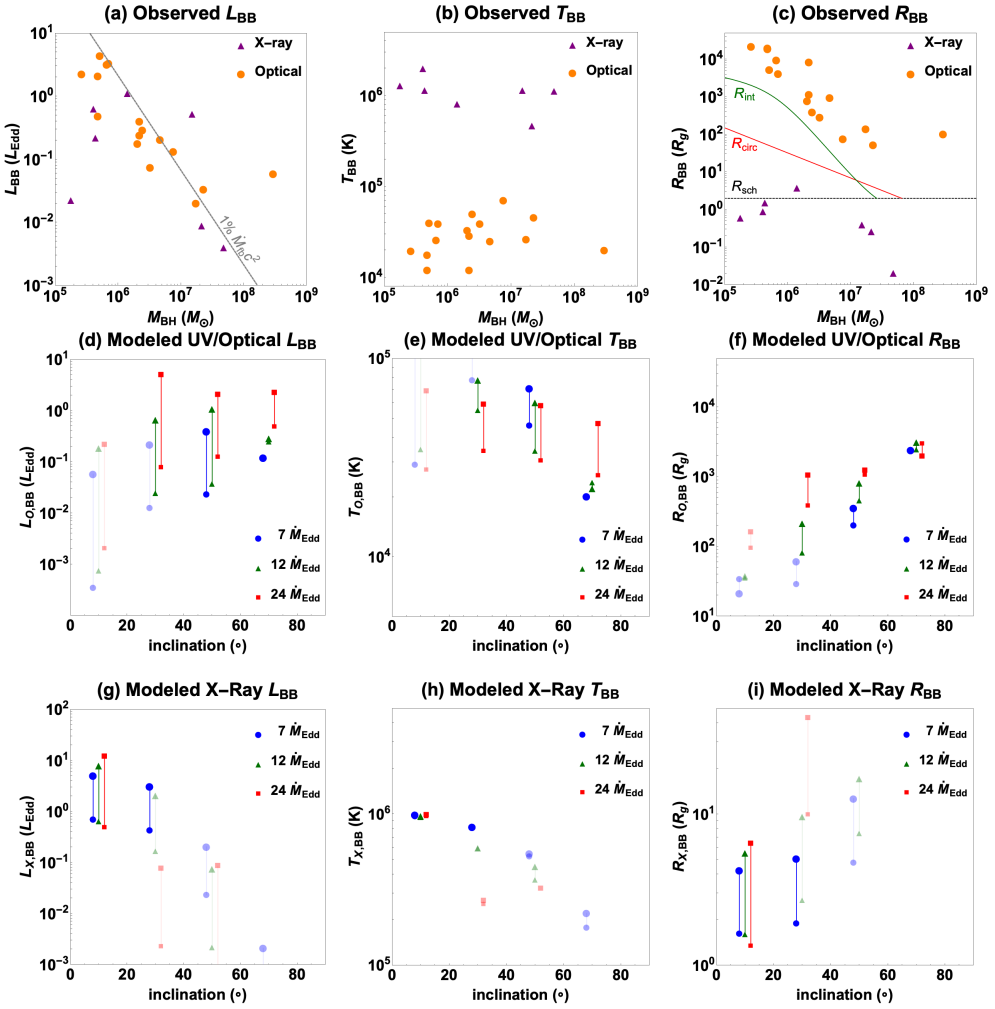

Figure 5.3: Comparison between the observed and modelled TDE blackbody luminosity, temperature and radius. Top row (a–c): The observed quantities vs. $M_{\rm BH}$ for 16 optically-selected TDEs (orange circles) and 7 X-ray-selected TDEs (purple triangles). (a) The observed $L_{\rm BB}/L_{\rm Edd}$ has a clear trend with $M_{\rm BH}$. A grey line showing $L = 1\%\ \dot{M}_{\rm fb}c^2$, with $\dot{M}_{\rm fb}$ being the fallback rate of a $0.1M_\odot$ star, is overplotted to guide the eye. (b) X-ray TDEs have temperatures of $10^5 - 10^6$K, and optical TDEs typically have lower temperatures of a few$\times 10^4$K. (c) Optical TDEs have $R_{\rm BB}$ larger than the circularisation radius (red curve) or the stream self-intersection radius (green curve) (both calculated using a $0.1M_\odot$ star). X-ray TDEs sometimes have $R_{\rm BB}$ smaller than the black hole Schwarzschild radius (black line). Middle row (d–f) and bottom row (g–i): The inferred quantities based on the blackbody radiation spectrum fitting the simulated spectra in the UV/optical band and X-ray band, respectively, vs inclination angle i. Different symbols are used to mark different accretion rates: $7\dot{M}_{\rm Edd}$ (blue circle), $12\dot{M}_{\rm Edd}$ (green triangle), and $24\dot{M}_{\rm Edd}$ (red square). Vertical lines connect the values calculated with an escaped luminosity of $L_{\rm bol} = L_{\rm Edd}$ (smaller symbol size) and $L_{\rm bol} = 10\%\dot{M}_{\rm acc}c^2$ (larger symbol size) to indicate possible ranges. In panels (d)-(f), TDEs with $L_{\rm O,BB} < L_{\rm X,0.3-10keV}$ are marked with lighter shaded symbols to indicate that they are less likely to be selected optically. Similarly, in panels (g)-(i), TDEs with $L_{\rm O,BB} > L_{\rm X,0.3-10keV}$ are marked with lighter-shaded symbols to indicate that they are less likely to be selected by X-ray instruments. The blackbody luminosity, temperature and radius inferred from our modelling to the first order reproduce the observed ones.

However, the temperatures at the centre of accretion disks generally increase with increasing $\dot{M}_{\rm acc}$ and decreasing $M_{\rm BH}$, which will induce more variance to the observed X-ray temperatures. In addition, for the setting with $L = L_{\rm Edd}$, the predicted $L_{\rm X,BB}$ decreases as $\dot{M}_{\rm acc}$ increases, as a result of a constant bolometric luminosity and more reprocessing from X-ray to UV/optical emissions at higher densities. However, simulations show that the radiation fluxes leaking through the funnel are not Eddington limited (McKinney et al., 2015; Dai et al., 2018). Therefore, we expect X-ray luminosities to scale positively with accretion rates, as illustrated by the $L = 0.1\ \dot{M}_{\rm acc}c^2$ case.

5.3.4 Temporal Evolution of TDE Continuum Emissions

We show in Fig. 5.4 the evolution of the modelled luminosity, temperature, radius, and the ratio of optical to X-ray luminosity as functions of the accretion rate. In order to connect the snapshots at a specific accretion rate to the temporal evolution of TDEs, we assume $\dot{M}_{\rm fb}(t) = \dot{M}_{\rm acc}(t) + \dot{M}_{\rm wind}(t)$. This assumption is valid only if the fallback timescale dominates over other timescales, such as the disk viscous timescale and the photon diffusion/advection timescale. The exact conversion from $\dot{M}_{\rm fb}$ to t depends on the mass of the MBH, the properties of the disrupted star, and the impact parameter (Law-Smith et al., 2020). Focusing on the post-peak evolution, the three disk simulations correspond to 45.9, 102.4, and 174 days after the peak of the flare, assuming that a solar-type star is fully disrupted by a $10^6 M_\odot$ black hole. Calculations of these timescales are given in Appendix C.6 to show that the fallback timescale dominates over the photon transport and disk viscous timescales.

As the accretion rate drops from $24\dot{M}_{\rm Edd}$ to $7\dot{M}_{\rm Edd}$, the optical luminosity also decreases, and the UV/optical light curve roughly follows the canonical $t^{-5/3}$ decay. As discussed in the previous section, the fitted blackbody temperature stays rather constant. Interestingly, at large inclinations, $T_{\rm O,BB}$ decreases slightly with declining $\dot{M}_{\rm acc}$, while at small to intermediate inclinations $T_{\rm O,BB}$ shows the opposite trend. This can provide an explanation for the differences in the observed evolution of $T_{\rm O,BB}$ (van Velzen et al., 2020). As a result, the photosphere radius shrinks as $\dot{M}_{\rm acc}$ decreases, with a faster evolution at smaller inclinations.

The ratio between UV/optical luminosity ($L_{\rm O,BB}$) and X-ray luminosity ($L_{\rm X,0.3-2keV}$) also decreases as the accretion level drops and the amount of obscuring material is reduced. The fastest $L_{\rm O,BB}/L_{\rm X,0.3-2keV}$ evolution is observed at intermediate inclinations, especially if the TDE has a high accretion rate at peak. In such cases, we expect to see strong X-ray brightening of initially optically strong TDEs, as found in ASASSN-15oi (Gezari et al., 2017). The X-ray luminosity reaches the same level as the UV/optical luminosity at $t \gtrsim 100$ days after the peak and possibly even later if the disk formation or viscous timescale is long. At very small inclinations, the event is always X-ray-strong. At very large inclinations, the event should stay optically strong for an extended period, although it is theoretically predicted that the disk should eventually become geometrically thin and emit mostly in X-rays/UV when the accretion level drops to around

Eddington (Shakura & Sunyaev, 1973).

While our model can qualitatively explain the evolution of most optical and X-ray TDEs, it cannot fully explain the evolution of ASASSN-14li, which produces almost equally bright in X-ray and UV/optical bands at peak and has $L_O/L_X \sim 1$ throughout the first year (Holoien et al., 2016b). The unique behaviour of ASASSN-14li could be related to the event happening in a host galaxy recently experiencing a merger and AGN activities (Prieto et al., 2016). Another possible explanation is that ASASSN-14li could be observed from a low inclination that gives a slower L_O/L_X evolution, but we are currently missing some UV/optical emissions observed at low inclinations owing to our 1D reprocessing setup, which is explained more in Section 5.4.

In addition, we can compare the mass of the gas used for post-processing in the three simulations to the accumulated mass of the fallen-back debris at the particular epochs corresponding to those accretion rates. Using the fallback rate from Evans & Kochanek (1989) and the black hole and stellar parameters as above, the total debris mass that has fallen back between the peak and 45.9/102.4/174 days after the peak is 0.11/0.18/0.23 $M_\odot$ respectively, which is much larger than the mass of the gas needed for reprocessing (0.012/0.024/0.072 $M_\odot$). It is worth mentioning that the effective mass used for the 1D post-processing can largely deviate from the true envelope mass due to the highly asymmetric structure and mass distribution of the 3D disk. As an example, the effective 1D envelope masses for the $\dot{M}_{\rm acc} = 12\dot{M}_{\rm Edd}$ simulations in four inclination bins are listed in Table C.5 to illustrate this effect.

5.4 Summary and Future Work

Inspired by the unified model for TDEs proposed by in Dai et al. (2018), we carry out three additional 3D GRRMHD simulations of TDE super-Eddington accretion flow at different Eddington ratios and conduct radiative transfer calculations to obtain the emanating spectra. Based on the results, we further propose a dynamical unified model that can explain the diversity and evolution of TDE continuum emissions:

- The viewing angle of the observer with respect to the orientation of the disk is the most important parameter in determining whether we observe either an X-ray or an optical bright TDE. At small inclinations, X-rays can escape from the funnel of the super-Eddington disk. At large inclinations, X-rays are mostly reprocessed into UV/optical radiation by the geometrically and optically thick wind and disk.
- The blackbody radiation fits of the TDE super-Eddington disk spectra produce colour temperature, blackbody luminosity, and photosphere radius distributions consistent with the observed ones. Most radiative energy escapes in the EUV range, and only a few to tens of percentages of radiative energy can be detected, which provides a solution to the TDE missing energy problem. The deviation between the detected energy and total energy is more severe for optical TDEs than for X-ray TDEs.

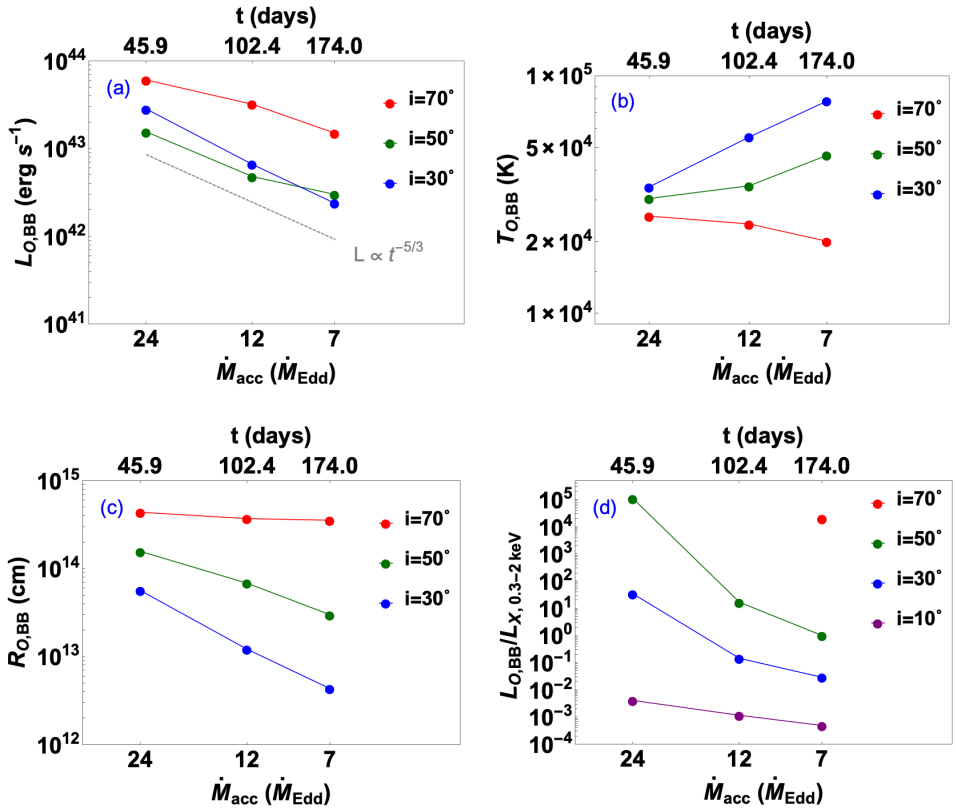

Figure 5.4: The post-peak temporal evolution of (a) the modelled TDE UV/optical luminosity, (b) temperature, (c) radius, and (d) the ratio between the UV/optical and X-ray luminosity. Different colours denote different inclination angles. The escaped radiation has luminosity $L_{\rm bol} = L_{\rm Edd}$ for all curves. The lower axis shows the accretion rate, and the upper axis shows the corresponding time elapsed since the peak, assuming a solar-type star disrupted by a $10^6 M_\odot$ black hole. In panels (a)-(c), we do not include the evolution $i = 10°$, where the event is always X-ray strong. In panel (a), the grey line shows the trend of $t^{-5/3}$ to guide the eye. In panel (d), the X-ray luminosity includes only the flux in the 0.3–2 keV bands for direct comparison with observations. In addition, at $i = 70°$ the X-ray luminosities at the two higher accretion rates are negligible.

- The observed diversity of the emission from different TDEs can be associated with the different Eddington ratios of their accretion rates, $\dot{M}_{\rm acc}$ = few $\times$ (1 − 10) $\dot{M}_{\rm Edd}$, at the peak. In general, higher accretion levels induce larger (fitted blackbody) luminosities and larger photosphere radii but do not significantly change the fitted effective temperatures.
- The early-time evolution ($t \approx 100$ days after peak) of optical TDEs can be explained by this reprocessing model. As the luminosity drops by about 0.5-1 order of magnitude, the fitted temperature slightly increases at small to intermediate inclinations or decreases at large inclinations.

- The evolution of the optical-to-X-ray flux ratio also depends sensitively on the viewing angle. At large inclinations, the TDE stays UV/optically strong for a very long time. At intermediate inclinations, we expect to see the fastest X-ray brightening, and L_O/L_X reaches unity at a few hundred days. At small inclinations, the TDE is always X-ray strong. The exact evolution timescale also depends on the accretion rate at peak, which further depends on the black hole and stellar parameters.

Many TDEs also exhibit distinct spectroscopic properties. In the optical range, TDEs can be characterised by producing strong and broad H, or He, or Bowen fluorescence emission lines or being featureless (Leloudas et al., 2019; van Velzen et al., 2020; Charalampopoulos et al., 2022; Hammerstein et al., 2023). Their UV spectra can display broad absorption line (BAL) or broad emission line (BEL) features, as also observed in some types of quasars (Hung et al., 2019). Some theoretical work has been done to understand TDE spectra. In particular, Parkinson et al. (2020, 2022) have modelled TDE UV/optical continuum and line spectra based on a reprocessing model. They adopted a biconical 2D disk wind toy model, somewhat similar to ours, but they focused on the phases after the peak when the accretion rate and wind mass rate both drop below the Eddington level. They injected a broadened blackbody spectrum of a thin disk. They showed that the reprocessing could be well fitted to the observed continuum of optical TDEs and BAL or BEL features, depending on whether the observer's line of sight intersects the wind. Compared to our model, the level of reprocessing is much lower in theirs due to the low wind density, and as a result, their X-rays are not entirely absorbed from any inclination. In addition, we have not studied the TDE line proprieties in the current work since our current Sedona simulations do not have frequency grids fine enough to capture the bound–bound transitions fully. In future work, we plan to address this issue and conduct TDE spectroscopic modellings.

Furthermore, while our GRRMHD simulations are conducted in 3D, we have done post-processing using a 1D setting; we use the gas profile inside a particular inclination bin and assume that it is spherically symmetric. This means that when viewing a TDE at low inclinations, due to the geometric effects, we only include the emissions leaked out from the funnel regions but miss those from the wind/outer disk. Therefore, we could have underestimated the optical emissions observed from low inclinations. In addition, as shown by Parkinson et al. (2020, 2022), implementing 2D or 3D radiative transfer calculations can allow one to follow photons along more realistic paths, which induce effects such as the reduction of photon trapping in the wind. We will also work toward including 2D/3D radiative transfer calculations in our post-processing simulation.

In this work, we have varied the accretion rate while keeping the same black hole mass and spin parameters. If adopting the thin-disk model, one expects that TDEs from more massive black holes should produce a higher L_O/L_X owing to the combined effects on disk temperatures from larger black hole mass and lower fallback/accretion

rate. However, our calculation shows that more X-rays can leak out in the super-Eddington regime as the accretion rate drops. Therefore, the dependence between TDE emission and black hole mass might be subtle due to these two opposite effects. The black hole spin is expected to be important for the funnel structure, jet launching, and, therefore, the production of non-thermal X-ray emissions. Future work studying how black hole parameters affect TDE emissions will enhance our understanding of TDEs and other super-Eddington systems, such as ultraluminous X-ray sources.

Last but not least, a series of reprocessing models have been raised to explain TDE optical emissions, most of which employ a spherically symmetric envelope for the calculations (e.g., Metzger & Stone, 2016; Roth et al., 2016; Matsumoto & Piran, 2021). While these 1D models offer insights into the radiative transfer physics and our post-processing calculations are also conducted under a 1D setting, it is important to emphasise that the real reprocessing gaseous envelope likely has asymmetric structure and mass distributions (as constrained using polarimetry by Leloudas et al., 2022), so 1D calculations can overestimate the mass needed for reprocessing. Using disk structures from 3D novel simulations, we have demonstrated that the stellar debris mass falling back at an early time is sufficient to reprocess most X-rays into UV/optical emissions when the observer is viewing from relatively large inclinations.

5.5 Acknowledgement

We thank K. Auchettl, C. Bonnerot, M. Bulla, J. Garcia, S. Gezari, E. Kara, D. Kasen, C. Knigge, G. Leloudas, B. Mockler, N. Stone, and S. van Velzen for useful discussions. We also acknowledge the anonymous referee for constructive comments. L.T., T.K. and L.D. acknowledge the support from the Hong Kong Research Grants Council (HKU27305119, HKU17304821) and the National Natural Science Foundation of China (HKU12122309). E.R.-R. is grateful for support from the Heising-Simons Foundation, NSF (AST-1615881, AST-1911206, and AST-1852393), Swift (80NSSC21K1409, 80NSSC19K1391), and Chandra (GO9-20122X). This material is based on work supported by the National Science Foundation Graduate Research Fellowship under grant No. DGE-1745301. The simulations carried out for this project were performed on the HPC computing facilities offered by ITS at HKU and the Tianhe-2 supercluster.

Chapter 6

Conclusions and Future Work

Super-Eddington accretion flows display morphologically distinct geometric features compared to the standard thin disks. Numerical simulations indicate that these disks can launch fast and optically thick winds, which have not been observed in other black hole accretion regimes. This dissertation connects theoretical and observational studies of super-Eddington accretion flow by investigating their observable characteristics through radiative transfer studies. The study is divided into two main components, the X-ray reverberation and the SED of the accretion flow.

For the first study (Chapters 3 and 4), I employ a general relativistic ray-tracing code to explore X-ray reverberation signatures produced by the super-Eddington accretion flows. The results show that these signatures exhibit morphologically distinct features due to reflection occurring in a narrow funnel structure embedded in the fast outflowing wind rather than the mid-plane of a disk, as in the case of a thin disk. Emission lines, such as the characteristic Fe Kα line, are typically bluer, more symmetric in shape, and delayed on a much shorter timescale due to the funnel-wind reflection geometry. I have used this model to successfully account for the observed Fe Kα line of the likely super-Eddington accretor Swift J1644+57.

For the second study (Chapter 5), I employ the Monte Carlo radiative transfer code Sedona to study the continuum emission generated in super-Eddington accretion flows, with a focus on their relevance to TDEs. As the X-ray emissions produced in the inner disk go through the super-Eddington accretion flow, the X-ray photons can be down-scattered or absorbed and remitted as UV/optical photons. My results demonstrate that the inclination of the observer with respect to the disk orientation primarily determines whether the event will be optically (high inclination) or X-ray bright (low inclination). Additionally, this dynamical model can explain the evolution of the emissions, such as the X-ray brightening at late time.

Besides the projects mentioned in the main Chapters, I have also contributed to various finished or ongoing projects, some of which are listed below.

Polarisation of TDEs
Polarimetry studies of electromagnetic light are valuable for gaining insights into the physics of TDEs. Recently, I participated in a project that conducted one of the first

TDE optical spectropolarimetry observations for three TDEs: AT2018dyb, AT2019azh, and AT2019dsg. Our findings revealed that polarisation, combined with spectra, can effectively constrain the TDE disk/wind geometry. My contribution to the project involved comparing the observations with models and conducting some of the analysis. As a result of our work, we published the paper entitled "An asymmetric electron-scattering photosphere around optical tidal disruption events" by Leloudas G., Bulla M., Cikota A., Dai L., **Thomsen L. L.**, Maund J. R., Charalampopoulos P., et al., 2022, Nature Astronomy, 6, 1193. doi:10.1038/s41550-022-01767-z,

Multiple Reflections in X-ray Reverberation
Building on the research described in Chapters 3 and 4, I am contributing to ongoing work investigating the behaviour of photons as they undergo multiple reflections within the super-Eddington funnel geometry before leaving it. This phenomenon of "returning radiation" has been demonstrated to be significant for thin disk geometries, and its impact should be even more pronounced when photons can be reflected multiple times in the narrow funnel structure typically found in super-Eddington sources.

Line Modelling
Until now, TDE modellers have not fully utilised the valuable information contained in emission/absorption lines. Beyond the SED modelling, as mentioned in Chapter 5, I am now conducting more radiative transfer simulations to investigate how we can use the TDE lines to constrain the geometry and kinematics of the gas, focusing on studying the different spectroscopic classes of optical TDEs (Leloudas et al., 2019; van Velzen et al., 2020; Hammerstein et al., 2023).

In conclusion, my PhD dissertation has demonstrated the essentiality of conducting radiative transfer calculations to obtain observable spectroscopic or temporal signatures from GRRMHD simulations of the physical processes around black holes. Through such studies, we can constrain important physical parameters of the accretion disk and the black holes and probe emission physics under extreme accretion conditions.

Appendix A

Accretion Physics

A.1 Thin Disk

In this section, I derive some of the well-known results of thin accretion disks based on Frank et al. (2002). First, I consider non-relativistic disks rotating at Keplerian speed, expressed in cylindrical coordinates (r, ϕ, z). Due to viscous forces arising from differential rotation (e.g. friction or turbulence due to magnetic field lines), the gas in the disk will have a small radial inflow velocity $v_r(r,t) << v_\phi = r\Omega(r)$. Assuming the disk is axis-symmetric and geometrically thin, with a small vertical scale height H compared to its radius ($H/r << 1$), I define the surface density (Σ) as the density (ρ) vertically integrated over the disk height: $\Sigma(r,t) = \int_{-z_0}^{z_0} \rho dz$. For simplicity, I assume the disk to be in a steady state, so the mass inflow ($\dot{M}$) can be written, due to mass conservation, as:

$$\dot{M} = 2\pi\rho \int_{-z_0}^{z_0} r(-v_r)dz = -2\pi r v_r \Sigma = \text{constant}. \tag{A.1}$$

Under steady-state conditions, the angular momentum of each annulus is conserved. The angular momentum per unit mass and the total angular momentum can be expressed as $j = v_\phi r = r\Omega(r)$ and $dJ = (2\pi r\Sigma dr)j$, respectively. The mass flow caries the angular momentum of the gas inwards as $\dot{J}_{\text{Mass Flow}} = \dot{M}j$. Meanwhile, the viscous force (F_{viscous}), which drives the inflow, carries angular momentum outwards. This force arises due to the differential rotation (represented by the term $d\Omega/dr$) in the disk and can be described by the Shakura-Sunyaev prescription (Shakura & Sunyaev, 1973):

$$F_{\text{viscous}} = \nu\Sigma(r\frac{d\Omega}{dr}). \tag{A.2}$$

The viscous torque, arising from the viscous force, is:

$$G(r) = (2\pi\rho F_\nu)r = 2\pi\Sigma r^3 \frac{d\Omega}{dr} = 0 \tag{A.3}$$

The total rate of losing/gaining angular momentum can now be written as:

$$\dot{J} = \dot{M}j + G. \tag{A.4}$$

Since the change in angular momentum is conserved in each annulus due to steady-state conditions, I perform a Taylor expansion in terms of r:

$$\frac{\partial dJ}{\partial t} = \dot{J} = \Delta r \frac{\partial \dot{J}}{\partial r} = \Delta r \frac{\partial \dot{M} j}{\partial r} + \Delta r \frac{\partial G}{\partial r} = -2\pi \Delta r \frac{\partial}{\partial r}(r \Sigma v_r r \Omega) + \Delta r \frac{\partial G}{\partial r} = 0. \tag{A.5}$$

In the limit of $\Delta r \to 0$, the momentum equation becomes:

$$-\dot{M} \frac{\partial}{\partial r}(r\Omega) = 2\pi \frac{\partial}{\partial r}\Big(\Sigma \nu r^3 \frac{d\Omega}{dr}\Big). \tag{A.6}$$

This can be integrated to yield the following expression:

$$\nu \Sigma r^{1/2} = \frac{\dot{M}}{3\pi}(r)^{1/2} + \text{const}, \tag{A.7}$$

where I have used that the disk is rotating at Keplerian speed with $\Omega = \sqrt{\frac{GM}{r^3}}$ to derive the result. Additionally, I can assume no torques exist beyond the innermost stable circular orbit (ISCO) by setting $G = 0$ at the ISCO. By doing so, I could estimate the constant of integration and obtain the complete expression.

$$\nu \Sigma = \frac{\dot{M}}{3\pi}\Big[1 - \Big(\frac{R_{\text{ISCO}}}{r}\Big)^{1/2}\Big]. \tag{A.8}$$

The energy resulting from the viscous force can be determined by calculating the amount of viscous dissipation per unit area (Q), which provides an estimate of:

$$Q(r) = \nu \Sigma \Big(r \frac{d\Omega}{dr}\Big)^2 = 3\frac{GM\dot{M}}{4\pi r^3}\Big[1 - \Big(\frac{R_{\text{ISCO}}}{r}\Big)^{1/2}\Big] \tag{A.9}$$

The corresponding luminosity (L) is:

$$L = \int_{R_{\text{ISCO}}}^{\infty} Q(r) 2\pi r dr = \frac{GM\dot{M}}{2R_{\text{ISCO}}} = \frac{1}{2}E_{\text{pot}}, \tag{A.10}$$

so the thin disk radiates half its potential energy away - the other half is lost in kinetic energy. The thin disk is optically thick (Shakura & Sunyaev, 1973), so the dissipative radiation can be described as black body radiation. Therefore, given the dissipation, one can assign a surface temperature (T_s) of the disk at a given radius by using the Stefan Boltzmann equation:

$$2\sigma T_s(r)^4 = Q(r), \tag{A.11}$$

where σ is the Stefan-Boltzmann constant, and the factor of 2 arises from the emitting top and bottom part of the disk. The disk's temperature increases towards the central object, reaching a maximum at the innermost part of the disk where the matter is orbiting the black hole at the highest velocity. The temperature profile of the disk is given by

$$T_s(r) = 3\frac{GM\dot{M}}{8\pi\sigma r^3}\Big[1 - \Big(\frac{R_{\text{ISCO}}}{r}\Big)^{1/2}\Big] \tag{A.12}$$

The density profile (ρ) of the thin accretion disk can be determined by considering hydro-static equilibrium in the vertical direction, where no bulk motion ($v_{\rm bulk} = 0$) is present since I have assumed the orbits are purely Keplerian. This leads to the following equation:

$$\frac{1}{\rho}c_s^2\frac{\partial r}{\partial z} = \frac{\partial}{\partial z}[\frac{GM}{(r^2+z^2)^{1/2}}] = \frac{\partial}{\partial z}[\frac{GM}{(r^2+z^2)^{1/2}}] = -\frac{GM}{r^2}z/r = -\Omega^2 z, \tag{A.13}$$

where I have used $z/r << 1$ and c_s is the sound speed. The differential equation can be solved, and the density as a function of scale height $H = \sqrt{2}c_s/\Omega$ is:

$$\rho(z) = \rho_0 \exp\left(-z^2\Omega^2/(2c_s^2)\right) = \rho_0 \exp\left(-z^2/H^2\right), \tag{A.14}$$

Appendix B

Appendix Chapter 4

B.1 Local Isotropic Irradiation in GR

B.1.1 Vierbein Transformation Matrix

The transformation to local frame in GR is the vierbein transformation matrix, which is a (4×4) matrix consisting of four 'legs' $\left(e_{\hat{t}}, e_{\hat{x}}, e_{\hat{y}}, e_{\hat{z}}\right)$. It can be found using the following transformation equations from Eq. 2.8. A hatted vector means as measured in its local reference frame, and unhatted parameters are measured in the 'global' Boyer-Lindquist coordinates.

The normal convention is to set the time-like first leg to be the 4-velocity since it automatically fulfils the equation 2.8 due to the velocity normalisation criteria: $g_{\mu\nu}u^{\mu}u^{\nu} = -1$. In the Boyer-Lindquist coordinate frame, the velocity of a rotating coronal source is given by $\vec{u} = u^t(1, 0, 0, \Omega)$. From the velocity normalisation, one finds

$$u^t = \sqrt{\frac{-1}{g_{tt} + 2\Omega g_{t\phi} + \Omega^2 g_{\phi\phi}}}.$$

Therefore, the first of the four legs of the vierbein transformation matrix is:

$$e^{\mu}_{\hat{t}} = \left(\sqrt{\frac{-1}{g_{tt} + 2\Omega g_{t\phi} + \Omega^2 g_{\phi\phi}}}, 0, 0, \sqrt{\frac{-\Omega^2}{g_{tt} + 2\Omega g_{t\phi} + \Omega^2 g_{\phi\phi}}}\right). \tag{B.1}$$

The two next legs can easily be calculated by noting that the local basis $(\hat{z}, \hat{y})$ is parallel to the Boyer-Lindquist basis vector $(\vec{r}, \vec{\theta})$. Since there is no cross term in $g_{\mu\nu}$ for $(\vec{r}, \vec{\theta})$, the two legs of the vierbein transformation matrix can be calculated using the normalisation condition given in equation 2.8, so:

$$e^{\mu}_{\hat{z}} = \left(0, \sqrt{\frac{1}{g_{rr}}}, 0, 0\right) = \left(0, \sqrt{\frac{\Delta}{\Sigma}}, 0, 0\right), \tag{B.2}$$

$$e^{\mu}_{\hat{y}} = \left(0, 0, \sqrt{\frac{1}{g_{\theta\theta}}}, 0\right) = \left(0, 0, \sqrt{\frac{1}{\Sigma}}, 0\right). \tag{B.3}$$

The last leg in the vierbein transformation matrix is $(e^{\mu}_{\hat{x}})$, which needs to account for the cross term in the metric element $g_{t\phi}$, so a simple ansatz is that the last leg has the following form:

$$e^{\mu}_{\hat{x}} = (e^{t}_{\hat{x}}, 0, 0, e^{\phi}_{\hat{x}}). \tag{B.4}$$

Furthermore, we use that it has to be orthogonal to the other transformation bases (legs), which yields:

$$\begin{aligned} &g_{\mu\nu} e^{\mu}_{\hat{x}} e^{\nu}_{\hat{t}} = 0 \\ &g_{tt} e^{t}_{\hat{x}} e^{t}_{\hat{t}} + g_{t\phi} e^{t}_{\hat{x}} e^{\phi}_{\hat{t}} + g_{\phi t} e^{\phi}_{\hat{x}} e^{t}_{\hat{t}} + g_{\phi\phi} e^{\phi}_{\hat{x}} e^{\phi}_{\hat{t}} = \\ &e^{t}_{\hat{x}} \left(g_{tt} e^{t}_{\hat{t}} + g_{t\phi} e^{\phi}_{\hat{t}} \right) + e^{\phi}_{\hat{x}} \left(g_{\phi t} e^{t}_{\hat{t}} + g_{\phi\phi} e^{\phi}_{\hat{t}} \right) = 0. \end{aligned} \tag{B.5}$$

So, there exists the following simple relation between the two components:

$$e^{\phi}_{\hat{x}} = \frac{-\left(g_{tt} e^{t}_{\hat{t}} + g_{t\phi} e^{\phi}_{\hat{t}} \right)}{\left(g_{\phi t} e^{t}_{\hat{t}} + g_{\phi\phi} e^{\phi}_{\hat{t}} \right)} e^{t}_{\hat{x}} = \frac{-\left(g_{tt} + \Omega g_{t\phi} \right)}{\left(g_{t\phi} + \Omega g_{\phi\phi} \right)} e^{t}_{\hat{x}} = \frac{-g_{tt} - \Omega g_{t\phi}}{g_{\phi\phi}(\Omega - \omega)} e^{t}_{\hat{x}}, \tag{B.6}$$

where we have used that $e^{\phi}_{\hat{t}} = \Omega e^{t}_{\hat{t}}$, and we have introduced the frame dragging velocity $\omega = -g_{t\phi}/g_{\phi\phi}$. The transformation (normalisation) condition from equation 2.8 gives the following expression:

$$\begin{aligned} &g_{tt} e^{t}_{\hat{x}} e^{t}_{\hat{x}} + 2 g_{t\phi} e^{t}_{\hat{x}} e^{\phi}_{\hat{x}} + g_{\phi\phi} e^{\phi}_{\hat{x}} e^{\phi}_{\hat{x}} = \\ &(e^{t}_{\hat{x}})^2 \left(g_{tt} - 2 g_{t\phi} \left(\frac{g_{tt} + \Omega g_{t\phi}}{g_{\phi\phi}(\Omega - \omega)} \right) + g_{\phi\phi} \left(\frac{g_{tt} + \Omega g_{t\phi}}{g_{\phi\phi}(\Omega - \omega)} \right)^2 \right) = 1. \end{aligned} \tag{B.7}$$

Next, the leg component $e^{t}_{\hat{x}}$ can be isolated, and from Eq. B.6, we can quickly find the expression for the other leg component $e^{\phi}_{\hat{x}}$. The full expression for the last leg of the vierbein transformation matrix is:

$$\begin{aligned} e^{\mu}_{\hat{x}} = \Bigg(&\frac{\Omega - \omega}{\sqrt{g_{tt}(\Omega - \omega)^2 - 2 g_{t\phi}(\Omega - \omega) \left(\frac{g_{tt} + \Omega g_{t\phi}}{g_{\phi\phi}} \right) + \frac{\left(g_{tt} + \Omega g_{t\phi} \right)^2}{g_{\phi\phi}}}}, 0, \\ 0, &\frac{-\left(g_{tt} + \Omega g_{t\phi} \right)}{\sqrt{g_{tt} g_{\phi\phi}^2 (\Omega - \omega)^2 - 2 g_{t\phi} g_{\phi\phi} (\Omega - \omega) \left(g_{tt} + \Omega g_{t\phi} \right) + g_{\phi\phi} \left(g_{tt} + \Omega g_{t\phi} \right)^2}} \Bigg). \end{aligned} \tag{B.8}$$

The transformation simplifies significantly for a stationary observer with $\Omega = 0$ and an observer rotating with the frame-dragging speed $\Omega = -g_{\phi t}/g\phi\phi = \omega$, which is known as a ZAMO (Zero-Angular-Momentum-Observer).

B.1.2 Stationary Observer

A stationary observer with $\Omega = 0$ will have the following simplified expressions of $e^{\mu}_{\hat{t}}$ and $e^{\mu}_{\hat{x}}$:

$$e^{\mu}_{\hat{t}} = \left(\sqrt{\frac{-1}{g_{tt}}}, 0, 0, 0\right)_{\text{STATIONARY}} \tag{B.9}$$

$$e^{\mu}_{\hat{x}} = \left(\frac{1}{\sqrt{g_{\phi\phi}\left(\frac{g_{tt}}{g_{t\phi}}\right)^2 - g_{tt}}}, 0, 0, \frac{-1}{\sqrt{g_{\phi\phi} - \frac{(g_{t\phi})^2}{g_{tt}}}}\right)_{\text{STATIONARY}}. \tag{B.10}$$

From equation 2.9, the initial four-momentum of a photon emitted by a stationary corona in the Boyer-Lindquist coordinates can be expressed as:

$$\begin{aligned}
\dot{t}_{\text{STATIONARY}} &= p^t = e^t_{\hat{t}} p^{\hat{t}} + e^t_{\hat{x}} p^{\hat{x}} = \frac{-E_0}{\sqrt{-g_{tt}}} + \frac{E_0 \sin(\alpha)\cos(\beta)}{\sqrt{g_{\phi\phi}\left(\frac{g_{tt}}{g_{t\phi}}\right)^2 - g_{tt}}} \\
\dot{r}_{\text{STATIONARY}} &= p^r = e^r_{\hat{z}} p^{\hat{z}} = E_0 \cos(\alpha)\sqrt{\frac{\Delta}{\Sigma}} \\
\dot{\theta}_{\text{STATIONARY}} &= p^\theta = e^\theta_{\hat{y}} p^{\hat{y}} = \frac{E_0 \sin(\alpha)\sin(\beta)}{\sqrt{\Sigma}} \\
\dot{\phi}_{\text{STATIONARY}} &= p^\phi = e^\phi_{\hat{x}} p^{\hat{x}} = \frac{-E_0 \sin(\alpha)\cos(\beta)}{\sqrt{g_{\phi\phi} - \frac{(g_{t\phi})^2}{g_{tt}}}}.
\end{aligned} \tag{B.11}$$

B.1.3 ZAMO

In a Kerr space-time, a stationary observer is an observer that is co-rotating with the space-time geometry of the BH since objects within the ergosphere cannot appear stationary to a truly static observer far away (Bardeen et al., 1972). This observer, rotating with the frame-dragging velocity $d\phi/d\tau = \Omega = \omega = -g_{t\phi}/g_{\phi\phi}$, is known as a ZAMO (Krawczynski & Beheshtipour, 2017) and it is the standard observer in GR. The ZAMO observer is characterised by having zero angular momentum, and its position is fixed at constant r and θ, so $p_\phi = L_z = \dot{r} = \dot{\theta} = 0$. For a ZAMO, the two legs of the transformation matrix $(\hat{t}, \hat{x})$ simplify to:

$$e^{\mu}_{\hat{t}} = \left(\sqrt{\frac{-1}{g_{tt} - \frac{g^2_{t\phi}}{g_{\phi\phi}}}}, 0, 0, \sqrt{\frac{-1}{g_{tt}\frac{g^2_{\phi\phi}}{g^2_{t\phi}} - g_{\phi\phi}}}\right)_{\text{ZAMO}} \tag{B.12}$$

$$e^{\mu}_{\hat{x}} = \left(0, 0, 0, \frac{-1}{\sqrt{g_{\phi\phi}}}\right)_{\text{ZAMO}}. \tag{B.13}$$

This simple transformation of $e^{\mu}_{\hat{x}}$, for a ZAMO, means that a particle with velocity $\dot{\phi} = 0$ in the BL frame will keep having zero velocity in the ZAMO-frame, which is an additional advantage of such an observer. Suppose the local reference frame of an object

differs from that of the ZAMO (other velocity profile). In that case, one can always get the local reference frame by adding the Lorentz factor, which takes the relative motion between the ZAMO and local reference frame of the object into account (Bardeen et al., 1972). A ZAMO observer has the 3-velocity $v_\phi = v_r = v_\theta = 0$, so the relative velocity is found by transforming the 4-velocity of the particle U^μ into the ZAMO frame with the following equation:

$$v_{\hat{i}} = \frac{g_{\mu\nu} U^\mu e^\nu_{\hat{i}}}{g_{\mu\nu} U^\mu e^\nu_{\hat{t}}}. \tag{B.14}$$

B.2 Relativistic Proper Area

We find the GR proper area of surface elements by performing the Jacobian. Our super-Eddington disk structure has been averaged in the azimuthal (ϕ) direction, so it is axis-symmetric in the z-direction. Therefore, we are looking for a mapping F that maps the photosphere from (r, θ, ϕ) to (ρ, ϕ):

$$\Big(\rho, \phi\Big) \underset{\mapsto}{F} \Big(r, \theta, \phi\Big) = \Big(r(\rho), \theta(\rho), \phi\Big). \tag{B.15}$$

The transformation is given by the metric tensor:

$$h = \begin{bmatrix} \langle \Sigma_k \lambda_{k\rho} \lambda_{k\rho} \rangle & \langle \Sigma_k \lambda_{k\rho} \lambda_{k\phi} \rangle \\ \langle \Sigma_k \lambda_{k\phi} \lambda_{k\rho} \rangle & \langle \Sigma_k \lambda_{k\phi} \lambda_{k\phi} \rangle \end{bmatrix} = \begin{bmatrix} g_{rr} \big(\frac{\partial r}{\partial \rho}\big)^2 + g_{\theta\theta} \big(\frac{\partial \theta(\rho)}{\partial \rho}\big)^2 & 0 \\ 0 & g_{\phi\phi} \frac{\partial \phi}{\partial \phi} \end{bmatrix}, \tag{B.16}$$

where $\lambda_{ij} = \frac{\partial F_i}{\partial u_j}$ is the Jacobian, and F is the mapping from $\big(r(\rho), \theta(\rho), \phi\big)$ to $u = (\rho, \phi)$. Here, $< * >$ denotes the inner product under the metric, and Σ_k is the summation over all indices k. The proper area, as seen by a stationary observer, is:

$$A_{\text{stationary}} = \sqrt{\det(h)} d\rho d\phi, \tag{B.17}$$

where $\det(h)$ is the determinant of h. The subscript "stationary" means the proper area in the frame of a ZAMO observer. In order to get the area as seen by the super-Eddington disk, we need to add the Lorentz factor between the ZAMO and disk elements using Eq. B.14

Appendix C

Appendix Chapter 5

C.1 Properties of Simulated Disks

A few more time-averaged quantities of the three simulated disks are listed in Table C.1. Φ_H is the normalised magnetic flux at horizon (Tchekhovskoy et al., 2011), with $\Phi_H \gtrsim 30-40$ being the condition for MADs. The net accretion efficiency, η_H, evaluates how much rest-mass energy going into the black hole is converted to outgoing energy near the event horizon. $L_{\rm jet}$ is the total power of the relativistic jet at $r = 5500r_g$, most of which is in the form of electromagnetic energy. $\Gamma_{\rm jet,max}$ is the maximum Lorentz factor of the jet. L_K is the thermal+kinetic luminosity of the wind calculated at $r \sim 5500r_g$. $\alpha_{\rm eff}$ is the effective α-parameter of the disk as defined in McKinney et al. (2012). $R_{\rm eq}$ indicates the radius within which the disk inflow equilibrium has been established. In our simulations, the winds are launched mostly from the inner disk regions and have travelled beyond the photospheres at most inclination angles.

Model	$\dot{M}_{\rm acc}$ ($\dot{M}_{\rm Edd}$)	Φ_H	η_H (%)	$L_{\rm jet}$ ($L_{\rm Edd}$)	$\Gamma_{\rm jet,max}$	L_K ($L_{\rm Edd}$)	$\alpha_{\rm eff}$	$R_{\rm eq}$ (R_g)
M6a08-1	7	34.5	35.5	1.1	2.27	0.5	2.7	340
M6a08-2	12	39	40.1	2.3	2.39	1.0	3.3	320
M6a08-3	24	55	69.3	9.7	2.66	4.8	2.3	230

Table C.1: More disk quantities

C.2 Radiative Transfer Physics

In our radiative transfer calculations, the X-rays, injected from the inner disk, are re-processed mainly owing to three mechanisms:

1. "Adiabatic expansion": The accumulation of multiple scatterings of photons in a diverging, fast-moving, optically thick wind can increase the photon wavelength due to Doppler shift. In the limit that the photons remain entirely trapped, the change in the radiation energy density can be computed based on the thermodynamics of adiabatic expansion. For the radiative transfer calculations in this paper, the fully adiabatic limit does not apply, but the result is still that photon

energies are downgraded as they traverse the wind. The amount of photon energy change depends on the velocity divergence of the wind and the number of scatterings photons undergo before they escape.

2. Absorption and re-emission: The absorption of X-rays in the accretion flow is dominated by bound–free interactions. Each bound–free absorption event acts as a heating source for the free electrons. Meanwhile, free electrons can recombine to produce fluorescence lines, which is a cooling mechanism for the free electrons. The amount of bound–free absorption depends on the number of bound electrons available to be ionised at a given location.

3. Compton scattering: Electron recoil causes scattering events to be non-coherent in the fluid rest frame, heating the electrons and downgrading the photon energies. Meanwhile, the thermal motion of electrons can transfer energy from the electrons to the photons when the electron temperature is sufficiently high. With a typical gas temperature between $10^6 - 10^4 K$ in our accretion flow, X-ray photons are expected to lose energy, and optical photons overall will gain energy due to Compton scattering. In the latter case (direct Compton scattering), we note that the induced electron temperature change is not included in this version of SEDONA. One can estimate how important Compton scattering is by calculating the Compton y parameter, which is the average energy change per scattering times the number of scatterings. If inverse Compton scattering dominates, we have $y_{IC} = kT_{\rm eff}/(m_e c^2) \times \max(\tau_{\rm es}, \tau_{\rm es}^2)$ and if Compton scattering dominates, we have $y_C = h\nu/(m_e c^2) \times \max(\tau_{\rm es}, \tau_{\rm es}^2)$. Here k is the Stefan-–Boltzmann constant, m_e is the electron mass, T_e is the electron temperature, and $T_{\rm eff}$ is the optical-depth-averaged gas temperature $T_{\rm eff} = \int T\kappa_{\rm es}\rho dr/\tau_{\rm es}$, where $\kappa_{\rm es}$ is the electron-scattering opacity and $\tau_{\rm es}$ is the total electron-scattering optical depth.

In Fig. C.1, we highlight the importance of the three reprocessing mechanisms in gas with different physical conditions. We choose a low-inclination case ($i = 30°$) where the wind velocity is very high and a high-inclination case ($i = 70°$) where the wind optical depth is very large. We plot the spectra and the corresponding wavelength-dependent optical depth (the sum of scattering and all absorption opacities). For the low-inclination case, we see that only the photoionisation cross sections of O VII and O VIII contribute a small amount to the overall optical depth since the gas is almost totally ionised and we are dominated by electron scattering. Therefore, absorption is not effective for reprocessing for this case, and neither is inverse Comptonisation since $y_{\rm IC} = 0.002$ due to the dilute wind. What reddens the escaped spectrum compared to the injected spectrum is mostly the adiabatic expansion with a small contribution from Compton scattering of X-ray photons (e.g., $y_{\rm C} = 0.2$ for $\lambda = 10$ Å). For the high-inclination case, gas is much denser and cannot be fully ionised by the injected radiation. The optical depth is very large due to the photoionisation of different oxygen species existing throughout the wind, as well as some helium. Therefore, the spectral

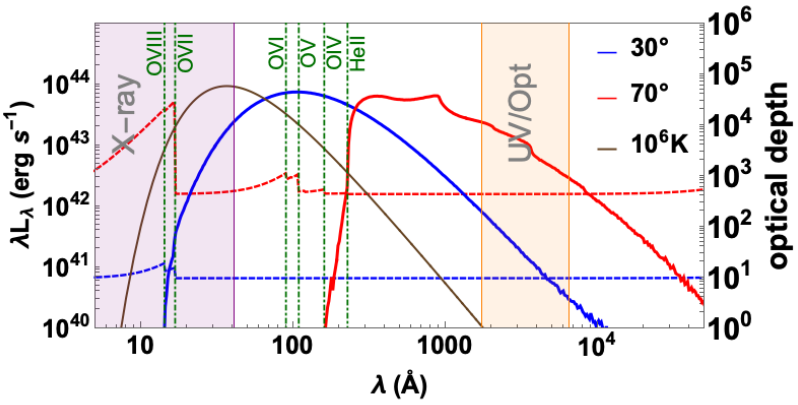

Figure C.1: The optical depth as a function of the wavelength (dashed curve) overlaid with the escaped spectra (solid curve) at two different inclinations $i = 30°$ and $i = 70°$ for the simulation with $\dot{M}_{\rm acc} = 12\,\dot{M}_{\rm Edd}$ and $L_{\rm bol} = L_{\rm Edd}$. The injected Planck spectrum at $T = 10^6$K (thin brown curve) is also plotted to show the level of reprocessing. The photoionisation edges have been marked with green vertical lines and labelled.

flux is suppressed mainly by O and He absorption. The large absorption opacities for X-ray photons lessen the importance of Compton scattering. Although, we have $y_{\rm C} = 459$ for $\lambda = 10$ Å, X-rays would still be all reprocessed even if Compton scattering were not included, and the overall optical continuum level would remain similar. Therefore, the reprocessing in the high-density case is mainly set by the bound–free interactions.

C.3 Simulated Spectra at Higher Luminosity

Spectra are also plotted for the other luminosity setting with $L_{\rm bol} = 10\% \times \dot{M}_{\rm acc}c^2$ and shown in Fig. C.2.

C.4 List of Observed TDEs Reported in the Literature

For plotting Figures 5.3a-5.3c, we use 16 optically selected TDEs and 7 X-ray selected TDEs. For completeness, we list their names and relevant parameters as reported from previous literature in Tables C.2 and C.3.

C.5 Modelled TDE Parameters

The values of the modeled observable as in Fig. 5.3d-5.3f are listed in Table C.4. The modeled bolometric correction, which is defined as $(L_{\rm O,BB} + (L_{\rm X,BB})/L_{\rm bol}$, is plotted in Fig. C.3.

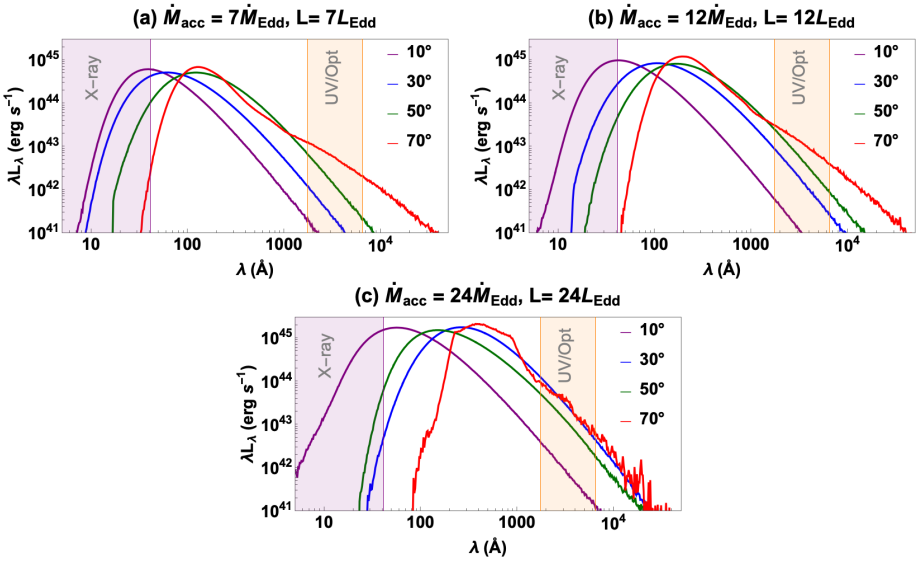

Figure C.2: The simulated escaping spectra of the accretion disk at different accretion rates and inclinations, similar to Figures 5.2a-5.2c, except that the bolometric luminosity of the spectra $L_{\rm bol} = 10\% \times \dot{M}_{\rm acc}c^2$.

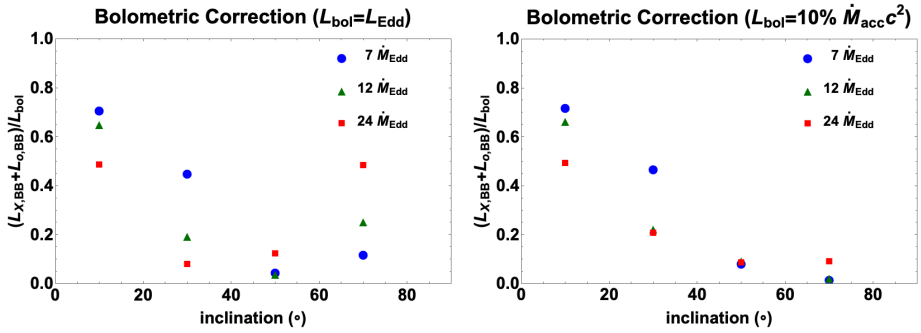

Figure C.3: The modeled bolometric correction $(L_{\rm O,BB} + L_{\rm X,BB})/L_{\rm bol}$ for two escaped luminosity settings. One can see that the luminosity inferred from the observations based on the assumption of blackbody radiation usually misses a large portion of the bolometric luminosity, and this problem is more severe for optical TDEs.

C.6 Characteristic Timescales

There are various physical timescales relevant for TDEs: debris mass fallback timescale, disk formation/circularisation timescale, disk viscous timescale, and photon transport timescale. The longest timescale of all governs the temporal evolution of TDE emissions. The time scales are shown in Table C.5.

The photon transport time through an optically thick medium is the shorter one between the diffusion timescale and advection timescale. The photon diffusion timescale is calculated as $t_{\rm diff} = \tau_{\rm es}\, R_{\rm es}/c$, where $R_{\rm es}$ is the size of the electron-scattering photosphere along a particular inclination and $\tau_{\rm es}$ is the electron-scattering optical depth-integrated radially from $r = 0$ to $r = R_{\rm es}$. The advection timescale is calculated as

Table C.2: Names and parameters of optical TDEs

Name	log $M_{\rm BH}$ ($M_\odot$)	log $L_{\rm BB}$ (erg s^{-1})	log $T_{\rm BB}$ (K)	log $R_{\rm BB}$ (R_g)
ASASSN-14ae	5.42	43.87	4.29	4.34
ASASSN-14li	6.31	43.66	4.52	2.88
ASASSN-15lh	8.47	45.34	4.30	2.00
ASASSN-15oi	5.71	44.45	4.60	3.72
AT2018dyb/ASASSN-18pg	6.67	44.08	4.40	2.97
AT2018hyz/ASASSN-18zj	5.68	44.10	4.25	4.27
GALEXD1-9	6.51	43.48	4.59	2.45
GALEXD23H-1	6.39	43.95	4.70	2.59
GALEXD3-13	7.36	43.98	4.66	1.71
iPTF-15af	6.88	44.10	4.85	1.87
iPTF-16axa	6.34	43.82	4.46	3.05
PS1-10jh	5.85	44.47	4.59	3.61
PTF-09axc	5.68	43.46	4.08	4.29
PTF-09djl	5.82	44.42	4.41	3.97
PTF-09ge	6.34	44.04	4.08	3.92
SDSS-TDE1	7.24	43.64	4.42	2.14

Table C.3: Names and parameters of X-ray TDEs

Name	log $M_{\rm BH}$ ($M_\odot$)	log $L_{\rm BB}$ (erg s^{-1})	log $T_{\rm BB}$ (K)	log $R_{\rm BB}$ (R_g)
SDSS J1323+48	6.15	44.30	5.91	0.80
SDSS J1201+30	7.18	45.00	6.06	-0.29
RX J1624+75	7.68	43.38	6.05	-1.57
RX J1420+53	7.33	43.38	5.67	0.03
RBS 1032	5.25	41.70	6.11	-0.13
3XMM J1521+07	5.61	43.51	6.30	-0.02
3XMM J1500+01	5.64	43.08	6.06	0.29

$t_{\rm adv} \approx R_{\rm es}/v_r$, since the photons trapped by the optically thick gas have a similar speed to the gas. Here the gas radial velocity, v_r, is averaged over the radial path within $R_{\rm es}$ and weighted by gas density. The values of these timescales in the $\dot{M}_{\rm acc} = 12\dot{M}_{\rm Edd}$ accretion flow are given in Table C.5. One can see that, for the inclinations considered in this work, photons are preferably advected out by the optically thick wind. The photon transport time varies from $\sim$0.1 to a few days depending on the inclination.

The disk viscous timescale can be analytically calculated by $t_{\rm visc} = t_{\rm dyn}\,\alpha^{-1}(H/R)^{-2}$, where $t_{\rm dyn}$ is the orbital timescale of the disk, α is a free parameter between 0 and approximately 1, and H/R is the disk thickness (Shakura & Sunyaev, 1973). For our disk parameters, we have $t_{\rm visc} \approx 5.44$ days $(R_{\rm disk}/8500r_g)\,(M_{\rm BH}/10^6 M_\odot)(\alpha/1)^{-1}((H/R)/0.3)^{-2}$. The viscous time scale is therefore only a few days. We caution the readers that our simulated disks are MADs, which typically have effective $\alpha \gtrsim 1$. The viscous time scale is potentially longer if the disks do not have such large magnetic fluxes.

The disk formation/circularisation timescale induces uncertainty in the evolution of TDEs. Recent simulations show that a large fraction of the debris materials can form a disk within a dynamical timescale, but the disk still possesses some moderate eccentricity (Bonnerot et al., 2021). As the topic is out of the scope of this paper, we assume here that the disk forms quickly for the calculation of the emission evolution.

Stellar debris typically falls back on timescales of $t_{\rm mb}$, which is the orbital time of

Table C.4: Modeled TDE observables

$\dot{M}_{\rm acc}$ ($\dot{M}_{\rm Edd}$)	$L_{\rm bol}$ ($L_{\rm Edd}$)	Inc (degree)	log $L_{\rm O,BB}$ (erg s^{-1})	$\frac{L_{\rm O,BB}}{L_{\rm bol}}$	log $T_{\rm O,BB}$ (K)	log $R_{\rm O,BB}$ (cm)	log $L_{\rm X,BB}$ (erg s^{-1})	$\frac{L_{\rm X,BB}}{L_{\rm bol}}$	log $T_{\rm X,BB}$ (K)	log $R_{\rm X,BB}$ (cm)
7	1	10	40.650	0.000	4.47	12.71	43.952	0.710	5.99	11.38
		30	42.212	0.013	4.89	12.64	43.742	0.438	5.91	11.45
		50	42.480	0.024	4.67	13.48	42.475	0.024	5.72	11.85
		70	43.179	0.120	4.30	14.55	38.879	0.000	5.25	13.11
	7	10	42.861	0.008	5.13	12.50	44.799	0.713	5.99	11.80
		30	43.434	0.031	5.04	12.95	44.587	0.438	5.91	11.87
		50	43.691	0.056	4.85	13.72	43.407	0.029	5.74	12.29
		70	43.175	0.017	4.30	14.55	41.422	0.000	5.35	13.55
12	1	10	40.989	0.001	4.55	12.73	43.914	0.651	5.98	11.38
		30	42.503	0.025	4.74	13.09	43.334	0.171	5.78	11.61
		50	42.684	0.038	4.54	13.84	41.451	0.002	5.57	12.05
		70	43.508	0.255	4.38	14.57	-	-	-	-
	12	10	43.364	0.015	5.13	12.75	44.994	0.652	5.99	11.91
		30	43.921	0.055	4.89	13.50	44.413	0.171	5.78	12.15
		50	44.130	0.089	4.78	14.08	42.973	0.006	5.65	12.40
		70	43.558	0.024	4.34	14.66	-	-	-	-
24	1	10	41.407	0.002	4.44	13.15	43.786	0.483	5.98	11.30
		30	42.994	0.078	4.53	13.75	41.452	0.002	5.40	12.17
		50	43.193	0.123	4.48	14.20	-	-	-	-
		70	43.784	0.482	4.41	14.64	-	-	-	-
	24	10	43.427	0.009	4.83	13.37	45.167	0.485	5.99	11.97
		30	44.790	0.204	4.77	14.18	42.977	0.003	5.43	12.80
		50	44.401	0.083	4.76	14.26	43.026	0.004	5.50	13.22
		70	44.444	0.092	4.67	14.46	-	-	-	-

the most bound debris (Evans & Kochanek, 1989; Guillochon & Ramirez-Ruiz, 2013; Rossi et al., 2021):

$$t_{\rm mb} \approx 41 \text{ days } \left(\frac{M_{\rm BH}}{10^6 M_\odot}\right)^{1/2} \left(\frac{m_\star}{M_\odot}\right)^{-1} \left(\frac{r_\star}{R_\odot}\right)^{3/2}. \tag{C.1}$$

For our case with $M_{\rm BH} = 10^6 M_\odot$, $t_{\rm mb}$ varies between 25 and 41 days for $m_\star = 0.1 - 10\ M_\odot$.

Lastly, assuming that the fallback timescale governs the evolution of TDEs, we calculate the time corresponding to each simulated disk with a further assumption that the fallback rate, $\dot{M}_{\rm fb}$, equals the instantaneous accretion rate, $\dot{M}_{\rm acc}$, plus the wind mass rate, $\dot{M}_w$. Here we focus on the post-peak evolution. By setting that the fallback rate peaks at $t_{\rm mb}$, the post-peak time $t_{\rm pp}$ associated with a particular $\dot{M}_{\rm fb}$ can be calculated

Table C.5: Parameters of the reprocessing envelope and timescales of photon propagation for the disk with $\dot{M}_{\rm acc} = 12\dot{M}_{\rm Edd}$ along different inclinations

Quantities \ Inclination (degree)	10°	30°	50°	70°
$R_{\rm es}$ (R_g)	896	1278	5425	8377
1D mass $(M_\odot)$	0.004	0.004	0.02	0.4
$\tau_{\rm es}$	7.0	74.0	137.2	710.2
v_r (c)	0.50	0.35	0.13	0.013
$t_{\rm adv}$ (days)	0.07	0.13	1.06	13.6
$t_{\rm diff}$ (days)	0.35	5.4	42.2	337.4

Table C.6: The epochs post peak corresponding to the three simulations, assuming $M_{\rm BH} = 10^6 M_\odot$ and various different $m_\star$

Quantities \ $m_\star$ $(M_\odot)$	0.2	0.5	1	1.5
$\dot{M}_{\rm fb,peak}$ $(\dot{M}_{\rm Edd})$	36.7	76.4	133.0	211.6
M6a08-3: $t_{\rm pp}(\dot{M}_{\rm fb} = (24+14)\ \dot{M}_{\rm Edd})$ (days)	N/A	18.6	45.9	69.7
M6a08-2: $t_{\rm pp}(\dot{M}_{\rm fb} = (12+4.5)\ \dot{M}_{\rm Edd})$ (days)	18.3	53.8	102.4	140.0
M6a08-1: $t_{\rm pp}(\dot{M}_{\rm fb} = (7+1.4)\ \dot{M}_{\rm Edd})$ (days)	42.3	98.5	174.0	229.2

with

$$\dot{M}_{\rm fb} \approx 133\Big(\frac{M_{BH}}{10^6 M_\odot}\Big)^{-3/2}\Big(\frac{m_\star}{M_\odot}\Big)^2\Big(\frac{r_\star}{R_\odot}\Big)^{-3/2}\Big(\frac{t}{t_{\rm mb}}\Big)^{-5/3}\dot{M}_{\rm Edd}. \tag{C.2}$$

With the wind mass rate given in Table 5.1, the three simulated disks correspond to $\dot{M}_{\rm fb} = \dot{M}_{\rm acc} + \dot{M}_w = (7+1.4, 12+4.5, 24+14)\ \dot{M}_{\rm Edd}$. The post-peak time obtained with $M_{\rm BH} = 10^6 M_\odot$ and a few different $m_\star$ are shown in Table C.6.

Bibliography

Abramowicz, M. A., Calvani, M., & Nobili, L. 1980, ApJ, 242, 772

Abramowicz, M. A., Czerny, B., Lasota, J. P., & Szuszkiewicz, E. 1988, ApJ, 332, 646

Abramowicz, M. A., & Fragile, P. C. 2013, Living Reviews in Relativity, 16, 1

Abramowicz, M. A., Novikov, I. D., & Paczynski, B. 1991, ApJ, 369, 175

Alexander, K. D., Berger, E., Guillochon, J., Zauderer, B. A., & Williams, P. K. G. 2016, ApJ, 819, L25

Alexander, K. D., Wieringa, M. H., Berger, E., Saxton, R. D., & Komossa, S. 2017, ApJ, 837, 153

Andalman, Z. L., Liska, M. T. P., Tchekhovskoy, A., Coughlin, E. R., & Stone, N. 2022, MNRAS, 510, 1627

Auchettl, K., Guillochon, J., & Ramirez-Ruiz, E. 2017, ApJ, 838, 149

Bañados, E., et al. 2018, Nature, 553, 473

Bade, N., Komossa, S., & Dahlem, M. 1996, A&A, 309, L35

Balbus, S. A., & Hawley, J. F. 1991, ApJ, 376, 214

Ballantyne, D. R., & Ramirez-Ruiz, E. 2001, ApJ, 559, L83

Bambynek, W., Crasemann, B., Fink, R. W., Freund, H. U., Mark, H., Swift, C. D., Price, R. E., & Rao, P. V. 1972, Reviews of Modern Physics, 44, 716

Bardeen, J. M., & Petterson, J. A. 1975, ApJ, 195, L65

Bardeen, J. M., Press, W. H., & Teukolsky, S. A. 1972, ApJ, 178, 347

Begelman, M. C. 1978, MNRAS, 184, 53

Begelman, M. C., McKee, C. F., & Shields, G. A. 1983, ApJ, 271, 70

Beloborodov, A. M. 1998, MNRAS, 297, 739

Berger, E., Zauderer, A., Pooley, G. G., Soderberg, A. M., Sari, R., Brunthaler, A., & Bietenholz, M. F. 2012, ApJ, 748, 36

Blandford, R., Yuan, Y., Hoshino, M., & Sironi, L. 2017, Space Sci. Rev., 207, 291

Blandford, R. D., & Payne, D. G. 1982, MNRAS, 199, 883

Blandford, R. D., & Znajek, R. L. 1977, MNRAS, 179, 433

Bloom, J. S., et al. 2011, Science, 333, 203

Bondi, H. 1952, MNRAS, 112, 195

Bonnerot, C., Lu, W., & Hopkins, P. F. 2021, MNRAS, 504, 4885

Bonnerot, C., Rossi, E. M., Lodato, G., & Price, D. J. 2016, MNRAS, 455, 2253

Bonnerot, C., & Stone, N. C. 2021, Space Sci. Rev., 217, 16

Bowen, I. S. 1934, PASP, 46, 146

Brandenburg, A., & Subramanian, K. 2005, Phys. Rep., 417, 1

Brown, G. C., Levan, A. J., Stanway, E. R., Tanvir, N. R., Cenko, S. B., Berger, E., Chornock, R., & Cucchiaria, A. 2015, MNRAS, 452, 4297

Bu, D.-F., Yuan, F., Gan, Z.-M., & Yang, X.-H. 2016, ApJ, 818, 83

Burrows, D. N., et al. 2011, Nature, 476, 421

Cackett, E. M., Bentz, M. C., & Kara, E. 2021, iScience, 24, 102557

Cackett, E. M., Zoghbi, A., Reynolds, C., Fabian, A. C., Kara, E., Uttley, P., & Wilkins, D. R. 2014, MNRAS, 438, 2980

Castor, J. I., Abbott, D. C., & Klein, R. I. 1975, ApJ, 195, 157

Cenko, S. B., et al. 2016, ApJ, 818, L32

Cenko, S. B., et al. 2012, ApJ, 753, 77

Charalampopoulos, P., et al. 2022, A&A, 659, A34

Coughlin, E. R., & Begelman, M. C. 2014, ApJ, 781, 82

Cunningham, C. T. 1975, ApJ, 202, 788

Curd, B., & Narayan, R. 2019, MNRAS, 483, 565

Dabrowski, Y., Fabian, A. C., Iwasawa, K., Lasenby, A. N., & Reynolds, C. S. 1997, arXiv e-prints, astro

Dai, J. L., Lodato, G., & Cheng, R. 2021, Space Sci. Rev., 217, 12

Dai, L. 2012, Stanford PhD Thesis, url= https://searchworks.stanford.edu/view/9699358

Dai, L., McKinney, J. C., & Miller, M. C. 2015, ApJ, 812, L39

Dai, L., McKinney, J. C., Roth, N., Ramirez-Ruiz, E., & Miller, M. C. 2018, ApJ, 859, L20

Dauser, T., Garcia, J., Wilms, J., Böck, M., Brenneman, L. W., Falanga, M., Fukumura, K., & Reynolds, C. S. 2013, MNRAS, 430, 1694

De Colle, F., Guillochon, J., Naiman, J., & Ramirez-Ruiz, E. 2012, ApJ, 760, 103

Done, C., Tomaru, R., & Takahashi, T. 2018, MNRAS, 473, 838

Eddington, A. S. 1926, The Internal Constitution of the Stars

Evans, C. R., & Kochanek, C. S. 1989, ApJ, 346, L13

Event Horizon Telescope Collaboration, et al. 2022, ApJ, 930, L12

Event Horizon Telescope Collaboration, et al. 2019, ApJ, 875, L1

Fabian, A. C., Rees, M. J., Stella, L., & White, N. E. 1989, MNRAS, 238, 729

Foreman-Mackey, D. 2016, The Journal of Open Source Software, 24

Foreman-Mackey, D., Hogg, D. W., Lang, D., & Goodman, J. 2013, PASP, 125, 306

Frank, J., King, A., & Raine, D. J. 2002, Accretion Power in Astrophysics: Third Edition

Frank, J., & Rees, M. J. 1976, MNRAS, 176, 633

Frederick, S., Kara, E., Reynolds, C., Pinto, C., & Fabian, A. 2018, ApJ, 867, 67

French, K. D., Wevers, T., Law-Smith, J., Graur, O., & Zabludoff, A. I. 2020, Space Sci. Rev., 216, 32

Fuerst, S. V., & Wu, K. 2004, A&A, 424, 733

Galeev, A. A., Rosner, R., & Vaiana, G. S. 1979, ApJ, 229, 318

García, J., et al. 2014, ApJ, 782, 76

García, J., Dauser, T., Reynolds, C. S., Kallman, T. R., McClintock, J. E., Wilms, J., & Eikmann, W. 2013, ApJ, 768, 146

García, J., & Kallman, T. R. 2010, ApJ, 718, 695

George, I. M., & Fabian, A. C. 1991, MNRAS, 249, 352

Gezari, S. 2021, ARA&A, 59, 21

Gezari, S., Cenko, S. B., & Arcavi, I. 2017, ApJ, 851, L47

Gierliński, M., & Done, C. 2004, MNRAS, 349, L7

Golightly, E. C. A., Nixon, C. J., & Coughlin, E. R. 2019, ApJ, 882, L26

Gonzalez, A. G., Wilkins, D. R., & Gallo, L. C. 2017, MNRAS, 472, 1932

Graham, M. J., et al. 2019, PASP, 131, 078001

Greiner, J., Schwarz, R., Zharikov, S., & Orio, M. 2000, A&A, 362, L25

Guillochon, J., Manukian, H., & Ramirez-Ruiz, E. 2014, ApJ, 783, 23

Guillochon, J., & Ramirez-Ruiz, E. 2013, ApJ, 767, 25

Guillochon, J., & Ramirez-Ruiz, E. 2015, ApJ, 809, 166

Hammerstein, E., et al. 2023, ApJ, 942, 9

Hayasaki, K., & Jonker, P. G. 2021, ApJ, 921, 20

Hayasaki, K., Stone, N., & Loeb, A. 2016, MNRAS, 461, 3760

Heinz, S., Brüggen, M., Young, A., & Levesque, E. 2006, MNRAS, 373, L65

Hills, J. G. 1975, Nature, 254, 295

Hinkle, J. T., et al. 2021, MNRAS, 500, 1673

Holoien, T. W. S., Brown, J. S., Auchettl, K., Kochanek, C. S., Prieto, J. L., Shappee, B. J., & Van Saders, J. 2018, MNRAS, 480, 5689

Holoien, T. W. S., et al. 2016a, MNRAS, 463, 3813

Holoien, T. W.-S., et al. 2016b, MNRAS, 455, 2918

Holoien, T. W. S., et al. 2014, MNRAS, 445, 3263

Hung, T., et al. 2019, ApJ, 879, 119

Hung, T., et al. 2021, ApJ, 917, 9

Hung, T., et al. 2017, ApJ, 842, 29

Ingram, A., Mastroserio, G., Dauser, T., Hovenkamp, P., van der Klis, M., & García, J. A. 2019, MNRAS, 488, 324

Jiang, Y.-F., Stone, J. M., & Davis, S. W. 2014, ApJ, 796, 106

Jiang, Y.-F., Stone, J. M., & Davis, S. W. 2019, ApJ, 880, 67

Kajava, J. J. E., Giustini, M., Saxton, R. D., & Miniutti, G. 2020, A&A, 639, A100

Kara, E., Alston, W. N., Fabian, A. C., Cackett, E. M., Uttley, P., Reynolds, C. S., & Zoghbi, A. 2016a, MNRAS, 462, 511

Kara, E., Cackett, E. M., Fabian, A. C., Reynolds, C., & Uttley, P. 2014, MNRAS, 439, L26

Kara, E., Dai, L., Reynolds, C. S., & Kallman, T. 2018, MNRAS, 474, 3593

Kara, E., Fabian, A. C., Cackett, E. M., Steiner, J. F., Uttley, P., Wilkins, D. R., & Zoghbi, A. 2013, MNRAS, 428, 2795

Kara, E., Miller, J. M., Reynolds, C., & Dai, L. 2016b, Nature, 535, 388

Kara, E., et al. 2019, Nature, 565, 198

Kasen, D., Fernández, R., & Metzger, B. D. 2015, MNRAS, 450, 1777

Kasen, D., Thomas, R. C., & Nugent, P. 2006, ApJ, 651, 366

King, A. 2003, ApJ, 596, L27

Knigge, C., Scaringi, S., Goad, M. R., & Cottis, C. E. 2008, MNRAS, 386, 1426

Kobayashi, H., Ohsuga, K., Takahashi, H. R., Kawashima, T., Asahina, Y., Takeuchi, S., & Mineshige, S. 2018, Publications of the Astronomical Society of Japan, 70, 22

Komossa, S. 2015, Journal of High Energy Astrophysics, 7, 148

Komossa, S., & Bade, N. 1999, A&A, 343, 775

Kormendy, J., & Ho, L. C. 2013, ARA&A, 51, 511

Kosec, P., Pinto, C., Walton, D. J., Fabian, A. C., Bachetti, M., Brightman, M., Fürst, F., & Grefenstette, B. W. 2018, MNRAS, 479, 3978

Krause, M. O. 1979, Journal of Physical and Chemical Reference Data, 8, 307

Krawczynski, H., & Beheshtipour, B. 2017, ApJ, 849, 66

Law-Smith, J., Guillochon, J., & Ramirez-Ruiz, E. 2019, ApJ, 882, L25

Law-Smith, J. A. P., Coulter, D. A., Guillochon, J., Mockler, B., & Ramirez-Ruiz, E. 2020, ApJ, 905, 141

Leloudas, G., et al. 2022, arXiv e-prints, arXiv:2207.06855

Leloudas, G., et al. 2019, ApJ, 887, 218

Levan, A. J., et al. 2011, Science, 333, 199

Liu, X.-L., Dou, L.-M., Chen, J.-H., & Shen, R.-F. 2022, ApJ, 925, 67

Lodato, G., Franchini, A., Bonnerot, C., & Rossi, E. M. 2015, Journal of High Energy Astrophysics, 7, 158

Lodato, G., King, A. R., & Pringle, J. E. 2009, MNRAS, 392, 332

Lodato, G., & Rossi, E. M. 2011, MNRAS, 410, 359

Loeb, A., & Ulmer, A. 1997, ApJ, 489, 573

Lu, W., & Bonnerot, C. 2020, MNRAS, 492, 686

Lu, W., Krolik, J., Crumley, P., & Kumar, P. 2017, MNRAS, 471, 1141

Lu, W., & Kumar, P. 2018, ApJ, 865, 128

Lucy, L. B. 2002, A&A, 384, 725

Magorrian, J., & Tremaine, S. 1999, MNRAS, 309, 447

Magorrian, J., et al. 1998, AJ, 115, 2285

Masterson, M., et al. 2022, ApJ, 934, 35

Matsumoto, T., & Piran, T. 2021, MNRAS, 502, 3385

Matt, G., Fabian, A. C., & Ross, R. R. 1993, MNRAS, 262, 179

Matt, G., Perola, G. C., & Piro, L. 1991, A&A, 247, 25

McConnell, N. J., Ma, C.-P., Gebhardt, K., Wright, S. A., Murphy, J. D., Lauer, T. R., Graham, J. R., & Richstone, D. O. 2011, Nature, 480, 215

McKinney, J. C., Dai, L., & Avara, M. J. 2015, MNRAS, 454, L6

McKinney, J. C., Tchekhovskoy, A., & Blandford, R. D. 2012, MNRAS, 423, 3083

McKinney, J. C., Tchekhovskoy, A., Sadowski, A., & Narayan, R. 2014, MNRAS, 441, 3177

Metzger, B. D., & Stone, N. C. 2016, MNRAS, 461, 948

Miller, J. M., et al. 2015, Nature, 526, 542

Misner, C. W., Thorne, K. S., & Wheeler, J. A. 1973, Gravitation

Miyamoto, S., Kitamoto, S., Mitsuda, K., & Dotani, T. 1988, Nature, 336, 450

Mockler, B., Guillochon, J., & Ramirez-Ruiz, E. 2019a, ApJ, 872, 151

Mockler, B., Guillochon, J., & Ramirez-Ruiz, E. 2019b, ApJ, 872, 151

Mockler, B., & Ramirez-Ruiz, E. 2021, ApJ, 906, 101

Mortlock, D. J., et al. 2011, Nature, 474, 616

Mummery, A., & Balbus, S. A. 2020, MNRAS, 492, 5655

Mundo, S. A., et al. 2020, MNRAS, 496, 2922

Murray, N., Chiang, J., Grossman, S. A., & Voit, G. M. 1995, ApJ, 451, 498

Mushotzky, R. F., Serlemitsos, P. J., Becker, R. H., Boldt, E. A., & Holt, S. S. 1978, ApJ, 220, 790

Müller, A. 2004, University of Heidelberg PhD thesis, doi = 10.11588/heidok.00005217

Narayan, R., Igumenshchev, I. V., & Abramowicz, M. A. 2003, PASJ, 55, L69

Narayan, R., McClintock, J. E., & Yi, I. 1996, ApJ, 457, 821

Narayan, R., & Yi, I. 1994, ApJ, 428, L13

Narayan, R., & Yi, I. 1995, ApJ, 452, 710

Noebauer, U. M., & Sim, S. A. 2019, Living Reviews in Computational Astrophysics, 5, 1

Novikov, I. D., & Thorne, K. S. 1973, in Black Holes (Les Astres Occlus), 343

Nowak, M. A., Vaughan, B. A., Wilms, J., Dove, J. B., & Begelman, M. C. 1999, ApJ, 510, 874

Ohsuga, K., Mineshige, S., Mori, M., & Kato, Y. 2009, Publications of the Astronomical Society of Japan, 61, L7

Parkinson, E. J., Knigge, C., Long, K. S., Matthews, J. H., Higginbottom, N., Sim, S. A., & Hewitt, H. A. 2020, MNRAS, 494, 4914

Parkinson, E. J., Knigge, C., Matthews, J. H., Long, K. S., Higginbottom, N., Sim, S. A., & Mangham, S. W. 2022, MNRAS, 510, 5426

Paxton, B., Bildsten, L., Dotter, A., Herwig, F., Lesaffre, P., & Timmes, F. 2011, ApJS, 192, 3

Pfister, H., Volonteri, M., Dai, J. L., & Colpi, M. 2020, MNRAS, 497, 2276

Phinney, E. S. 1989, in IAU Symposium, Vol. 136, The Center of the Galaxy, ed. M. Morris, 543

Pinto, C., et al. 2017, MNRAS, 468, 2865

Pinto, C., Middleton, M. J., & Fabian, A. C. 2016, Nature, 533, 64

Piran, T., Svirski, G., Krolik, J., Cheng, R. M., & Shiokawa, H. 2015, ApJ, 806, 164

Pomraning, G. C. 1969, J. Quant. Spec. Radiat. Transf., 9, 407

Ponti, G., Papadakis, I., Bianchi, S., Guainazzi, M., Matt, G., Uttley, P., & Bonilla, N. F. 2012, A&A, 542, A83

Pozdnyakov, L. A., Sobol, I. M., & Syunyaev, R. A. 1977, Soviet Ast., 21, 708

Prieto, J. L., et al. 2016, ApJ, 830, L32

Proga, D., Stone, J. M., & Kallman, T. R. 2000, ApJ, 543, 686

Ramirez-Ruiz, E., & Rosswog, S. 2009, ApJ, 697, L77

Rees, M. J. 1988, Nature, 333, 523

Reis, R. C., & Miller, J. M. 2013, ApJ, 769, L7

Reynolds, C. S. 2014, Space Sci. Rev., 183, 277

Reynolds, C. S., & Begelman, M. C. 1997, ApJ, 488, 109

Reynolds, C. S., Young, A. J., Begelman, M. C., & Fabian, A. C. 1999, ApJ, 514, 164

Ross, R. R., & Fabian, A. C. 2005, MNRAS, 358, 211

Ross, R. R., Fabian, A. C., & Young, A. J. 1999, MNRAS, 306, 461

Rossi, E. M., Stone, N. C., Law-Smith, J. A. P., Macleod, M., Lodato, G., Dai, J. L., & Mandel, I. 2021, Space Sci. Rev., 217, 40

Roth, N., & Kasen, D. 2015, ApJS, 217, 9

Roth, N., & Kasen, D. 2018, ApJ, 855, 54

Roth, N., Kasen, D., Guillochon, J., & Ramirez-Ruiz, E. 2016, ApJ, 827, 3

Roth, N., Rossi, E. M., Krolik, J., Piran, T., Mockler, B., & Kasen, D. 2020, Space Sci. Rev., 216, 114

Rybicki, G. B., & Lightman, A. P. 1979, Radiative processes in astrophysics

Saxton, R., Komossa, S., Auchettl, K., & Jonker, P. G. 2021, Space Sci. Rev., 217, 18

Sazonov, S., et al. 2021, MNRAS, 508, 3820

Schnittman, J. D., Krolik, J. H., & Noble, S. C. 2013, ApJ, 769, 156

Shakura, N. I., & Sunyaev, R. A. 1973, A&A, 500, 33

Shapiro, I. I. 1964, Phys. Rev. Lett., 13, 789

Shiokawa, H., Krolik, J. H., Cheng, R. M., Piran, T., & Noble, S. C. 2015, ApJ, 804, 85

Silk, J., & Rees, M. J. 1998, A&A, 331, L1

Sądowski, A. 2009, ApJS, 183, 171

Sądowski, A., & Narayan, R. 2016, MNRAS, 456, 3929

Sądowski, A., Narayan, R., McKinney, J. C., & Tchekhovskoy, A. 2014, MNRAS, 439, 503

Sądowski, A., Tejeda, E., Gafton, E., Rosswog, S., & Abarca, D. 2016, MNRAS, 458, 4250

Steinberg, E., & Stone, N. C. 2022, arXiv e-prints, arXiv:2206.10641

Stone, N., & Loeb, A. 2012, Phys. Rev. Lett., 108, 061302

Stone, N. C., Kesden, M., Cheng, R. M., & van Velzen, S. 2019, General Relativity and Gravitation, 51, 30

Stone, N. C., & Metzger, B. D. 2016, MNRAS, 455, 859

Stone, N. C., Vasiliev, E., Kesden, M., Rossi, E. M., Perets, H. B., & Amaro-Seoane, P. 2020, Space Sci. Rev., 216, 35

Strubbe, L. E., & Quataert, E. 2009, MNRAS, 400, 2070

Svirski, G., Piran, T., & Krolik, J. 2017, MNRAS, 467, 1426

Tanaka, Y., et al. 1995, Nature, 375, 659

Taylor, C., & Reynolds, C. S. 2018a, ApJ, 855, 120

Taylor, C., & Reynolds, C. S. 2018b, ApJ, 868, 109

Tchekhovskoy, A., Metzger, B. D., Giannios, D., & Kelley, L. Z. 2014, MNRAS, 437, 2744

Tchekhovskoy, A., Narayan, R., & McKinney, J. C. 2011, MNRAS, 418, L79

Tejeda, E., Gafton, E., Rosswog, S., & Miller, J. C. 2017, MNRAS, 469, 4483

Thomsen, L. L., Dai, L., Kara, E., & Reynolds, C. 2022a, ApJ, 925, 151

Thomsen, L. L., Kwan, T. M., Dai, L., Wu, S. C., Roth, N., & Ramirez-Ruiz, E. 2022b, ApJ, 937, L28

Thomsen, L. L., Lixin Dai, J., Ramirez-Ruiz, E., Kara, E., & Reynolds, C. 2019, ApJ, 884, L21

Thorne, K. S. 1974, ApJ, 191, 507

Ulmer, A. 1999, ApJ, 514, 180

Uttley, P., Cackett, E. M., Fabian, A. C., Kara, E., & Wilkins, D. R. 2014, A&A Rev., 22, 72

van Velzen, S., et al. 2021, ApJ, 908, 4

van Velzen, S., Holoien, T. W. S., Onori, F., Hung, T., & Arcavi, I. 2020, Space Sci. Rev., 216, 124

van Velzen, S., Stone, N. C., Metzger, B. D., Gezari, S., Brown, T. M., & Fruchter, A. S. 2019, ApJ, 878, 82

Vestergaard, M., & Peterson, B. M. 2006, ApJ, 641, 689

Vincentelli, F. M., Mastroserio, G., McHardy, I., Ingram, A., & Pahari, M. 2020, MNRAS, 492, 1135

Walton, D. J., et al. 2016, ApJ, 826, L26

Wang, J., & Merritt, D. 2004, ApJ, 600, 149

Wevers, T., et al. 2019, MNRAS, 488, 4816

Weymann, R. J., Carswell, R. F., & Smith, M. G. 1981, ARA&A, 19, 41

Weymann, R. J., Morris, S. L., Foltz, C. B., & Hewett, P. C. 1991, ApJ, 373, 23

Wilkins, D. R. 2013, University of Cambridge, url= https://www.repository.cam.ac.uk/handle/1810/244941

Wilkins, D. R., Cackett, E. M., Fabian, A. C., & Reynolds, C. S. 2016, MNRAS, 458, 200

Wilkins, D. R., & Fabian, A. C. 2012, MNRAS, 424, 1284

Wilkins, D. R., Reynolds, C. S., & Fabian, A. C. 2020, MNRAS, 493, 5532

Wong, T. H. T., Pfister, H., & Dai, L. 2022, ApJ, 927, L19

Wu, S., Coughlin, E. R., & Nixon, C. 2018, MNRAS, 478, 3016

Wu, S.-M., & Wang, T.-G. 2007, MNRAS, 378, 841

Wu, X.-B., et al. 2015, Nature, 518, 512

Yang, H., Yuan, F., Kwan, T., & Dai, L. 2022, arXiv e-prints, arXiv:2211.10710

Yao, Y., et al. 2022, arXiv e-prints, arXiv:2206.12713

Yuan, F., Gan, Z., Narayan, R., Sadowski, A., Bu, D., & Bai, X.-N. 2015, ApJ, 804, 101

Yuan, F., & Narayan, R. 2014, ARA&A, 52, 529

Yuan, Y., Blandford, R. D., & Wilkins, D. R. 2019, MNRAS, 484, 4920

Zauderer, B. A., et al. 2011, Nature, 476, 425

Zoghbi, A., Fabian, A. C., Reynolds, C. S., & Cackett, E. M. 2012, MNRAS, 422, 129

Zoghbi, A., Reynolds, C., Cackett, E. M., Miniutti, G., Kara, E., & Fabian, A. C. 2013, ApJ, 767, 121